The Abyssal Ocean's Contributions to the Global Energy and Sea Level Budgets Between the 1990s and 2000s

Sarah Michelle Goldstein Purkey

A dissertation
submitted in partial fulfillment of the
requirements for degree of

Doctor of Philosophy

University of Washington
2014

Reading Committee:
Gregory C. Johnson, Chair
Susan L. Hautala
Mark J. Warner

Program Authorized to Offer Degree:
School of Oceanography

University of Washington

Abstract

The Abyssal Ocean's Contributions to the Global Energy and Sea Level Budgets Between the 1990s and 2000s

Sarah Michelle Goldstein Purkey

Chair of Supervisory Committee:
Dr. Gregory C. Johnson
Affiliate Professor, Oceanography

Over the past three decades, Antarctic Bottom Water (AABW), a cold, dense water-mass produced around Antarctica that feeds the bottom limb of the Meridional Overturning Circulation (MOC), has warmed, freshened, and declined in volume. Using highly accurate, full-depth, ship-based, conductivity-temperature-depth measurements taken along repeated oceanographic sections between 1981 and 2013, combined with satellite altimetry and gravity data, we quantify water-property changes in the deep Southern Ocean and the abyssal global ocean and evaluate the relative contribution of these abyssal changes to the global energy and sea level rise budgets.

We find a strong warming trend throughout the deep (greater than 1000 m) Southern Ocean and abyssal (greater than 4000 m) global oceans. The abyssal warming follows AABW circulation pathways into the central Pacific, western Atlantic, and eastern Indian oceans, weakening in magnitude to the north. The warming is equivalent to a heat flux of 0.095 (± 0.062) W m^{-2} applied over the entire surface area of the Earth, a statistically significant fraction of the present global energy budget. The observed warming pattern is also consistent with a global-scale contraction of AABW, suggesting a slowdown of the bottom limb of the MOC. The contraction can be seen in a downward displacement of potential isotherms over time that is associated with warming on isobars. Within the Southern Ocean, potential isotherms near the top of AABW (0 °C potential temperature) have fallen by approximately 100 m per decade, equivalent to an 8.2 (± 2.6) Sv (1 Sv = 1×10^6 m^3 s^{-1}) contraction rate. The deep water-mass contraction is compensated near the surface by an expansion of Circumpolar Deep Water, presumably entering from the north.

In addition, the newest formed AABW varieties within the Indian and Pacific sectors of the Southern Ocean have freshened. Freshening of 0.02 PSS-78 per decade is observed in the AABW directly downstream from formation sites along the Antarctic continent, with freshening rates roughly a tenth of this in the deep interior of basins adjacent to Antarctica. The fresh water flux required to account for the observed freshening of AABW in these two basins is 73 (±26) GT yr^{-1}. Furthermore, the warming and freshening below the 0 °C potential isotherm south of 30 °S contribute 0.52 (±0.18) mm per year to local steric sea level rise (SLR), almost entirely owing to the thermal expansion from warming. The warming from isotherm heave integrated below 2000 m in the Southern Ocean (south of 30ºS) accounts for a net heat uptake of 34 (±14) TW.

Finally, the full-depth steric contributions to SLR calculated along the repeated hydrographic sections are used to assess regional and global rates of SLR owing to mass addition through a full depth SLR budget. First, we use the residual between changes in full depth steric sea level and changes in total sea level from satellite altimetry to quantify the ocean mass contribution to sea level rise between 1996 and 2006. Second, regional trends in mass addition are estimated directly using data from the Gravity Recovery And Climate Experiment (GRACE) from 2003–2013. These two independent methods both find a global mean rate of mass addition of 1.5 (± 0.4) mm yr^{-1} over their respective periods with large regional variability. Both methods find higher rates of mass addition in the North Pacific, South Atlantic, and Indo-Atlantic sector of the Southern Ocean and smaller mass addition rates in the North Atlantic and Pacific Sector of the Southern Ocean, possibly associated with recent changes in the gravity field from ice loss in these two regions.

Table of Contents

Purkey, S. G., G. C. Johnson and D. P. Chambers. 2014. Relative contributions of ocean mass and deep steric changes to sea level rise between 1993 and 2013. J. Geophys. Res., submitted.

List of figures

List of tables

Acknowledgments

First and foremost, I would like to express my utmost gratitude to my advisor Gregory C. Johnson. This dissertation would not have been possible without his ideas, guidance, and oversight. He taught me how to be an Oceanographer: from collecting high quality data, to conducting scientific research, through preparing a well-written manuscript. I am eternally grateful for his endless encouragement, enthusiasm, and for being a wonderful role model.

I would also like to thank my supervising committee, Susan Hautala, Mark Warner, and Cecilia Bitz, for their contribution of ideas and useful discussions over the past 6 years. In addition, I owe huge thanks to LuAnne Thompson for serving as my “on campus advisor”, for being my fellowship sponsor, a fantastic teacher, and a great PCC advisor.

I would like to thank my classmates for their help, discussions, and contributions over the years, in addition to making this whole process much more enjoyable. I am especially grateful to my PMEL officemates, Andrea Fassbender and Pamela Barrett, for always being my chemical-oceanography support team and listening to endless practice talks. My fellow PCC and PO graduate students helped me to stretch my field of expertise both in the classroom and during many adventures exploring the Pacific Northwest.

I owe an immense debt of gratitude to all the crew and scientist team members who helped collect and process the WOCE and GO-SHIP data, without which this work would not be possible. In particular, I owe many thanks to Kristene McTaggart, who patiently introduced me to the world of CTD instrumentation, data processing, and calibration back in 2008. She, together with Greg, continued to be my lifeline via satellite phones and email whenever issues arose out in the field over the past 7 years.

This research would not have been possible without generous support from NOAA, the University of Washington Graduate School, and NASA headquarters under the NASA Earth and Space Fellowship Program- Grant NNX11AL89H.

Last but not least I would like to thank my family; my parents for their years of support, my siblings for always keeping me grounded, and my husband for being my favorite colleague, friend, and partner.

This thesis includes previously published and submitted work. Sarah G. Purkey performed the analysis and writing, with guidance and editing from Gregory C. Johnson. Reprinted with permission from publishers. Chapters 2-5 should be cited as follows:

Chapter 2:

Purkey, S. G., and G. C. Johnson, 2010: Warming of Global Abyssal and Deep Southern Ocean Waters Between the 1990s and 2000s: Contributions to Global Heat and Sea Level Rise Budgets. Journal of Climate, 23, 6336-6351, doi:10.1175/2010JCLI3682.1.

Chapter 3:

Purkey, S. G. and G. C. Johnson, 2012: Global contraction of Antarctic Bottom Water between the 1980s and 2000s. Journal of Climate, 25, 5830-5844, doi:10.1175/JCLI-D-11-00612.1.

Chapter 4:

Purkey, S. G. and G. C. Johnson, 2013: Antarctic Bottom Water warming and freshening: Contributions to sea level rise, ocean freshwater budgets, and global heat gain. Journal of Climate, 26, 6105-6122, doi:10.1175/JCLI-D-12-00834.1

Chapter 5:

Purkey, S. G., G. C. Johnson and D. Chambers, 2014: Relative contributions of ocean mass and deep steric changes to sea level rise between 1993 and 2013. J. of Geophysical Research, submitted.

Chapter 1

Introduction

The deep ocean is filled with cold dense waters originating from high latitudes, replenished through the buoyancy-driven Meridional Overturning Circulation (MOC; Johnson 2008). Two distinct varieties of deep water exist; North Atlantic Deep Water (NADW), produced through open water convection in the north Atlantic, and Antarctic Bottom Water (AABW), formed through complex ocean-ice-atmosphere interactions along the Antarctic Continental Shelf (e.g. Lumpkin and Speer 2007). The bottom cell of the MOC consists of cold, relatively fresh northward-flowing AABW. The overlying southward-flowing, saltier, and warmer NADW eventually upwells and mixs in the Antarctic Circumpolar Current (ACC) to create Circumpolar Deep Water (CDW; Sloyan and Rintoul 2001; Schmitz 1995). Together, the deep water formation and circulation of AABW and NADW fill the worlds deep oceans and play critical roles in the global ocean circulation, heat transport, and CO_2 transport (Lumpkin and Speer 2007; Johnson 2008; Levitus 2005).

Historically, the southern limb of the MOC has been thought to be fairly stable on century time scales, partially owing to limited data in the Southern Ocean. However, during the late 1980s early 1990s, World Ocean Circulation Experiment (WOCE) investigators teamed up to collected the most well sampled, high-quality, full-depth global ocean data set to date. Subsequent sampling of the abyssal ocean at different locations around the globe has revealed that AABW properties have warmed and freshened within formation regions and along AABW pathways to the north (e.g. Aoki et al. 2005;Johnson and Doney 2006; Johnson et al. 2008a).

Here an analysis is presented quantifying global and regional decadal trends in water properties and circulation of AABW and AABW-derived waters within the Southern Ocean and around the globe. In addition, the following work estimates the contributions of these abyssal changes to Earth's energy imbalance, sea level rise (SLR), and the ocean's freshwater budget. This introduction provides necessary background on AABW formation (1.1), global circulation (1.2), and previous studies on recent changes in AABW properties (1.3). Section 1.4 provides an outline of how Chapters 2–5 contribute to our understanding of decadal variability in AABW properties and circulation.

1.1 AABW formation

AABW has various definitions. In the Southern Ocean a classic early definition is water of potential temperature (θ) < 0 ºC (e.g. Killworth 1983). However, in the Atlantic Ocean, bottom water colder than θ of 2 °C with some water-property evidence of Antarctic origins is sometimes referred to as AABW (e.g. Deacon 1933). The definition can be refined and subdivided into a 'pure' AABW, defined as water with density too great to travel through Drake Passage and mostly confined to the Southern Ocean, and a lighter Lower CDW (LCDW), consisting of a mix of AABW and CDW that escapes the ACC to fill most of the deep Indian, Pacific, and southwest Atlantic oceans (Orsi et al. 1999; Orsi 2002; Johnson 2008). A recent definition of pure AABW is that of Southern Hemisphere waters having neutral density > 28.27 kg m^{-3} (Orsi et al., 1999), which very loosely corresponds to θ < 0 °C definition. While this "pure" AABW is only found south of the ACC with the exception of the Argentine Basin, AABW-derived waters are found in many deep basins around the globe (Johnson 2008). LCDW travels north into all three oceans along four primary western boundaries (Schmitz 1995). This water is still mostly (over 60%)

AABW and the deep water property changes seen along these pathways trace back to its AABW sources (Fig. 1.1; Johnson 2008).

AABW is produced in at least three locations along the Antarctic continental shelf through complex interactions among the ocean, atmosphere, sea ice, and ice shelf (Fig. 1.2). At each formation site, a pool of cold, dense shelf water exists within a shallow continental shelf. This dense shelf water is formed through three primary mechanisms that allow the water to become more saline. First, coastal polynyas in the sea ice, opened either by katabatic winds or sensible heat from below, allow for sea-ice production and export above the shelf (Foster and Carmack 1976; Rintoul 1998). Through sea-ice formation and heat loss to the atmosphere, the surface waters are cooled and become more saline from brine rejection. Second, as the dense water sinks, it interacts with the ice shelf and melts it at depth. This melting creates freshening near the ice shelf grounding line, decreasing the density of the shelf waters, and allowing them to rise as supercooled waters which refreeze, causing further brine rejection (Jacobs 2004). Third, the encroachment of tongues of modified CDW, or Warm Deep Water as it is referred to in the Weddell Sea, provides further salt as they mix with shelf waters (Foster and Carmack 1976). Observations at each formation site show that slightly different combinations of these mechanisms form shelf waters with different θ–S properties (e.g. Jacobs 1970; Foster and Carmack 1976; Rintoul 1998). However, at all formation sites, conditions allow for shelf water that is sufficiently dense to cascade down the continental slope in plumes, mixing with ambient waters, to form AABW.

The most prolific variety of AABW is Weddell Sea Bottom Water (WSBW), formed along the western side of the Weddell shelf in the South Atlantic sector of the Southern Ocean. WSBW is defined as having $\theta < -0.6$ °C and salinity (S) less than 34.64 with production rates between 3–5 Sv (1 Sv = 1 × 10^6 m^3 s^{-1}; Orsi et al. 1999). Here, the shelf water is primarily formed from a winter coastal polynya that leaves a salty, cold, oxygen-rich water that fills the shelf (Foster and Carmack 1976). The descending shelf water turns left as if flows down the slope and travels clockwise around the Weddell Gyre and into the interior, entraining modified CDW along the way. Within the Weddell Gyre, Weddell Sea Deep Water (WSDW; $\theta<0$ °C) sits above WSBW, formed either directly from the overflow from a lighter variety of shelf water found on the eastern side of the shelf or from further mixing between WSBW and overlying Warm Deep Water (Fahrbach et al. 1995).

Similarly, the large Ross Sea shelf holds dense water that cascades down the slope to produce another variety of slightly warmer, saltier, AABW called Ross Sea Bottom Water (RSBW). Using data collected during the mid-1980s and early-1990s, RSBW was defined as having θ ranging from -0.6 to -0.3 ºC and salinity > 34.72 (Orsi et al. 1999), although more recent observations suggest RSBW has freshened and now falls outside this range (e.g. Swift and Orsi, 2012). The Ross Shelf high salinity water appears more dependent on freezing/unfreezing processes under the ice shelf than WSBW (Jacobs, 1970). Again, as the dense water flows down the shelf, it mixes with ambient waters to form RSBW. RSBW follows the bathymetry toward the northern corner of the Ross Sea were some continues to the west along the Antarctic continent and some continues with the gyre flow to the east and interior of the Ross Sea (Jacobs et al. 1970; Jacobs 2004).

Finally, Adelie Land Bottom Water (ALBW) is formed along the Wilkes-Adelie Land coast primarily between 145–142.5 ºE in the Adelie Depression where the highest salinity shelf water is found (Rintoul 1998). Again, the shelf water is derived through slightly different processes than in the Weddell and Ross Seas. Here, high salinity shelf water is found along a much narrower shelf with less ice export and the heat from the modified CDW may play a bigger role in keeping the coastal polynya open as well as bringing high salinity waters to the shelf (Rintoul 1998). ALBW is colder and fresher than RSBW, falling in between WSBW and RSBW with θ ranging between -0.8 and -0.4 °C and salinities ranging from 34.62 to 34.68 (Orsi et al 1999). ALBW flows westward down the continental slope, in the direction of the overlying coastal current, mixing with RSBW and filling the interior of the Australian-Antarctic Basin.

Elsewhere around the Antarctic continent, coastal polynyas with high ice export rates falling near shallow shelves are likely producing some amount of AABW, but not at the rate of ALBW, RSBW, or WSBW. For example, recently, newly formed AABW has been detected near Cape Darnley and Vincennes Bay but total transport estimates are low (Ohshima et al. 2013; Kitade et al. 2014).

Finally, open-water convection is not believed to be a major mechanism of AABW formation since the 1970s. However, it may have contributed more under previous climate regimes. During the austral 1974–1976 winters, a large open-water polynya was observed in the Weddell Sea producing an estimated 1.6–3.6 Sv of deep water (Gordon 1982). This was the last observed site of significant open-ocean deep convection in the Southern Ocean. While smaller polynyas have been observed by satellite altimetry since, none are thought to have allowed deep open-ocean convection at rates observed in the 1970s (e.g. Comiso et al. 1987).

1.2 Global circulation of AABW

Wust (1935) accurately portrayed the deep Atlantic MOC with two overturning cells; an AABW-fed bottom cell flowing north and a NADW-fed upper cell flowing south. Wust's early schematic depicted AABW traveling north across the equator and gaining buoyancy through mixing with the overlying NADW. Since the 1930s, a more quantitative understanding of abyssal flow has developed, including descriptions of abyssal circulation in the Indian and Pacific oceans. Abyssal AABW circulation transports ~20 Sv of AABW/LCDW north out of the Southern Ocean along four primary deep western boundary currents (e.g. Schmitz 1995; Lumpkin and Speer 2007).

In the Atlantic, water as cold as -0.6 °C leaves the Weddell and Enderby basins through a deep western boundary current, warming as it travels through the Scotia Sea, Argentine Basin, Brazil Basin, and eventually across the equator (Fig 1.1;Fig. 3.1; Schmitz 1995; Gouretski and Koltermann 2004). WSDW circulating around the Weddell Gyre along the South Scotia Ridge can travel north through the Orkney Passage into the Scotia Sea or around the South Sandwich Trench into the Argentine Basin (Meredith et al. 2008). AABW continues north along the western boundary current through the Argentine Basin and circulates around the basin, filling it with cold WSDW (Fig 3.1). The AABW then flows north into the Brazil Basin through the topographically restrictive Vema and Hunter channels at a rate of 6.9 Sv ($\theta < 2$ °C) and near the equator into the east and north Atlantic (e.g. Hogg 1999). Trace amounts of AABW can still be detected even at 24 °N, where it flows north along the western flank of the Mid-Atlantic Ridge (e.g. Johnson et al. 2008b).

The Indian Ocean has two pathways carrying AABW to the north (Fig. 3.1). In the western Indian, AABW primarily of Weddell Sea origin travels north through the Madagascar Basin, Mascarene Basin, Somali Basin and Arabian Basin with geostrophic northward transport estimates ranging from 7–11 SV at 32 °S entering the Madagascar Basin and reducing to 1–5 SV by 9 °S in the Amirante Passage leading into the Somali Basin (e.g. Johnson et al. 1998). In the east Indian ocean, a mixture of RSBW and ALBW varieties of AABW circulate clockwise around the Australian-Antarctic Basin flowing along the Kerguelen Plateau before flowing north through the Australian-Antarctic Discordance (e.g. Sloyan 2006). Velocity measurements within the deep western boundary current along the Kerguelen Plateau imply northward transports of ~12 Sv of water for $\theta \leq 0$ °C but with high temporal variability (Fukamachi et al. 2010). AABW travels north into the South Australian Basin, then into the Wharton Basin through a gap between the Broken and Naturaliste plateaus, and has been detected crossing the Mid-Indian Ridge into the Mid-Indian Basin at multiple gaps (Warren and Johnson 2002; Sloyan 2006).

The abyssal Pacific is fed by LCDW containing AABW components from both the Australian-Antarctic Basin and South Pacific (Fig. 3.1). A relatively shallow sill constrains deep water flowing into the Southwest Pacific Basin (Whitworth et al. 1999). A deep western boundary current carries an estimated 15.8 (±9.2) Sv of bottom and deep waters north (Whitworth et al. 1999). The northward flow continues into the Pacific Basin through the Samoan Passage (e.g. Roemmich and Hautala 1996).

Inverse models estimate between 20–30 Sv of deep water is transported north out of the Southern Ocean as part of the bottom cell of the MOC (e.g. Ganachaud and Wunsch 2000; Sloyan and Rintoul 2001; Lumpkin and Speer 2007). Pure AABW production rates are around 8 Sv, but AABW mixes heavily with CDW to produce a lighter, warm water mass with two to three times the transport by the time it reaches the subtropics (Orsi et al. 1999; Sloyan and Rintoul 2001; Orsi 2002). Regardless, this water mass is still primarily composed of AABW, with water found below 4000 m in the Indian, Pacific, and southwest Atlantic oceans containing over 50% AABW (Johnson 2008). Using a 7-box inverse model, Ganachaud and Wunsch (2000) estimated northward transport of 21(±6) Sv of AABW (defined as neutral densities greater than 28.11 kg m^{-3}) across 25 °S. Sloyan and Rintoul (2001), using an inverse method focusing on only the Southern Ocean, found a total of 25 Sv of northward-flowing AABW, with 8 Sv in the Pacific, 10 Sv in the Indian, and 6 Sv in the Atlantic Ocean. Similarly, Lumpkin and Speer (2007) also used an inverse technique taking air-sea heat and freshwater fluxes and direct current measurements into account and also found 25 Sv of AABW transport to the north, with 5.6 (±3.0) Sv in the Atlantic, 11.0 (±5.1) Sv in the Pacific and 9.2 (±2.7) Sv in the Indian Ocean.

AABW continues north across the equator, filling most of the global deep ocean (Johnson 2008). Using a multivariate least-squares near-global water-mass analysis of AABW and NADW, Johnson (2008) found AABW occupies about twice the volume of NADW. Below 1000 m in the Southern Ocean, water is over 70% AABW and over 50% AABW below 2500 in the Indian and Pacific oceans. Even in the western South Atlantic, AABW has a strong presence below 4000 m (Johnson 2008).

1.3 AABW warming, freshening, and volume changes

A number of previous studies have revealed property and circulation changes both within and down-stream from AABW formation regions. In the Weddell Sea, the WSBW and WSDW have shown decadal variability in temperature, salinity, and volume. The WSBW warmed by 0.009 °C yr^{-1} between 1990 and 1998, followed by a weakening of the warming signal, and showed an overall decrease in volume of WSBW within the gyre (Fahrbach et al. 2004). Using historical data, Robertson et al. (2002), found a slight, but not statistically significant, warming trend WSDW extending back to 1970s with the coldest WSDW found during and directly after the close of the Weddell Polynya, suggesting that the end of deep convection triggered the decline and warming of WSDW.

In the South Indian and South Pacific, RSBW and ALBW both freshened between 1950s and 2000s. Ross Shelf Water, an important end member of RSBW, has freshened by 0.03 PSS-78 decade^{-1} between 1958 and 2008, possibly owing to increased glacial melt in the west Antarctic (Jacobs 2002; Jacobs and Giulivi 2010). Directly downstream from RSBW formation regions, the deep western boundary current carrying recently formed RSBW has freshened by 0.04 between 1992 and 2011 (Swift and Orsi 2012). In the South Indian Ocean at 140 °S directly off the coast from ALBW formation, newly formed ALBW has also freshened by 0.03 between 1994–2002 (Aoki et al. 2005). In addition, the interior of the Australian-Antarctic Basin, fed by both RSBW and ALBW, AABW has also freshened by 0.005 between 1994/5 and 2007 (e.g. Johnson et al. 2008a).

Furthermore, decadal warming has been observed in regions fed by AABW outside the Southern Ocean. AABW has warmed throughout the Pacific Ocean between the 1990s and 2000s, with rates highest close to the source, but detectible even in the northern parts of the North Pacific Basin (Fukasawa et al. 2004; Kawano et al. 2006; Johnson et al. 2007; Masuda et al. 2010). In the South Pacific Basin, the deep western boundary current has warmed at a rate between 0.005 and 0.01 °C per decade between 1990s and late 2000s (Kawano et al. 2006; Sloyan et al. 2013). Furthermore, consistent warming has been detected through the interior of the South and Central Pacific basins between 1985 and 1999 (Fukasawa et al. 2004; Johnson et al. 2007). Similarly, in the western Atlantic, AABW has warmed along the outflow from the Weddell to the Scotia Sea, Argentine Basin, and Brazil Basin (Johnson and Doney 2006). Reoccupation of the cross section along AABW north ward flow in the Scotia Sea showed high variability in water mass properties and volume between 1995, 1999, and 2005 (Meredith et al. 2008). AABW in the Brazil and Argentine basins lost density and warmed between the 1980s and 2005 by ~0.04 ºC decade^{-1} (Coles et al. 1996; Johnson and Doney 2006). Furthermore, the coldest waters flowing north through the deep Vema Channel between the Argentine Basin and Brazil Basin have been well sampled between the 1970s and 2010, with 19 occupations showing steady warming at a rate of 2.8 mK yr^{-1} of the coldest waters between 1995 and 2010 (Zenk and Morozov 2007; Zenk and Visbeck 2013), consistent with the more temporally sparse but spatially dense section differences found in the adjacent Argentine and Brazil basins.

These observations of consistent AABW warming along deep western boundary currents around the globe are consistent with a decrease in the strength of the bottom limb of the MOC (e.g. Kawano et al. 2006; Masuda et al. 2010). If AABW production slowed in recent decades, this change could be communicated throughout the globe through thermocline readjustments via Kelvin and Rossby waves on time-scales of less than 100 years (e.g. Masuda et al. 2010). This adiabatic re-adjustment would result in a decrease in volume, or a sinking of potential temperature (or density) surfaces, appearing as warming on isobars. Masuda et al. (2010) demonstrated this with a data-assimilation model connecting the North Pacific Basin warming to a decrease in AABW production in the Southern Indian. This hypothesis is further supported by detection of recent decreases in northward transport along the deep western boundary currents in the South Pacific, North Pacific, and North Atlantic. Along the western edge of the north Atlantic at 24°N, AABW transport has decreased between 1981 and 2004 (Johnson et al. 2008b) with a slight rebound in 2010 (Frajka-Williams et al. 2011) calculated from changes in geostrophic shear. Similarly, in the North Pacific at 24 °N a decrease in the northward transport has been detected between 1985 and 2005 (Kouketsu et al. 2009). Furthermore, using the heat content changes from a re-analysis product spanning from 1967 to 2006, Kouketsu et al. (2011)

found a statistically significant reduction in northward transport in the west Atlantic and Pacific at 35 °S of -0.36 (± 0.06) and -0.71 (± 0.23) x 10^{-9} kg s^{-1} $decade^{-1}$, respectively.

Further understanding of these deep changes is important for assessing past climate variability as well as accurately predicting the future. The strength of the deep MOC controls the ability of the ocean to sequester anthropogenic heat and carbon on long timescales. In order to accurately assess past global warming rates, the increase in ocean heat content, which stores over 90% of the total global energy imbalance (Rhein et al., 2013), needs to be precisely known.

This thesis shows the deep ocean has warmed, possibly tied to a slowdown of the bottom limb of the MOC forced by recent AABW property changes in formation. The warming of the global abysal ocean (below 4000 m) and deep Southern Ocean (below 1000 m) accounts for 16% of the observed increase in global thermal energy storage. This warming not only effects global energy budgets, but contributes to SLR through thermal expansion (thermosteric SLR). Furthermore, understanding the causes of these changes are necessary for future climate predictions under higher CO_2 emission scenarios.

1.4 Chapter summaries

The chapters that follow present global assessments of warming, freshening, and volume changes within AABW between the 1990s and 2000s and evaluate the contribution of these changes to the global energy and SLR budgets. Four independent analyses evaluate AABW warming, contraction, freshening, and the contribution of AABW changes to SLR, organized in the following manner:

Chapter 2 quantifies deep warming trends along isobars by basin and globally between the 1990s and 2000s. The primary data and regional classifications used throughout the thesis are introduced. We present a global picture of abyssal warming, with the strongest warming in the Southern Ocean and consistent warming at decreased magnitudes along three of the four deep western boundary currents. We quantify the deep warming's contribution to global heat imbalance and thermosteric SLR.

Chapter 3 looks at the same warming pattern, but recasts it in terms of a change in volume, suggesting a global slowdown in the bottom limb of the MOC. Here, we quantify a global scale contraction of AABW, presented as a rate of volume loss of AABW by basin. We find a global 8.2 Sv loss of classic AABW colder than 0 °C, seen as a ~100 m decade^{-1} fall rate of the 0 °C potential isotherm. Again, the southern loss of cold deep water propagates north along three of the four deep western boundary currents.

Chapter 4 focuses on water-mass changes in the newest formed AABW in the Southern Ocean. Here we separate the observed property changes owing to change in volume (isotherm heave) versus changes in water-mass properties, specifically salinity. We show the newly formed AABW in the south Pacific and south Indian oceans fed by RSBW and ALBW have freshened, with the strongest freshening appearing to originate from the Ross Sea. The freshening is equivalent to a 73 Gigaton yr^{-1} flux of freshwater into the deep Southern Ocean between these two basins, comparable in magnitude to fresh water mass loss rates off West Antarctica between 1992 and 2011 (Shepherd et al. 2012).

Chapter 5 quantifies the contribution of deep ocean warming and salinity changes to SLR. This analysis builds on the findings of the previous three chapters with a more comprehensive SLR analysis between 1993 and 2013. We estimate the contribution of mass addition to global SLR using the differences of full depth steric data presented in the previous three chapters from sea surface height measured from satellite altimetry. We find good agreement between this residual calculation and ocean mass changes estimated directly from changes in gravity as measured by the twin GRACE satellites between 2003 and 2013. Furthermore, we quantify the contribution of the deep ocean expansion to the SLR budget and use this result to assess the error introduced into the residual calculation that arises from ignoring deep steric SLR.

Finally, Chapter 6 concludes with a summary of the findings. It assesses what has been accomplished in this thesis and what still needs to be done to better understand recent changes in AABW.

References:

Aoki, S., S. R. Rintoul, S. Ushio, S. Watanabe, and N. L. Bindoff, 2005: Freshening of the Adélie Land Bottom water near 140 E. *Geophys. Res. Lett*, **32**, L23601, doi:10.1029/2005GL024246.

Coles, V. J., M. S. McCartney, D. B. Olson, and W. M. Smethie Jr, 1996: Changes in Antarctic Bottom Water properties in the western South Atlantic in the late 1980s. *J. Geophys. Res*, **101**, 8957–8970, doi:0.1029/95JC03721.

Comiso, J. C., and Gordon, A. L., 1987: Recurring polynyas over the Cosmonaut Sea and the Maud Rise. *J. Geophys. Res.*, **92**(C3), 2819–2833. doi:10.1029/JC092iC03p02819.

Deacon, G.E.R., 1933: A general account of the hydrology of the South Atlantic Ocean, *Discovery Reports*, **7**, 171-238.

Fahrbach, E., M. Hoppema, G. Rohardt, M. Schr der, and A. Wisotzki, 2004: Decadal-scale variations of water mass properties in the deep Weddell Sea. *Ocean Dynamics*, **54**, 77–91, doi:10.1007/s10236-003-0082-3.

Fahrbach, E., G. Rohardt, N. Scheele, M. Schroder, and V. Strass, 1995: Formation and discharge of deep and bottom water in the northwestern Weddell Sea. *Journal of Marine Research*, **53**, 515–538.

Foster, T. D., and E. C. Carmack, 1976: Frontal zone mixing and Antarctic Bottom Water formation in the southern Weddell Sea. *Deep Sea Research and Oceanographic Abstracts*, **23**, 301-317, doi:10.1016/0011-7471(76)90872-X.

Frajka-Williams, E., S. A. Cunningham, H. Bryden, and B. A. King, 2011: Variability of

Antarctic Bottom Water at 24.5°N in the Atlantic. *J. Geophys. Res*, **116**, C11026, doi:10.1029/2011JC007168.

Fukamachi, Y., S. R. Rintoul, J. A. Church, S. Aoki, S. Sokolov, M. A. Rosenberg, and M. Wakatsuchi, 2010: Strong export of Antarctic Bottom Water east of the Kerguelen plateau. *Nature Geoscience*, **3**, 327–331, doi:10.1038/ngeo842.

Fukasawa, M., H. Freeland, R. Perkin, and T. Watanabe, 2004: Bottom water warming in the North Pacific Ocean. *Nature*, **427**, 825–827, doi:10.1038/nature02337.

Ganachaud, A., and C. Wunsch, 2000: Improved estimates of global ocean circulation, heat transport and mixing from hydrographic data. *Nature*, **408**, 453–457, doi:10.1038/35044048.

Gouretski, V. V., and K. P. Koltermann, 2004: *WOCE Global Hydrographic Climatology*. Berichte des Bundesamtes für Seeschifffahrt und Hydrographie, *35*, pp. 52 + 2 CD-ROMs.

Gordon, A. L., 1982: Weddell deep water variability, *J. Mar. Res* **40**, 199-217.

Gordon, A. L. 2001: Bottom Water Formation. In Encyclopedia of Ocean Sciences, J. Steele, S. Thorpe, & K. Turekian (Eds.), (6 ed., pp. 334–340). Elsevier. doi:10.1006/rwos.2001.0006.

Hogg, N. G., G. Siedler, and W. Zenk, 1999: Circulation and Variability at the Southern Boundary of the Brazil Basin. *J. Phys. Oceanogr*, **29**, 145–157.

Jacobs, S. S., 2002: Freshening of the Ross Sea During the Late 20th Century. *Science*, **297**, 386–389, doi:10.1126/science.1069574.

Jacobs, S. S., 2004: Bottom water production and its links with the thermohaline circulation.

Antarctic Science, **16**, 427–437, doi:10.1017/S095410200400224X.

Jacobs, S. S., A. F. Amos, and P. M. Bruchhausen, 1970: Ross Sea oceanography and Antarctic bottom water formation. *Deep Sea Research Part I: Oceanographic Research Papers*, **17**, 935–962.

Jacobs, S. S., and C. F. Giulivi, 2010: Large Multidecadal Salinity Trends near the Pacific–Antarctic Continental Margin. *J. Climate*, **23**, 4508–4524, doi:10.1175/2010JCLI3284.1.

Johnson, G. C., 2008: Quantifying Antarctic Bottom Water and North Atlantic Deep Water volumes. **113**, C05027, doi:10.1029/2007JC004477.

Johnson, G. C., and S. C. Doney, 2006: Recent western South Atlantic bottom water warming. **33**, L14614, doi:10.1029/2006GL026769.

Johnson, G. C., Mecking, S., Sloyan, B. M., and Wijffels, S. E., 2007; Recent Bottom Water Warming in the Pacific Ocean, *J. Climate*, **20** (21), 5365–5375, doi:10.1175/2007JCLI1879.1

Johnson, G., Musgrave, D. L., Warren, B. A., Ffield, A., and Olson, D. B., 1998; Flow of bottom and deep water in the Amirante Passage and Mascarene Basin, *J. Geophys. Res.,* **103**(C13), 30973–30984, doi:10.1029/1998JC900027.

Johnson, G. C., S. G. Purkey, and J. L. Bullister, 2008a: Warming and Freshening in the Abyssal Southeastern Indian Ocean, **21**, 5351–5363, doi:10.1175/2008JCLI2384.1.

Johnson, G. C., S. G. Purkey, and J. M. Toole, 2008b: Reduced Antarctic meridional overturning circulation reaches the North Atlantic Ocean. *Geophys. Res. Lett*, **35**, L22601, doi:10.1029/2008GL035619.

Kawano, T., M. Fukasawa, S. Kouketsu, H. Uchida, T. Doi, I. Kaneko, M. Aoyama, and W. Schneider, 2006: Bottom water warming along the pathway of lower circumpolar deep water in the Pacific Ocean. *Geophys. Res. Lett*, **33**, L23613, doi:10.1029/2006GL027933.

Killworth, P. D., 1983: Deep Convection in the world ocean. *Reviews of Geophysical and Space Physics*, **21**, 1–26.

Kitade, Y. and Coauthors, 2014: Antarctic Bottom Water production from the Vincennes Bay Polynya, East Antarctica. *Geophys. Res. Lett*, doi:10.1002/2014GL059971.

Kouketsu, S., Doi, T., Kawano, T., Masuda, S., Sugiura, N., Sasaki, Y., et al., 2011: Deep ocean heat content changes estimated from observation and reanalysis product and their influence on sea level change. *J. Geophys. Res.*, **116**(C3), C03012. doi:10.1029/2010JC006464.

Kouketsu, S., Fukasawa, M., Kaneko, I., Kawano, T., Uchida, H., Doi, T., et al. 2009: Changes in water properties and transports along 24°N in the North Pacific between 1985 and 2005. *J. Geophys. Res.*, **114**(C1), C01008. doi:10.1029/2008JC004778.

Levitus, S., 2005: Warming of the world ocean, 1955–2003. *Geophys. Res. Lett*, **32**, L02604, doi:10.1029/2004GL021592.

Lumpkin, R., and K. Speer, 2007: Global Ocean Meridional Overturning. *J. Phys. Oceanogr*, **37**, 2550–2562, doi:10.1175/JPO3130.1.

Masuda, S., Awaji, T., Sugiura, N., Matthews, J. P., Toyoda, T., Kawai, Y., et al., 2010: Simulated Rapid Warming of Abyssal North Pacific Waters. *Science*, **329**(5989), 319–322, doi:10.1126/science.1188703.

Meredith, M. P., Garabato, A. C. N., Gordon, A. L., and Johnson, G. C., 2008; Evolution of the

Deep and Bottom Waters of the Scotia Sea, Southern Ocean, during 1995–2005,*J. Climate,* **21**(13), 3327–3343. doi:10.1175/2007JCLI2238.1.

Ohshima, K. I. and Coauthors, 2013: Antarctic Bottom Water production by intense sea-ice formation in the Cape Darnley polynya. *Nature Geoscience*, **6**, 235–240, doi:10.1038/ngeo1738.

Orsi, A. H., 2002: On the total input of Antarctic waters to the deep ocean: A preliminary estimate from chlorofluorocarbon measurements. *J. Geophys. Res*, **107**, 3122, doi:10.1029/2001JC000976.

Orsi, A. H., G. C. Johnson, and J. L. Bullister, 1999: Circulation, mixing, and production of Antarctic Bottom Water. *Progress in Oceanography*, **43**, 55–109, doi:10.1016/S0079-6611(99)00004-X.

Rhein, M., S.R. Rintoul, S. Aoki, E. Campos, D. Chambers, R.A. Feely, S. Gulev, G.C. Johnson, S.A. Josey, A. Kostianoy, C. Mauritzen, D. Roemmich, L.D. Talley and F. Wang, 2013: Observations: Ocean. In: *Climate Change 2013: The Physical Science Basis. Contribution of Working Group I to the Fifth Assessment Report of the Intergovernmental Panel on Climate Change* [Stocker, T.F., D. Qin, G.-K. Plattner, M. Tignor, S.K. Allen, J. Boschung, A. Nauels, Y. Xia, V. Bex and P.M. Midgley (eds.)]. Cambridge University Press, Cambridge, United Kingdom and New York, NY, USA.

Rintoul, S., 1998: On the origin and influence of Adelie Land Bottom Water. In: Ocean, ice and atmosphere: Interactions at the Antarctic continental margin Antarct. Res. Ser., vol. 75. AGU, Washington, DC, pp. 151–172.

Robertson, R., Visbeck, M., Gordon, A. L., and Fahrbach, E., 2002: Long-term temperature trends in the deep waters of the Weddell Sea. *Deep Sea Research Part II: Topical Studies in Oceanography*, *49*(21), 4791–4806. doi:10.1016/S0967-0645(02)00159-5

Roemmich, D., and S. L. Hautala, 1996: Northward abyssal transport through the Samoan passage and adjacent regions, J. Geophys. Res., **101**(C6), 14039–14005, DOI: 10.1029/96JC00797.

Schmitz, W. J., 1995: On the interbasin-scale thermohaline circulation. *Rev. Geophys*, **33**, 151–173, doi:10.1029/95RG00879.

Shepherd, A., Ivins, E. R., A, G., Barletta, V. R., Bentley, M. J., Bettadpur, S., et al. 2012: A Reconciled Estimate of Ice-Sheet Mass Balance. *Science*, **338**(6111), 1183–1189. doi:10.1126/science.1228102.

Sloyan, B. M., 2006: Antarctic bottom and lower circumpolar deep water circulation in the eastern Indian Ocean. *J. Geophys. Res*, **11**, doi:doi:10.1029/2005JC003011.

Sloyan, B. M., and S. R. Rintoul, 2001: The Southern Ocean Limb of the Global Deep Overturning Circulation. *J. Phys. Oceanogr*, **31**, 143–173, doi:http://dx.doi.org/10.1175/1520-0485(2001)031<0143:TSOLOT>2.0.CO;2.

Sloyan, B. M., Wijffels, S. E., Tilbrook, B., Katsumata, K., Murata, A., & Macdonald, A. M., 2013: Deep Ocean Changes near the Western Boundary of the South Pacific Ocean. *J. of Phys. Oceanogr.*, ***43***(10), 2132–2141. doi:10.1175/JPO-D-12-0182.1

Swift, J., and A. Orsi, 2012: Sixty-Four Days of Hydrography and Storms: RVIB Nathaniel B. Palmer's 2011 S04P Cruise. *oceanog*, **25**, 54–55, doi:10.5670/oceanog.2012.74.

Warren, B. A., and Johnson, G. C., 2002: The overflows across the Ninetyeast Ridge. *Deep Sea*

Research Part II: Topical Studies in Oceanography, **49**(7-8), 1423–1439. doi:10.1016/S0967-0645(01)00156-4, doi: 10.1016/S0967-0645(01)00156-4.

Whitworth, T., III, Warren, B. A., and Nowlin, W. D., Jr., 1999: On the deep western-boundary current in the Southwest Pacific Basin. *Progress in Ocenaography*, ***43***(1), 1–54. doi:10.1016/S0079-6611(99)00005-1.

Wust, G., 1935. Schichtung und Zirkulation des Atlantischen Ozeans. Die Stratophare. In: Wissenschaftliche Ergebnisse der Deutschen Atlantischen Expedition auf dem Forschungs—und Vermessungsschiff ''Meteor"1925–1927, vol. 6, first part, 2, Berlin, 180 pp. (The Stratosphere of the Atlantic Ocean, Emery, W.J. (Ed), 1978 Amerind, New Delhi, 112 pp.).

Zenk, W., and E. Morozov, 2007: Decadal warming of the coldest Antarctic Bottom Water flow through the Vema Channel. *Geophys. Res. Lett*, **34**, L14607, doi:10.1029/2007GL030340.

Zenk, W., and Visbeck, M., 2013: Structure and evolution of the abyssal jet in the Vema Channel of the South Atlantic. *Deep-Sea Research Part II*, **85**(C), 244–260, doi:10.1016/j.dsr2.2012.07.033

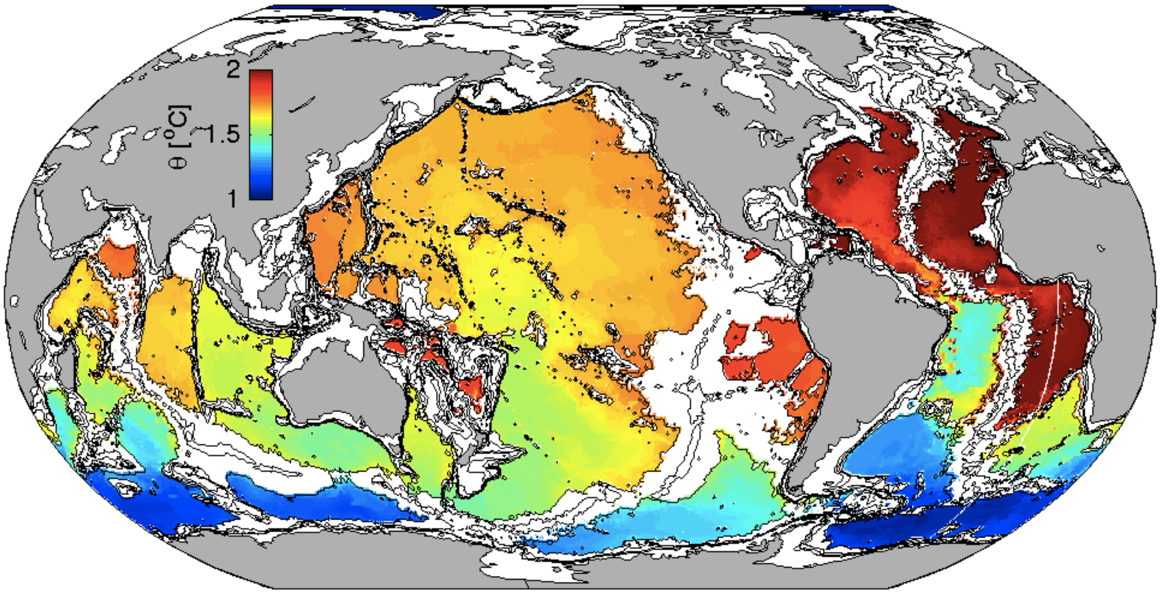

Fig. 1.1: Bottom potential temperature below 4000 m (color bar; Gouretski and Koltermann, 2004) with isobaths contoured at 1000-m intervals from the surface to 4000 m (black lines).

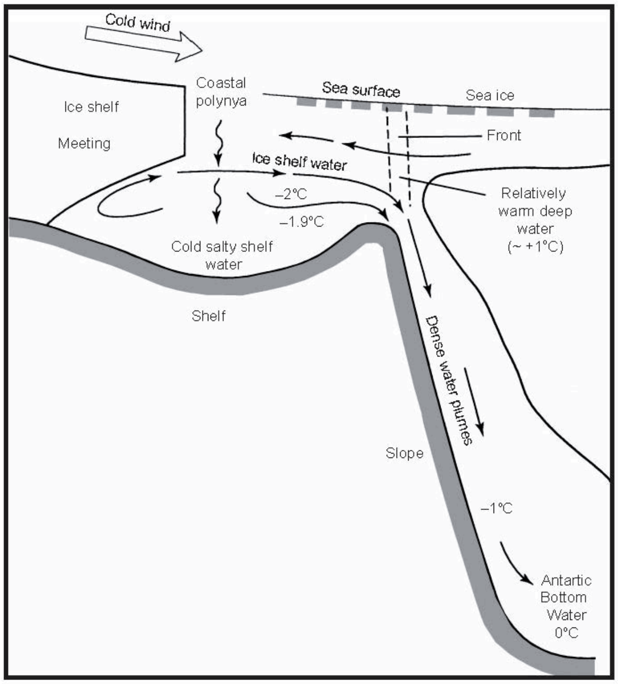

Figure 1.2: Schematic of AABW formation along the Antarctic Continental Shelf and Slope (thick gray lines) from Gordon (2001). Cold shelf water is formed through brine rejection in coastal polynyas during ice formation and export. The shelf water flows down the slope in dense plumes, mixing with ambient Warm Deep Water. Potential temperatures pertinent to Weddell Sea Bottom Water formation are given.

Chapter 2

Warming of Global Abyssal and Deep Southern Ocean Waters Between the 1990s and 2000s: Contributions to Global Heat and Sea Level Rise Budgets*

(Citation: Purkey, S. G., and G. C. Johnson. 2010. Warming of Global Abyssal and Deep Southern Ocean Waters Between the 1990s and 2000s: Contributions to Global Heat and Sea Level Rise Budgets. Journal of Climate, 23, 6336-6351, doi:10.1175/2010JCLI3682.1.)

ABSTRACT

Abyssal global and deep Southern Ocean temperature trends between the 1990s and 2000s to assess the role of recent warming of these regions in global heat and sea level budgets. We compute warming rates with uncertainties along 28 full-depth, high-quality, hydrographic sections that have been occupied two or more times between 1980 and 2010. We divide the global ocean into 32 basins defined by the topography and climatological ocean bottom temperatures and estimate temperature trends in the 24 sampled basins. The three southernmost basins show a strong statistically significant abyssal warming trend, with that warming signal weakening to the north in the central Pacific, western Atlantic, and eastern Indian Oceans. Eastern Atlantic and western Indian Ocean basins show statistically insignificant abyssal cooling trends. Excepting the Arctic Ocean and Nordic seas, the rate of abyssal (below 4000 m) global ocean heat content change in the 1990s and 2000s is equivalent to a heat flux of 0.027 (±0.009) W m^{-2} applied over the entire surface of the Earth. Deep (1000–4000 m) warming south of the Sub-Antarctic Front of the Antarctic Circumpolar Current adds 0.068 (±0.062) W m^{-2}. The

abyssal warming produces a 0.053 (±0.017) mm yr^{-1} increase in global average sea level and the deep warming south of the Sub-Antarctic Front adds another 0.093 (±0.081) mm yr^{-1}. Thus warming in these regions, ventilated primarily by Antarctic Bottom Water, accounts for a statistically significant fraction of the present global energy and sea level budgets.

2.1 Introduction

A warming climate is unequivocal, with the global top of the atmosphere radiative imbalance currently on the order of one W m^{-2}, very likely due to anthropogenic greenhouse gasses (Solomon et al. 2007). Over the past few decades, roughly 80% of the energy resulting from this imbalance has gone into heating the oceans (Levitus et al. 2005), which have a large heat capacity compared with the land or the atmosphere. This warming is important in Sea Level Rise (SLR) and other climate projections (Bindoff et al. 2007).

The Earth's radiative imbalance affects SLR in two ways (e.g., Cazanave et al. 2008; Trenberth and Fasullo 2009). Much of the heat raises ocean temperature, causing thermal expansion, termed thermosteric SLR. A much smaller portion of the heat acts to melt continental ice, adding mass to the ocean. Highly accurate satellite measurements from TOPEX/Poseidon and Jason altimetry have reported an average rate of SLR of 3.1 mm yr^{-1} between 1993 and 2003, with roughly half of that being due to thermal expansion, and half due to mass changes, mostly from melting of continental ice (Bindoff et al. 2007). However, there is still debate over the exact breakdown of SLR between thermostatic and mass addition components. Some recent SLR budgets using observations of upper ocean warming and mass changes either do not close or have high uncertainty (Miller and Douglas 2004; Raper and Braithwaite 2006), especially post-2003 (Willis et al. 2008). Other SLR and global energy budgets rely on poorly constrained deep ocean heat uptake for closure (Domingues et al. 2008; Murphy et al. 2009).

Models contain a delay between greenhouse gas forcing and surface temperature increase because of the long equilibration time of the ocean (Hansen et al. 2005). Therefore, even if greenhouse gas concentrations were kept constant at current levels, ocean temperatures and sea level would continue to rise for centuries. Furthermore, model fluxes of heat from the ocean surface layers to the deep ocean differ dramatically depending on model details. This climate sensitivity affects predictions of the magnitudes and rates of future SLR and global atmospheric warming (Raper et al. 2002; Meehl et al. 2005). Indeed, uncertainty involved in deep-ocean heat uptake may be the largest cause of variation among climate projections (Boe et al. 2009), making it vital to close observed heat and SLR budgets, including the deep ocean, for the purposes of adequately constraining predictions of and preparing for future climate change.

The deep ocean is ventilated by dense water sinking at high latitudes. North Atlantic Deep Water (NADW) is a mixture of water masses formed through deep convection processes in the Nordic and Labrador Seas (LeBel et al. 2008). Antarctic Bottom Water (AABW) is formed by a complex interaction of water masses and physical processes, with varieties produced in at least three source regions: The Weddell Sea, the Ross Sea, and the Adelie Coast (Orsi et al. 1999). While pure AABW is largely confined to the Southern Ocean, here we will refer to deep and bottom waters primarily ventilated near the Antarctic as AABW for simplicity. NADW and AABW feed the deep and abyssal limbs of the global ocean meridional overturning circulation (Lumpkin and Speer 2007).

Recent studies have revealed property changes in AABW near its source regions. In the Weddell Sea, the deep water has warmed at a rate of 0.009 °C yr^{-1} between 1990 and 1998, followed by a period of cooling (Fahrbach et al. 2004). In the Ross Sea, shelf and surface water has freshened, along with warming at mid-depths (190–440 m) and in the deep layer within the gyre (Jacobs et al. 2002; Ozaki et al. 2009; Jacobs and Giulivi 2010). Deep water off the Adelie Coast along 140°E has also shown cooling and freshening on isopycnals (Aoki et al. 2005; Rintoul 2007; Johnson et al. 2008a; Jacobs and Giulivi 2010).

Warming of AABW is not limited to the Southern Ocean. In the deep basins north of the Antarctic Circumpolar Current (ACC), AABW has also shown signs of warming, although at a reduced rate compared to the warming near the source regions. In the Atlantic Ocean, the abyssal water in the Scotia Sea, Argentine Basin, and Brazil Basin — all fed by AABW originating from the Weddell Sea — has warmed over the past two decades (Coles et al. 1996; Johnson and Doney 2006; Zenk and Morozov 2007; Meredith et al. 2008). In the southeastern Indian Ocean warming has been observed in the Australian-Antarctic Basin but little change has been seen to the north (Johnson et al. 2008a). Finally, the abyssal Southwest and Central Pacific Basins have both significantly and widely warmed over the past two decades (Fukasawa et al. 2004; Kawano et al. 2006; Johnson et al. 2007; Kawano et al. 2010). In addition to the warming, there is some evidence of recently reduced abyssal circulation in the North Atlantic (Johnson et al. 2008b) and North Pacific (Kouketsu et al. 2009; Masuda et al. 2010).

Furthermore, the upper 1000-m of the water column throughout much of the Southern Hemisphere Ocean has also warmed over the last few decades, apparently at a faster rate than the upper ocean global mean (Gille 2002; 2008; Böning et al. 2008; Sokolov and Rintoul 2009). This warming may be partly associated with a poleward migration of the ACC due to an increase in the strength and southward shift of the westerly winds that drive the ACC.

Here we make quantitative global estimates of recent (1990s to 2000s) deep and abyssal ocean warming, mostly within or originating from the Southern Ocean. We use repeat hydrographic section data to quantify temperature trends in two regions of the world's oceans: the global abyssal ocean defined here as > 4000 m in all deep basins (excluding the Arctic Ocean and Nordic Seas), and the deep Southern Ocean defined here as the region between 1000 and 4000 m south of the Sub-Antarctic Front (SAF). AABW, as defined by a water-mass analysis (Johnson 2008), dominates much of the abyssal (Fig. 2.2.1a) global ocean and deep (Fig. 2.2.1b) Southern Ocean. The abyssal Pacific and Indian Oceans are primarily composed of AABW with only a small fraction of NADW present (Fig. 2.2.1a; Johnson 2008). However, in the abyssal Atlantic, AABW dominates only in the Weddell-Enderby, Cape, Argentine, and Brazil Basins, with a small fraction persisting near the bottom of the other basins, where NADW is endemic. In the deep Southern Ocean, south of the SAF, AABW also dominates (Fig. 2.2.1b; Johnson 2008). Thus our fixed control volume (necessary for evaluating a change in heat content) contains primarily, although not solely, AABW, and allows for an estimate of warming due to changes in waters mostly of southern origin.

We describe the repeat hydrographic data and screening methodologies used in Section 2. In Section 3, we describe regional rates of temperature change and estimate their uncertainties from these data. In Section 4 we use these rates to calculate the contributions of warming primarily of southern origin to heat and SLR budgets in two ways: First, we calculate local abyssal contributions for individual ocean basins and the deep Southern Ocean (Section 4a). Second, we combine abyssal contributions from all 32 basins (assuming unsampled basins do not change) and the deep Southern Ocean for a global assessment (Section 4b). We explore the effects of variations in our 4000-m boundary between global abyssal and deep Southern Ocean volumes near the end of Section 4. We conclude with a discussion of the results in Section 5.

2.2 Data

High-quality temperature observations of the global deep ocean originate mostly from ship-based Conductivity-Temperature-Depth (CTD) instruments. The international World Ocean Circulation Experiment (WOCE) Hydrographic Programme accomplished a full-depth high-resolution high-accuracy hydrographic survey of the global ocean in the 1990s, with coast-to-coast zonal and meridional sections crossing all major ocean basins. A key subset of these sections are being reoccupied in support of the Climate Variability (CLIVAR) and carbon cycle science programs, now coordinated by the international Global Ocean Ship-based Hydrographic Investigations Program (GO-SHIP). All occupations of the repeat sections that had publicly available CTD data posted on http://cchdo.ucsd.edu as of July 2010 are considered here. Thus the data set used for this study is an aggregate of 28 full-depth, high-quality hydrographic sections that have been occupied two or more times between 1981 and 2010 (Figs. 1–2). Throughout this study sections are referred to by their WOCE IDs.

The first occupation of most sections was in the 1990s during WOCE, with subsequent occupations, mostly during the 2000s, in support of the CLIVAR and Carbon Cycle Science Programs (Fig. 2.2). The nine sections with occupations prior to 1990 were sampled during the ramp-up to WOCE with the earliest occupation considered here being the 1981 occupation of A05. The most recent occupation included in this study is also of A05, completed in February of 2010. Sections have a minimum of one occupation during WOCE followed by a second occupation 6–12 years later, with the exceptions of A01, A02, P03, and A13.5 (Fig. 2.2). Both

A01 and A02 have multiple occupations available, but only in the 1990s. P03 and A13.5 were occupied in the 1980s and 2000s but have no occupations in the 1990s. The shortest time interval between the first and last occupation of a section is 3 years, for A02, from 1994 to 1997; and the longest time interval is 29 years, for A05 from 1981 to 2010. The mean and median time differences between first and last occupations for repeat sections are 12.9 and 11.9 years.

Data collected along each section are highly accurate and well sampled in the vertical and horizontal. Vertical profiles of temperature, conductivity, and pressure were collected at each station from the surface to a depth of 10–20 m from the bottom using a CTD. Horizontal station spacing was nominally 55 km, often less over rapidly changing bathymetry. Salinity was calculated from CTD conductivity, temperature, and pressure data and calibrated to bottle samples standardized with International Association for the Physical Science of the Oceans (IAPSO) Standard Seawater using the 1978 Practical Salinity Scale (PSS-78). All temperature analysis here uses the 1968 International Practical Temperature Scale (IPTS-68), applicable to the 1980 equation of state (EOS-80). WOCE (and GO-SHIP) CTD accuracy standards are 0.002 PSS-78 for salinity, 0.002°C for temperature, and 3 dbar for pressure (Joyce, 1991). Some GO-SHIP cruises may achieve 0.001°C temperature accuracy.

We screen data prior to analysis based on two criteria. First, only data with good quality flags are used. Second, each section is visually inspected to determine if the trackline of any given occupation was close enough to those of other occupations for comparison. Here trackline refers to the zonal or meridional line along which the sampling stations fell (as opposed to the locations of the stations themselves), typically following a nominal latitude or longitude (Fig. 2.2.1). Tracklines of reoccupations of most sections used here lie within 10 km of the original, with four exceptions: First, at the west end of A05, between 69°W and 76°W, the 1998, 2004 and 2010 occupations lie ~220 km to the north of the 1981 and 1992 occupations. Second, the tracklines of the 1993 and 2003 occupations of A16 diverge by up to 88 km between 2°N and 12°N. Third, south of 20°S along P16 the tracklines are consistently ~40 km apart. Finally, between 85°W and 91°W along I05, the trackline of the 1995 occupation reaches distances as much as 55 km from the tracklines of the 2002 and 2009 occupations. These variations are deemed useable because they occur in areas of small deep horizontal density gradients. However, in other areas where tracklines diverge by less than 200 km the data are not used here because the divergences occur in regions of large deep horizontal density gradients, such as the Southern Ocean. In addition, any data from tracklines falling on opposite sides of deep ridges are not used in this study.

The sections analyzed here were not necessarily occupied in a single leg by one ship (Fig. 2.2). Many of them were broken into multiple segments that sometimes span more than a single calendar year. These segments are aggregated into a single section for this analysis. Sections with more than one occupation in a single calendar year are treated as if all stations measured in that year were from one occupation. This aggregation applies to 14 sections: the 1990, 1991, 1992, 1994, 1995, 1996, and 1997 occupations of A01; the 1988/9 occupation of A16; the 1994/5 and 2007 occupations of I08/I09; the 1995 occupation of I09S; the 1999 and 2007 occupations of P01; the 1993/4 occupation of P02; the 2005/6 occupation of P03; the 1992 and 2003 occupations of P06; the 1992/3 and 2007 occupations of P14; the 1992 and 2005 occupations of P16; the 1991/2/3 occupation of P17; the 1994 and 2008 occupations of P18; the 1994 and 2009 occupations of P21; and the 1995 occupation of SR03.

2.3 Temperature change analysis

We interpolate data for each occupation of the 28 studied sections onto closely spaced vertical and horizontal grids along their tracklines for analysis. First, potential temperature (θ) is derived from the 2-dbar CTD data at each station. The station θ profiles are then low-passed vertically with a 40-dbar half-width Hanning filter and interpolated onto a 20-dbar vertical grid. At each pressure, the data are then interpolated onto an evenly spaced standard 2' longitudinal or latitudinal grid along the section trackline using a space-preserving piecewise cubic Hermite interpolant. The horizontal grid chosen matches a 2' bathymetric dataset derived from merging satellite altimetry data and bathymetric soundings (Smith and Sandwell 1997). The bathymetric dataset and the measured CTD maximum pressures for each station are used to mask interpolated data located below the sea floor. In addition, interpolated data are discarded between any gaps in station spacing exceeding 2° of latitude or longitude along a trackline.

We calculate a rate of change in θ with time ($d\theta/dt$) at every vertical and horizontal grid point along each trackline using data from all occupations of that section where the time between the first and last occupation exceeds 2.5 years. In places with only two occupations, $d\theta/dt$ is calculated by dividing the θ change between occupations by the time between occupations. For sections with more than two occupations, at each grid point, a line is fit to θ data versus time using least squares, allowing estimates of both $d\theta/dt$ and its uncertainty from the slope of the line and its error (Fig. 2.3). Here we assume that errors owing to spatial and temporal variability discussed immediately below dominate, and so ignore the slope uncertainties and the comparatively small instrumental errors of 0.001–0.002°C. We construct pressure-latitude or pressure-longitude sections of $d\theta/dt$ estimates for each repeat section (e.g., Fig. 2.4). Generally, sections with three or more occupations evince a monotonic temperature trend with time on basin scales. For instance, the warming rates in the Southwest Pacific Basin among the three distinct pairs formed by the three occupations of P06 (a trans-Pacific section along 32°S; Fig. 2.2.1) are grossly similar (Fig. 2.5). While there is variability among the three rate estimates at any given depth and the estimate over the longest time interval is smoothest in the vertical, using any two of the three occupations would result in a similar depth-averaged rate of abyssal warming.

The $d\theta/dt$ contours along section tracklines reveal vertically banded structures extending throughout the water column (Fig. 2.4). These vertical structures are most likely due to mesoscale ocean eddies, internal waves, and tides that cause vertical displacements of isopycnals. To evaluate the statistical significance of large-scale $d\theta/dt$ patterns observed in the face of such variations, a robust estimate of a characteristic horizontal decorrelation length scale is required to calculate the effective degrees of freedom (DOF). To evaluate the length scale of these features, at every pressure level along each trackline, we remove unsampled (masked) grid points, and then find the maximum of the integral of the spatially lagged autocovariance of the spatially detrended warming rate, following Johnson et al. (2008a). Twice this integral gives an estimate of the horizontal decorrelation length scale.

The horizontal decorrelation length scale varies among sections, with values ranging from 25–400 km, but generally clustering near 160 km (Fig. 2.6). The decorrelation length scales estimated from each section are relatively constant vertically from about 500–5000 dbar because energetic vertical features in $d\theta/dt$ tend to be coherent throughout the water column. Deeper than 5000 dbar, the length scale gradually tends toward zero with depth, as the sampled region gets smaller and smaller, and there are more breaks in the sections owing to intervening topography. Shallower than 500 dbar, the length scales sometimes get longer, perhaps owing to large-scale wind-driven shifts in gyre positions or aliasing of the seasonal cycle. At each pressure surface, using repeat sections with lengths greater than 2000 km, we calculate the median of the horizontal decorrelation length scale (Fig. 2.6). There are 25 sections longer than 2000 km at the surface but this number decreases with depth to only 11 sections by 5000 dbar. Between 500 and 5000 dbar, the median is fairly constant around 163 km. The vertical mean and median between 500 and 5000 dbar are both 163 km. This value is used throughout this study as our best estimate of the horizontal length scale for all sections at all pressures. We chose the 2000-km section-length criterion based on an examination of decorrelation-length scale estimates vs. section length (not shown). For sections longer than 2000-km the decorrelation-length scale estimates asymptotically approach a common value. The criterion chosen ensures the sections used for the decorrelation length-scale estimate sample this length scale roughly a dozen times or more.

For this analysis we divide the ocean into 32 deep basins (Fig. 2.2.1) based on bottom topography (Smith and Sandwell 1997) and climatological ocean bottom temperature (Gouretski and Koltermann 2004). The boundaries for the basins follow the major ocean ridges, most of which are shallower than 3000 m. Most of the 32 deep basins were crossed by at least one section, with the exception of the Arabian Sea and Somali Basin in the northwest Indian Ocean (Fig. 2.2.1). A few marginal seas (the Sea of Okhotsk, Sea of Japan, Philippine Sea, Guatemala Basin, Panama Basin, and Gulf of Mexico) are also unsampled, but these are all mostly shallower than 4000 dbar, and thus have a minor impact on our study. The Arctic Ocean and Nordic Seas, which contain little or no AABW, were not sampled by the available repeat sections analyzed here, and thus are not included in this study.

We estimate a mean warming rate and its associated uncertainty at each pressure horizon for each of the 24 deep basins sampled (e.g., Fig. 2.7). For these estimates, we divide the sections at the basin boundaries and calculate the mean and standard deviations of the warming rates on isobars within each basin. If a basin only has one section crossing it, the means and standard deviations for the single section within the basin as a function of pressure are assumed to be representative of the whole basin. If a basin is crossed by more than one section, the length-weighted means and standard deviations are calculated using data from portions of all sections crossing that basin at each pressure level. For example, the mean *dθ/dt* for the Amundsen-Bellinghausen Basin of the Southeast Pacific (Fig. 2.7) estimates warming of about 0.002°C yr^{-1}, statistically different from zero at 97.5% confidence below about 3500 m. This result might be anticipated from examination of the warming rate along the P18 section (Fig. 2.4), which is the major contributor to this estimate, augmented only by a small portion of the southern end of P16 that also enters the basin (Fig. 2.2.1). We discuss the assumption that the length-weighted temperature trend statistics for the repeat hydrographic section tracklines crossing each basin are representative of the entire basin further in Section 5.

At each pressure level, we compute the DOF for each section crossing the basin by dividing the horizontal length of the section at that pressure by a single horizontal decorrelation length scale of 163 km. In areas where topography isolates the sampled regions such that one region is continuously sampled in the horizontal over a distance less than the decorrelation length scale, and that region is separated from adjacent sampled regions by distances more than the decorrelation length scale, the data from the region in question are assumed to be statistically independent and to contribute one DOF to the estimate. The DOF at each pressure within each basin is the sum of the DOF for all sections that cross that basin. The standard deviation is converted to a standard error by dividing by the square root of the DOF and the two-sided 95% confidence interval is estimated assuming Student's t-distribution.

In each basin where measurements do not extend to the deepest portions of that basin, the deepest estimate of *dθ/dt* is applied to the deep unsampled portions of that basin. Prior to this operation, each basin is visually inspected to make sure that the deepest estimate is well below the sill depth of that basin and that the volume of water below the deepest estimate is small compared to the volume of the basin > 4000 m. If these conditions are not met, the extension is not applied.

In addition to these basin-based warming estimates using physical topographical boundaries, we make one other estimate of *dθ/dt* for the entire Southern Ocean. We use an estimate of the location of the SAF (Orsi et al. 1995), which demarks the northern edge of the ACC, as the northern boundary for the region. Even though it is not a physical boundary, the SAF acts as a dynamical boundary separating water masses. While the SAF moves in time, and has trended south slightly over recent decades (Gille 2008; Sokolov and Rintoul 2009), a time-invariant control volume is required for heat and sea-level budgets, so motions of the SAF are not considered in this analysis. South of the SAF, isotherms rise steeply, indicating that the cold dense water of Antarctic origins found only in very deep regions to the north of the SAF extends to shallower ranges of the water column to the south of the SAF (Figs. 1b and 4). The eight meridional and one zonal section that sample regions south of the SAF (Fig. 2.2.1b) are grouped together to estimate the warming rate along pressure horizons in the Southern Ocean. The meridional sections are reasonably evenly spaced around the globe and give good coverage of the South Indian and South Atlantic Oceans. However, there is only one section in the South Pacific Ocean (P18, located on the eastern side, see Fig. 2.2.1) that approaches even the base of the Antarctic continental rise, so this region is under-represented in the final estimates of Southern Ocean changes.

The warming rate of the entire Southern Ocean south of the SAF is estimated at each pressure. Using the same method described above for basins with multiple crossings, the nine sections with data south of the SAF (Fig. 2.2.1b) are used to find the length-weighted means and 95% confidence intervals of the warming rate in the Southern Ocean. As mentioned above, due to the spatial distribution of available data, these values are somewhat biased toward θ changes in the South Indian and South Atlantic Oceans over the South Pacific Ocean and thus might be more representative of property changes originating from Weddell Sea or Adelie Land Bottom Water rather than those originating from Ross Sea Bottom Water. In addition, since not all the tracklines extend to the Antarctic continental rise (Fig. 2.2.1b), the northern portions of the Southern Ocean may also be over-represented in the warming rates for the Southern Ocean presented here.

2.4 Heat gain and sea level rise

We focus here on the effects of 1990s to 2000s warming of abyssal waters globally and deep waters in the Southern Ocean on heat gain and SLR. First, given the observed $d\theta/dt$ within a given depth range in each basin, we estimate the *local* heat flux required across the top of that depth range in each basin to account for that change and the *local* SLR implied by that change in each basin (Section 4a). Second, we make a *global* estimate of the heat flux required to account for the sum of changes in individual basins and given depth ranges expressed as if the heating were distributed evenly over the entire surface of the Earth (a climate literature convention) and, similarly, a *global* estimate of SLR expressed as a uniform change in height of the entire ocean surface (Section 4b).

In many of the basins north of the SAF, warming trends on pressure levels become significantly different from zero at 97.5% confidence below around 4000 m, making this pressure level a natural division for this study. In many of the repeat sections within the Southern Ocean consistently strong warming extends higher in the water column south of the SAF. Hence we also analyze contributions to SLR and heat gain from warming found from 1000–4000 m south of the SAF. We sum the changes found in these two regions (1000–4000 m south of the SAF and below 4000 m everywhere but the Arctic Ocean and Nordic Seas). Both of these regions are primarily ventilated by AABW (Fig. 2.2.1; Johnson 2008), so our estimates may be loosely thought of as quantifying the effects of changes in AABW on local and global heat and sea level budgets, although other Southern Ocean changes likely also play a role, as discussed in Section 5.

2.4.1 Local estimates

To calculate the *local* contribution of warming in each basin below 4000 m to the heat budget, *dθ/dt* estimates are converted to a heat flux (Q_i) through the 4000-m isobath of each basin using:

$$Q_i = \frac{\int_{4000}^{bottom} \rho \cdot C_p \cdot {}^{d\theta}\!/_{dt} \cdot a \cdot dz}{a(4000)}, \tag{1}$$

where *a* is the surface area of each depth, *z*, calculated using a satellite bathymetric dataset (Smith and Sandwell 1997). Prior to this integration, the *dθ/dt* profiles are interpolated from a pressure grid onto an evenly spaced 20-m depth grid for each basin. Profiles of density, ρ, and heat capacity, C_p, are estimated from climatological data (Gouretski and Koltermann 2004) for each basin using the mean temperature and salinity at each depth within that basin. The integral in (1) gives the total heating rate below 4000 m in each basin. Dividing by the surface area of the basin in question at 4000 m, $a(4000)$, converts the total heating rate into a flux required through the 4000-m level in that basin to account for the observed warming beneath that level in that basin (Fig. 2.8a).

We find the 95% confidence interval associated with the Q for each basin using the volume-weighted variance of Q and volume-weighted DOF for that basin. The variance (standard deviation squared) of $d\theta/dt$ at each pressure in each basin is converted to a heating rate variance by multiplying by the square of $\rho \cdot C_p$. Then the volume-weighted means for the variance and DOF below 4000 m are found using the as at each depth for weights in a vertical integration. The standard deviation is then found by taking the square root of the variance; and again the 95% confidence interval estimated assuming Student's t-distribution (Fig. 2.8a).

Similarly, we calculate the local SLR due to thermal expansion of each basin below 4000 m F_i using:

$$F_i = \frac{\int_{4000}^{bottom} \alpha \cdot {}^{d\theta}\!/_{dt} \cdot a \cdot dz}{a(4000)}, \qquad (2)$$

where α is the thermal expansion coefficient. The associated 95% confidence intervals for each F_i are estimated following a method analogous to that described above for the local heat budget estimates (Fig. 2.8b).

The geographical distributions of local basin-mean warming and cooling below 4000 m from the 1990s to the 2000s (Fig. 2.8a) and closely associated SLR changes (Fig. 2.8b) reveal a clear global pattern. Of the 24 basins with data below 4000 m, 17 warmed (nine significantly different from zero at 97.5% confidence) and seven cooled (one significantly different from zero at 97.5% confidence).

In general, a clear pattern in the magnitude of abyssal heating is seen: smaller values further to the north and larger values to the south (Fig. 2.8). The three southernmost basins: the Weddell-Enderby Basin, the Australian-Antarctic Basin, and the Amundsen-Bellinghausen Basin show strong local warming below 4000 dbar of 0.33 (±0.28), 0.25 (±0.14), and 0.15 (±0.11) W m^{-2} respectively, all significantly different from zero at 97.5% confidence. We can trace the propagation of AABW from these southernmost basins northward, and with it, a waning warming (or cooling) signal. In each of the three oceans, AABW flows generally north from basin to basin, subject to bathymetric constraints. However, the Atlantic, Indian, and Pacific Oceans each present a slightly different pattern that should be viewed with the AABW flow in mind, as discussed below.

In the Atlantic Ocean, the warming pattern follows the flow of AABW out of the Southern Ocean. AABW leaves the Weddell Sea across the South Scotia Ridge and through the Sandwich Trench traveling toward the western North Atlantic through the Argentine and Brazil Basins in the western South Atlantic (Coles et al. 1996; Orsi et al. 1999; Jullion et al. 2010). The Argentine and Brazil Basins, containing mostly AABW in the abyss (Fig. 2.2.1a; Johnson 2008), show statistically significant warming, while the abyssal western North Atlantic, which contains little AABW influence, shows only a small amount of warming, not significantly different from zero (Fig. 2.8). At the equator, deep and bottom waters cross into the Angola Basin and travel north and south filling the basins east of the Mid-Atlantic Ridge through deep passages (Warren and Speer, 1991). These eastern Atlantic basins all show abyssal cooling with the northernmost basin being the only one showing statistically significant cooling in this study. However, the dominant abyssal influence in these eastern basins is NADW, not AABW (Fig. 2.2.1; Johnson 2008). On the other hand, the strong and statistically significant recent warming in the deep

Caribbean Sea, filled with NADW that spills over a relatively shallow ~1800-m sill, is part of a trend starting a few decades prior to the 1990s (Johnson and Purkey 2009).

In the Indian Ocean both warming and cooling basins are found (Fig. 2.8). Basins to the west of the Ninetyeast Ridge mostly show deep cooling, although none of these basins exhibit cooling significantly different from zero at 97.5% confidence, while the two basins to the east of the ridge show statistically significant warming. Two of the basins west of the Ninetyeast Ridge, the Somali Basin and Arabian Sea, are not sampled. Since the deepest sills of these basins connect them to adjacent basins exhibiting cooling, one could speculate that these unsampled basins might have shown cooling had they been sampled repeatedly, although the adjacent cooling is not statistically different from zero at 97.5% confidence. As in the Atlantic, the magnitude of the warming (or cooling) in the Indian Ocean basins decreases with distance from the Southern Ocean. The warming Agulhas-Mozambique Basin, located directly south of Africa between the cooling Cape Basin in the southeast Atlantic Ocean and the cooling Crozet and Madagascar Basins in the southwest Indian Ocean, stands out as an anomaly to this pattern. Data from two tracklines crossing the dynamic Agulhas-Mozambique Basin were used in this calculation (Fig. 2.2.1a): I05 shows uniform cooling across the northeast region of the basin; but I06 alternates between warming and cooling while crossing the fronts of the ACC. Hence these data estimate overall warming in the basin, but with a large uncertainty.

In contrast to the Atlantic and Indian Oceans, the Pacific Ocean (Fig. 2.8) exhibits deep warming that is significantly different from zero at 97.5% confidence in its large central basins with more uncertain warming in most of its small peripheral basins. One of the peripheral basins shows very slight (0.01 W m^{-2}) but statistically insignificant cooling. Similarly to the other two oceans, the magnitude of the warming in the Pacific basins decreases northward from the Southern Ocean.

To complement the local estimates of warming and SLR below 4000 m, Q and F are calculated for the region between 1000–4000 m in the Southern Ocean south of the SAF, where AABW influence is also strong (Fig. 2.2.1b; Johnson 2008). Equations (1) and (2) are applied following the same procedure as described above but using the area and *dθ/dt* from the Southern Ocean. The heating between 1000 and 4000 m in the region contributes an additional 0.91 (±0.82) W m^{-2} and 0.87 (±0.76) mm yr^{-1} to the local heat flux and SLR, respectively. Adding these local changes to the heat flux and SLR below 4000 m in the Southern Ocean yields local heat gains equivalent to a local heat flux on the order of 1 W m^{-2} and SLR on the order of 1 mm yr^{-1}.

2.4.2. Global estimates

The observed *local* heat flux and SLR are combined in rough estimates of the recent abyssal and deep Southern Ocean warming's contributions to *global* heat and SLR budgets. The total heat flux and error at each depth can be calculated by summing the results from all basins using

$$Q_{abyssal} = \frac{\sum_{b=1}^{32} \rho \cdot C_p \cdot {}^{d\theta}\!/_{dt} \cdot a \cdot dz}{SA_{Earth}} \tag{3}$$

and the 95% confidence interval on that sum estimated using

$$err_{95\%} = \frac{\sqrt{\sum_{b=1}^{32} \left(\rho \cdot C_p \cdot \sigma_{{}^{d\theta}\!/_{dt}} \cdot a_b \right)^2}}{SA_{Earth}} \times 2\,, \tag{4}$$

where SA_{earth} is the total surface area of the Earth and the subscript b denotes each basin (Fig. 2.9a). The global heat flux is expressed in terms of an application to the total surface of the Earth, as is customary for global energy budget studies, rather than the surface area of the ocean.

The factor of 2 in (4) yields a conservative estimate for 95% confidence limits from Student's t-distribution. The DOF of the 24 sampled basins range from 4–283 with a mean and median of 37 and 23. The estimate in each basin is independent, making the DOF easily over 60, thus this factor could arguably be slightly less than 2. The eight basins that were not sampled are assumed to have a zero warming rate.

The contribution of the Southern Ocean Q (Fig. 2.9b) to the global heat budget can be derived by dividing by SA_{earth} instead of the basin surface area in (1). Again, we express this contribution as a uniform heat flux applied to the entire surface area of the Earth. Comparing the global heat flux (Fig. 2.9a) to the heat flux south of the SAF (Fig. 2.9b) further emphasizes the result (Fig. 2.8) that the abyssal temperature changes contribute a statistically significant fraction of the observed global change in addition to the deep Southern Ocean warming. Above 4000 m almost all the deep warming can be accounted for by warming in the Southern Ocean, again supporting the choice made here of focusing on global abyssal changes below 4000 m and Southern Ocean deep changes from 1000–4000 m.

Area-weighted mean $d\theta/dt$ profiles for the global and Southern Oceans (Figs. 9c and d) emphasize that the deep warming rate in the Southern Ocean is much larger than that in the global ocean. Also, warming temperature trends remain strong to the bottom; contributions of abyssal warming to the heat budget decrease with increasing depth primarily because the area of the ocean decreases with increasing depth.

We make an estimate of the total heat gain from recent deep Southern Ocean and global abyssal warming by adding the integral of $Q_{abyssal}$ below 4000 m to the integral of $Q_{SouthernOcean}$ from 1000–4000 m (Table 2.1). The 95% confidence interval for $Q_{abyssal}$ is calculated as the square root of the sum of the basin standard errors squared times 2, again using this factor because the DOF exceed 60. The warming below 4000 m is found to contribute 0.027 (±0.009) W m^{-2}. The Southern Ocean between 1000–4000 m contributes an additional 0.068 (±0.062) W m^{-2}, for a total of 0.095 (±0.062) W m^{-1} to the global heat budget (Table 2.1). Following the same procedure, the contribution of these warmings to SLR due to thermal expansion can be estimated using α instead of $\rho \cdot C_p$ and the surface area of the ocean instead of the surface area of the Earth. A global contribution of 0.145 (±0.083) mm yr^{-1} of SLR can be linked to this thermal expansion (Table 2.1).

The above calculations assume that the unsampled basins give zero contribution to the heat budget. We investigate the effects of two alternative scenarios on the estimates. For the first scenario, we assume that the unsampled basins have a $d\theta/dt$ profile equal to the mean $d\theta/dt$ profile of all the sampled basins. This scenario increases our global abyssal estimate by 0.0006 W m^{-2}. For the second scenario, we assume that the unsampled basins have a $d\theta/dt$ profile identical to that of the adjacent basin with the deepest connecting sill upstream in terms of abyssal flow, where the abyssal water supplying the basin in question likely originated. The two unsampled deep basins in the Indian Ocean: the Somali Basin and Arabian Sea, are assumed to be connected to the Madagascar Basin and Mid-Indian Basin, respectively. In addition, $d\theta/dt$ of the Central Pacific Basin is used for the Sea of Okhotsk, Sea of Japan, and the Coral Sea and $d\theta/dt$ of the Peru Basin is used for the Guatemala and Panama Basins. However, as mentioned earlier, all of these basins are either completely or mostly shallower than 4000 m: therefore, they have little impact on the estimates given here. The scenario decreases the global mean estimate of deep Southern Ocean and global abyssal heat gain by 0.0009 W m^{-2}. Thus, for either of these methods of accounting for the unsampled basins, the global values remain identical at the quoted precision (Table 2.1).

In addition to using 4000 m as the shallower limit for the global abyssal estimate and the deeper limit for the deep Southern Ocean estimate of warming, we also present global heat flux and SLR estimates using 3000 m and 2000 m for that dividing depth (Table 2.1). We believe that 4000 m is the more appropriate choice for quantifying primarily the effects of AABW warming. However, since the deepest known studies of ocean heat uptake of which we are aware extend only to 3000 m (Levitus et al. 2005) and the Argo array allows estimates to 2000 m since about 2003 (e.g., Von Schuckman et al. 2009), we calculate the global flux and SLR below 3000 m and 2000 m for comparison with these works. The 2000-m numbers should be used with caution. Above 3000 m, changes along a given section may be influenced by changes in the wind driven circulation (e.g., Roemmich et al. 2007), requiring better temporal and spatial sampling than available from repeat hydrography to quantify properly. Thus we may be underestimating uncertainties above 3000 m, since we may be aliasing wind-driven processes that are not captured by the spatially sparse and decadal sampling scheme.

When 3000 m is used instead of 4000 m, the same local basin patterns emerge (not shown). The only basin where the mean changes sign is the South Fiji Basin, which goes from warming at 0.00 W m^{-2} to cooling at 0.02 W m^{-2}. The error to signal ratio for local heating rates below 3000 m increases substantially in many of the basins compared with that below 4000 m, with none of the basins' cooling being statistically significant. Using a 2000-m interface depth gives an even higher abyssal heat flux (not shown), also with an even higher error to signal ratio.

Again, following (3) and (4), the recent decadal global heat gain in the deep ocean can be estimated by adding $Q_{abyssal}$ below 3000 m (or 2000 m) to the $Q_{SouthernOcean}$ between 1000 and 3000 m (or 2000 m) (Table 2.1). As expected, using this 3000-m interface the global contribution below 3000 m increases compared to that below 4000 m. The Southern Ocean contribution between 1000 and 3000 m is less than between 1000 and 4000 m. The sum, however, is roughly the same. Similarly, using the 2000-m interface depth raises the global contribution but lowers the Southern Ocean contribution, with the sum remaining roughly the same. Again, this similarity exists because most of the observed warming between 2000 and 4000 m is located in the Southern Ocean (Fig. 2.9), and therefore, choosing 4000 m, 3000 m, or 2000 m does not change the heat gained by the ocean below that interface north of the SAF. However, the partition of error associated with the estimates shifts as the interface depth is changed. The abyssal contribution has a signal 3.2 times its 95% confidence with the 4000-m interface, but only 1.7 (1.1) times its confidence using 3000 m (2000 m), because the bottom-intensified abyssal warming signal is most robust near the bottom.

2.5 Discussion

We make three large assumptions in constructing the abyssal basin estimates of heat gain and SLR below 4000 m and the deep Southern Ocean estimates of these quantities from 1000–4000 m. First, we assume that $d\theta/dt$ within a given basin or the Southern Ocean is relatively consistent over the pressure intervals considered. This assumption is often supported by examination of pressure-latitude/longitude sections of $d\theta/dt$ estimates, wherein $d\theta/dt$ is often roughly vertically uniform on deep pressure horizons, and more so below the sill depth of a basin. For example, P18 crosses four basins: the Amundsen-Bellinghausen Basin, Chile Basin, Peru Basin, and Central Pacific Basin (Fig. 2.4). The Chile and Peru basins both show uniform (but small) warming below 3000 m and exhibit little variability, while the Amundsen-Bellinghausen Basin shows stronger warming but also higher variability. Second, we assume that the tracklines used to estimate warming rates in each basin or region are representative samples of that basin. The validity of this assumption is dependent on the spatial coverage of the tracklines. In the basins that have multiple meridional and zonal crossings, this assumption seems valid. However, in a few of the basins, such as in the Philippine Sea and the Amundsen-Bellinghausen Basin, repeat sections cross only a small portion of the basin. In these cases, the changes seen in the single region are applied to the whole basin (Fig. 2.2.1). Generally, the error analysis ensures that the uncertainties for these basins, with their limited DOF, are appropriately large. The third assumption is that the timescale of the $d\theta/dt$ changes observed is longer than the intervals between occupations. This assumption generally seems valid because different sections taken over different time intervals in the same basin yield similar estimates of $d\theta/dt$ (e.g., Fig. 2.5) and a consistent large-scale geographical pattern emerges from the analysis (Fig. 2.8).

While we focus on deep warming of Antarctic origin here, the temperature and salinity of NADW also varies significantly on interdecadal time scales (Yashayaev and Clarke 2008), with implications for long-term warming (Levitus et al. 2005). Our study includes some of this recent variability, especially in the abyssal North Atlantic. However, the deep Nordic Seas have also warmed at a rate around 0.01°C yr^{-1} during the 1990s (Osterhus and Gammelsrod 1999; Karstensen et al. 2005). The local heat flux that would be needed to account for the warming in the Greenland sea below 1500 m since 1989 is on the order of 50 W m^{-2} (Karstensen et al. 2005), with a similar value for the warming in the deep Norwegian Sea starting in 1980 (Osterhus and Gammelsrod 1999). These marginal seas are neither ventilated by AABW nor sampled by repeat hydrographic data available at the CCHDO, and so are excluded from our study. However, if the Arctic Ocean and Nordic Seas had been included, the global heat flux estimates for below 2000 m, 3000 m, and 4000 m presented here could have increased.

The heating reported here is a statistically significant fraction of previously reported upper ocean heat uptake. The upper 3000 m of the global ocean has been estimated to warm at a rate equivalent to a heat flux of 0.20 W m^{-2} applied over the entire surface of the Earth between 1955 and 1998 with most of that warming contained in the upper 700 m of the water column (Levitus et al. 2005). From 1993 to 2008 the warming of the upper 700 m of the global ocean has been reported as equivalent to a heat flux of 0.64 (±0.11) W m^{-2} applied over the Earth's surface area (Lyman et al. 2010). Here, we showed the heat uptake by AABW contributes about another 0.10 W m^{-2} to the global heat budget. Thus, including the global abyssal ocean and deep Southern Ocean in the global ocean heat uptake budget could increase the estimated upper ocean heat uptake over the last decade or so by roughly 16%. Considering the ocean between 700 m and the upper limits of our control volumes could add more heat (von Schuckmann et al. 2009; Levitus et al. 2005), reducing the percentage of the contribution computed here somewhat.

The global SLR due to upper ocean thermal expansion is estimated at about 1.6 (±0.5) mm yr^{-1} (Bindoff et al. 2007) and the contribution from deep Southern Ocean and global abyssal warming estimated here is about 9% of that rate. This percentage is smaller than the relative contribution to the heat budget because the thermal expansion of seawater relative to its heat capacity is reduced at cold temperatures and deep pressures. While the warming in the global abyssal and deep Southern Ocean only contributes to a fraction of the global SLR budget, the local contribution from deep warming in some regions is similar in magnitude to the global upper ocean contribution. For instance, in the region south of the SAF, the local SLR estimate due to thermal expansion below 1000 m is over 1 mm yr^{-1} (Fig. 2.8b). The warming of the deep ocean is contributing to global and local heat and SLR budgets and needs to be considered for accurate assessments of the roles of the ocean in climate change.

Several possible mechanisms could effect the warming reported here, perhaps in combination. First, changes in buoyancy forcing in AABW formation regions could reduce formation rates or change water properties, resulting in local and remote warming (Masuda et al. 2010), possibly over long time-scales. This change may be due partly to changes in air-sea heat flux, in addition to melting continental ice (Jacobs and Guilivi 2010). Second, long-term intensification and southward movement of westerly winds that drive the ACC appear to result in southward shifts of ACC fronts, also creating warming in the Southern Ocean (Gille 2008; Sokolov and Rintoul 2009), perhaps to great depth as seen here. These stronger winds may also spin up the Weddell Gyre, increasing the temperature of abyssal waters escaping that gyre to flow northward (Jullion et al. 2010), and perhaps similarly the Ross Gyre. Finally, wind strength and position also effect ice coverage and warm water transport into formation regions, changing formation rates of AABW (Santoso and England 2007).

Abyssal warming in the Southern Ocean is likely to be at least partly caused by advection of warmer water directly from the sources. These basins are located directly downstream from the source regions for AABW and are filled on timescales captured by the data used in this study, as shown by transient tracer burdens (Orsi et al. 1999). Outside of the Southern Ocean, advection times from AABW formation regions to some abyssal locations, such as the North Pacific, can approach 1000 years (Masuda et al. 2010). However, a deep warming signal can propagate from the Southern Ocean to the North Pacific via planetary (Kelvin and Rossby) waves in less than 50 years (Nakano and Suginohara 2002), moving northward on western boundaries, eastward on the equator, then poleward at eastern boundaries, and westward into the interior (Kawase 1987). This remote warming signal could be driven by an increase and southward shift in Southern Ocean westerly winds (Klinger and Cruz 2009) or reductions in buoyancy fluxes near the AABW formation regions that decrease AABW formation rates (Masuda et al. 2010). Alternatively, the more distant changes could also be advective, resulting from changes in AABW formation centuries ago.

The local abyssal heating rates outside of the Southern Ocean (Fig. 2.8a) are comparable to geothermal heating, typically 0.05 W m^{-2} away from ridge crests, which can have a significant impact on abyssal ocean circulation and water properties (Joyce et al. 1986; Adcroft et al. 2001). However, if the ocean circulation and geothermal heat fluxes are in steady state, this heating should not cause trends in abyssal temperatures. But, if the abyssal circulation were to slow, geothermal influences might contribute to a change in abyssal temperatures and even circulation.

To gain more precise estimates of the deep ocean's contribution to sea level and global energy budgets, and to understand better how the deep and abyssal warming signals spread from the Southern Ocean around the globe, higher spatial and temporal resolution sampling of the deep ocean is required. The basin space-scale and decadal time-scale resolution of the data used here could be aliased by smaller spatial scales and shorter temporal scales. Furthermore, the propagation of the signal can only be conjectured, not confirmed, with the present observing system.

In summary, we show that the abyssal ocean has warmed significantly from the 1990s to the 2000s (Table 2.1). This warming does not occur uniformly around the globe but is amplified to the south and fades to the north (Fig. 2.8). Both the Indian and Atlantic Oceans only warm on one side, with statistically insignificant cooling on their other side. The recent decadal warming of the abyssal global ocean below 4000 m is equivalent to a global surface energy imbalance of 0.027 (±0.009) W m^{-2} with Southern Ocean deep warming contributing an additional 0.068 (±0.062) W m^{-2} from 1000–4000 m. The warming contributes about 0.1 mm yr^{-1} to the global SLR. However, in the Southern Ocean, the warming below 1000 m contributes about 1 mm yr^{-1} locally. Thus, deep ocean warming contributions need to be considered in SLR and global energy budgets.

Acknowledgments. Our heartfelt thanks go to all those who helped to collect, calibrate, and process the WOCE and GO-SHIP data analyzed here. Discussions with John Lyman were useful. Comments from Susan Hautala, Takeshi Kawano, Michael Meredith, LuAnne Thompson, Joshua Willis, Carl Wunsch, and two anonymous reviewers improved the manuscript. The findings and conclusions in this article are those of the authors and do not necessarily reflect the views of the National Oceanic and Atmospheric Administration (NOAA). The NOAA Climate Program Office and the NOAA Office of Oceanic and Atmospheric Research supported this research.

REFERENCES

Adcroft, A., J. R. Scott, and J. Marotzke, 2001: Impact of geothermal heating on the global ocean circulation. *Geophys. Res. Lett.*, **28**, 1735–1738.

Aoki, S., S. R. Rintoul, S. Ushio, S. Watanabe, and N. L. Bindoff, 2005: Freshening of the Adélie Land Bottom Water near 140°E. *Geophys. Res. Lett.,* **32**, L23601, doi:10.1029/2005GL024246.

Bindoff, N. L., J. Willebrand, V. Artale, A, Cazenave, J. Gregory, S. Gulev, K. Hanawa, C. Le Quéré, S. Levitus, Y. Nojiri, C. K. Shum, L. D. Talley, and A. Unnikrishnan, 2007: Observations: Oceanic Climate Change and Sea Level. In: *Climate Change 2007: The Physical Science Basis. Contribution of Working Group I to the Fourth Assessment Report of the Intergovernmental Panel on Climate Change* [Solomon, S., D. Qin, M. Manning, Z. Chen, M. Marquis, K.B. Averyt, M. Tignor and H.L. Miller (eds.)]. Cambridge University Press, Cambridge, United Kingdom and New York, NY, USA.

Böning, C. W., A. Dispert, M. Visbeck, S. R. Rintoul, and F. U. Schwarzkopf, 2008: The response of the Antarctic Circumpolar Current to recent climate change. *Nature Geosci.*, **1**, 864–869.

Boe, J., A. Hall, and X. Qu, 2009: Deep ocean heat uptake as a major source of spread in transient climate change simulations. *Geophys. Res. Lett.*, **36**, L22701, doi: 10.1029/2009GL040845.

Cazenave, A., A. Lombard, and W. Llovel, 2008: Present-day sea level rise: A synthesis. *Comptes rendus Geosci.,* **340** , 761–770.

Coles, V. J., M. S. McCartney, D. B. Olson, and W. M. Smethie Jr., 1996: Changes in Antarctic Bottom Water properties in the western South Atlantic in the late 1980s. *J. Geophys. Res.*, **101**, 8957–8970.

Domingues, C. M., J. A. Church, N. J. White, P. J. Gleckler, S. E. Wijffels, P. M. Barker, and J. R. Dunn, 2008: Improved estimates of upper-ocean warming and multi-decadal sea-level rise. *Nature*, **453**, 1090–1093, doi:10.1038/nature07080.

Fahrbach, E., M. Hoppema, G. Rohardt, M. Schroder, A. Wisotzki, 2004: Decadal-scale variations of water mass properties in the deep Weddell Sea. *Ocean Dynamics*, **54**, 77–91.

Fukasawa, M., H. Freeland, R. Perkin, T. Watanabe, H. Uchida, and A. Nishima, 2004: Bottom water warming in the North Pacific Ocean. *Nature*, **427**, 825–827.

Gille, S. T., 2002: Warming of the Southern Ocean since the 1950s. *Science*, **295**, 1275–1277.

Gille, S. T., 2008: Decadal-scale temperature trends in the Southern Hemisphere ocean. *J. Climate*, **21**, 4749–4765.

Gouretski, V. V., and K. P. Koltermann, 2004: *WOCE Global Hydrographic Climatology*. Berichte des Bundesamtes für Seeschifffahrt und Hydrographie, *35*, pp. 52 + 2 CD-ROMs.

Hansen, J., L. Nazarenko, R. Ruedy, M. Sato, J. Willis, A. Del Genio, D. Koch, A. Lacis, K. Lo, S. Menon, T. Novakov, J. Perlwitz, G. Russell, G. A. Schmidt, and N. Tausnev, 2005: Earth's energy imbalance: Confirmation and implications. *Science*, **308**, 1431–1435.

Jacobs, S. S., and C. F. Giulivi, 2010: Large Multi-decadal Salinity trends near the Pacific-Antarctic Continental Margin. *J. Climate,* in press, doi:10.1175/2010JCLI3284.1.

Jacobs, S. S., C. F. Giulivi, and P. A. Mele, 2002: Freshening of the Ross Sea during the late 20th century. *Science*, **297**, 386–389.

Johnson, G. C., 2008: Quantifying Antarctic Bottom Water and North Atlantic Deep Water volumes. *J. Geophys. Res*., **113**, C05027, doi: 10.1029/2007JC004477.

Johnson, G. C., and S. C. Doney, 2006: Recent western South Atlantic bottom water warming. *Geophys. Res. Lett*., **33**, L14614, doi:10.1029/2006GL026769.

Johnson, G. C., S. Mecking, B. M. Sloyan, and S. E. Wijffels, 2007: Recent bottom water warming in the Pacific Ocean. *J. Climate*, **20**, 5365–5375.

Johnson, G. C., and S. G. Purkey, 2009: Deep Caribbean Sea warming. *Deep-Sea Res. I*, **56**, 827–834, doi:10.1016/j.dsr.2008.12.011.

Johnson, G. C., S. G. Purkey, and J. L. Bullister, 2008a: Warming and freshening in the abyssal southeastern Indian Ocean. *J. Climate*, **21**, 5353–5365.

Johnson, G. C., S. G. Purkey, and J. M. Toole, 2008b: Reduced Antarctic meridional overturning circulation reaches the North Atlantic Ocean. *Geophys. Res. Letters,* **35**, L22601, doi: 10.1029/2008GL03519.

Joyce, T. M., 1991: Introduction to the Collection of Expert Reports Compiled for the WHP Program. WOCE Hydrographic operations and methods. WOCE Operations Manual. WHP Office Report WHPO-91-1, WOCE Report no. 68/91.

Joyce, T. M., B. A. Warren, and L. D. Talley, 1986: The geothermal heating of the abyssal subarctic Pacific Ocean, *Deep-Sea Res*., **33**, 1003–1015.

Jullion, L., S. C. Jones, A. C. Naveira Garaboto, and M. P. Meredith, 2010: Wind-controlled export of Antarctic Bottom Water from the Weddell Sea. *Geophys. Res. Letters*, **37**, L09609, doi:10.1029/2010GL042822.

Karstensen, J., P. Schlosser, D. W. R. Wallace, J. L. Bullister and J. Blindheim, 2005: Water mass transformation in the Greenland Sea during the 1990s. *J. Geophys. Res.*, **110**, C07022, doi: 10.1029/2004JC002510.

Kawano, T., T. Doi, H. Uchida, S. Kouketsu, M. Fukasawa, Y. Kawai, and K. Katsumata, 2010: Heat content change in the Pacific Ocean between the 1990s and 2000s. *Deep-sea Res. II,* **57**, 1141–1151, doi:10.1016/j.dsr2.2009.12.003 .

Kawano, T., M. Fukawasa, S. Kouketsu, H. Uchida, T. Doi, I. Kaneko, M. Aoyama, and W. Scheider, 2006: Bottom water warming along the pathways of lower circumpolar deep water in the Pacific Ocean. *Geophys. Res. Lett*., **33**, L23613, doi:10.1029/2006GL027933.

Kawase, M., 1987: Establishment of Deep Ocean Circulation Driven by Deep-Water Production. *J. Phys. Oceanogr*., **17**, 2294–2317

Klinger, B. A., and C. Cruz, 2009: Decadal response of global circulation to Southern Ocean zonal wind stress perturbation. *J. Phys. Oceanogr*., **39**, 1888–1904, doi: 10:1175/2009JPO4070.1.

Kouketsu, S., M. Fukasawa, I. Kaneko, T. Kawano, H. Uchida, T. Doi, M. Aoyama, and K. Murakami, 2009: Changes in water properties and transports along 24°N in the North Pacific between 1985 and 2005. *J. Geophys. Res.*, **114**, C01008, doi:10.1029/2008JC004778.

LeBel, D. A., W. M. Smethie Jr., M. Rhein, D. Kieke, R. A. Fine, J. L. Bullister, D.-H. Min, W. Roether, R. F. Weiss, C. Andrié, D. Smythe-Wright, E. P. Jones, 2008: The formation rate of North Atlantic Deep Water and Eighteen Degree Water calculated from CFC-11 inventories observed during WOCE. *Deep-Sea Res. I,* **55**, 891–910.

Levitus, S., J. Antonov, and T. Boyer, 2005: Warming of the world ocean, 1955–2003. *Geophys. Res. Lett.,* **32**, L02604, doi: 10:1029.2004GL021592.

Lumpkin, R., and K. Speer, 2007: Global Ocean meridional overturning. *J. Phys. Oceanogr*., **37**, doi: 10:1175/JPO3130.1.

Lyman, J. M., S. A. Good, V. V. Gouretski, M. Ishii, G. C. Johnson, M. D. Palmer, D. A. Smith, and J. K. Willis, 2010: Robust warming of the global upper ocean. Nature, **465**, 334–337, doi:10.1038/nature09043.

Masuda, S., T. Awaji, N. Sugiura, J. P. Matthews, T. Toyoda, Y. Kawai, T. Doi, S. Kauketsu, H. Igarashi, K. Katsumata, H. Uchida, T. Kawano, and M. Fukasawa, 2010: Simulated rapid warming of abyssal North Pacific water. *Science*, **329**, 319–322, doi: 10.1126/science.1188703.

Meehl. G. A., W. M. Washington, W. D. Collins, J. M. Arblaster, A. Hu, L. E. Budja, W. G. Strand, and H. Teng, 2005: How much more Global Warming and sea level rise? *Science*, **307**, 1769–1772.

Meredith, M. P., A. C. Naveira Garabato, A. L. Gordon, and G. C. Johnson, 2008: Evolution of the Deep and Bottom Water of the Scotia Sea, Southern Ocean, during 1995–2005. *J. Climate*, **21**, 3327–3343.

Miller, L., and B. C. Douglas, 2004: Mass and volume contributions to twentieth-Century global sea level rise. *Nature*, **248**, 406–409.

Murphy, D. M., S. Solomon, R. W. Portmann, K. H. Rosenlof, P. M. Forster, and T. Wong, 2009: An observationally based energy balance for the Earth since 1950. *J. Geophys. Res.*, **114**, D17107, doi:10.1029/2009JD012105.

Nakano, H., and N. Suginohara, 2002: Importance of the eastern Indian Ocean for the abyssal Pacific. *J. Geophys, Res.*, **107**, 3219, doi:10.1029/2001JC001065.

Orsi, A. H., G. C. Johnson, and J. L. Bullister, 1999: Circulation, mixing, and production of Antarctic Bottom Water. *Prog. Oceanogr.*, **43**, 55–109.

Orsi, A. H., T. Whitworth III, and W. D. Nowlin, Jr., 1995: On the meridional extent and fronts of the Antarctic Circumpolar Current. *Deep-Sea Res. I*, **42**, 641–673.

Osterhus, S., and T. Gammelsrod, 1999: The abyss of the Nordic Seas is warming. *J. Climate*, **12**, 3297–3304.

Ozaki H., H. Obata, M. Naganobu, and T. Gamo, 2009: Long-term bottom water warming in the North Ross Sea. *J. Oceanogr.,* **65**, 235–244.

Raper, S. C. B., and R. J. Brathwaite, 2006: Low sea level rise projections from mountain glaciers and icecaps under global warming. *Nature*, **439**, 311–313.

Raper, S. C. B., J. M. Gregory, and R. J. Stouffer, 2002: The role of climate sensitivity and ocean heat uptake on AOGCM transient temperature response. *J. Climate,* **15**, 124–130.

Rintoul, S. R., 2007: Rapid freshening of Antarctic Bottom Water formed in the Indian and Pacific Oceans. *Geophys. Res. Lett.*, **34**, L06606, doi:10.1029/2006GL028550.

Roemmich, D., J. Gilson, R. Davis, P. Sutton, S. Wijffels, and S. Riser, 2007: Decadal Spinup of the South Pacific Subtropical Gyre. *J. Phys. Oceanogr.*, **37**, 162–173. doi:10.1175/JPO3004.1.

Santoso A., and M. H. England, 2008: Antarctic Bottom Water Variability in a coupled climate model. *J. Phys. Oceanogr.*, **38**, 1870–1893, doi: 10:1175/2008JPO3741.1.

Smith, W. H. F., and D. T. Sandwell, 1997: Global seafloor topography from satellite altimetry and ship depth soundings. *Science*, **277**, 1956–1962.

Sokolov, S., and S. R. Rintoul, 2009: Circumpolar structure and distribution of the Antarctic Circumpolar Current fronts: 2. Variability and relationship to sea surface height. *J. Geophys. Res*., 114, C11019, doi:10.1029/2008JC005248.

Solomon, S., D. Qin, M. Manning, Z. Chen, M. Marquis, K. B. Averyt, M. Tignor, and H.L. Miller (eds.), 2007: Climate Change 2007: The Physical Basis. Contribution of Working Group I to the Fourth Assessment Report of the Intergovernmental Panel on Climate Change**,** Cambridge University Press, Cambridge, United Kingdom and New York, NY, USA.

Trenberth, K. E, and J. T. Fasullo, 2009: Changes in the flow of energy through the Earth's climate system. *Meteorologische Zeitschrift*, **18**, 369–377.

von Schuckmann , K., F. Gaillard, and P.-Y. Le Traon, 2009: Global hydrographic variability patterns during 2003–2008, *J. Geophys. Res.*, **114**, C09007, doi:10.1029/2008JC005237.

Warren, B. A., and K. G. Speer, 1991: Deep circulation in the eastern South Atlantic Ocean. *Deep-Sea Res.*, **38(Suppl.)**, S281–S322.

Willis, J. K., D. P. Chambers, and R. S. Nerem, 2008: Assessing the globally averaged sea level budget on seasonal to interannual timescales. *J. Geophys. Res.,***113**, C06015, doi:10.1029/2007JC004517.

Yashayaev, I., and A. Clarke, 2008: Evolution of North Atlantic water masses inferred from Labrador Sea salinity series. *Oceanogr.*, **21**, 30–45.

Zenk, W., and E. Morozov, 2007: Decadal warming of the coldest Antarctic Bottom Water flow through the Vema Channel. *Geophys. Res. Lett.*, *34*, L14607, doi:10.1029/2007GJ030340.

Interface depth (m)	**Heat (W m^{-2})**			**SLR (mm yr^{-1})**		
	Global: below interface depth	**South of SAF: 1000-interface depth**	**Total**	**Global: below interface depth**	**South of SAF: 1000-interface depth**	**Total**
2000	0.068 (±0.061)	0.032 (±0.026)	0.099 (±0.066)	0.113 (±0.100)	0.037 (±0.030)	0.150 (±0.104)
3000	0.053 (±0.031)	0.051 (±0.047)	0.104 (±0.056)	0.097 (±0.055)	0.063 (±0.060)	0.161 (±0.081)
4000	0.027 (±0.009)	0.068 (±0.062)	0.095 (±0.062)	0.053 (±0.017)	0.093 (±0.081)	0.145 (±0.083)

TABLE 2.1. Heat fluxes (and uncertainties at 95% confidence) applied over the entire surface area of the Earth required to explain the recent decadal observed temperature changes for the global ocean below the interface depth, the ocean south of the Sub-Antarctic Front (SAF) between 1000 m and the interface depth, and the sum of the previous two terms. Similarly, mean sea level rise (SLR) for the global ocean due to the thermal expansion estimated from the recent decadal temperature changes observed in the three regions described above.

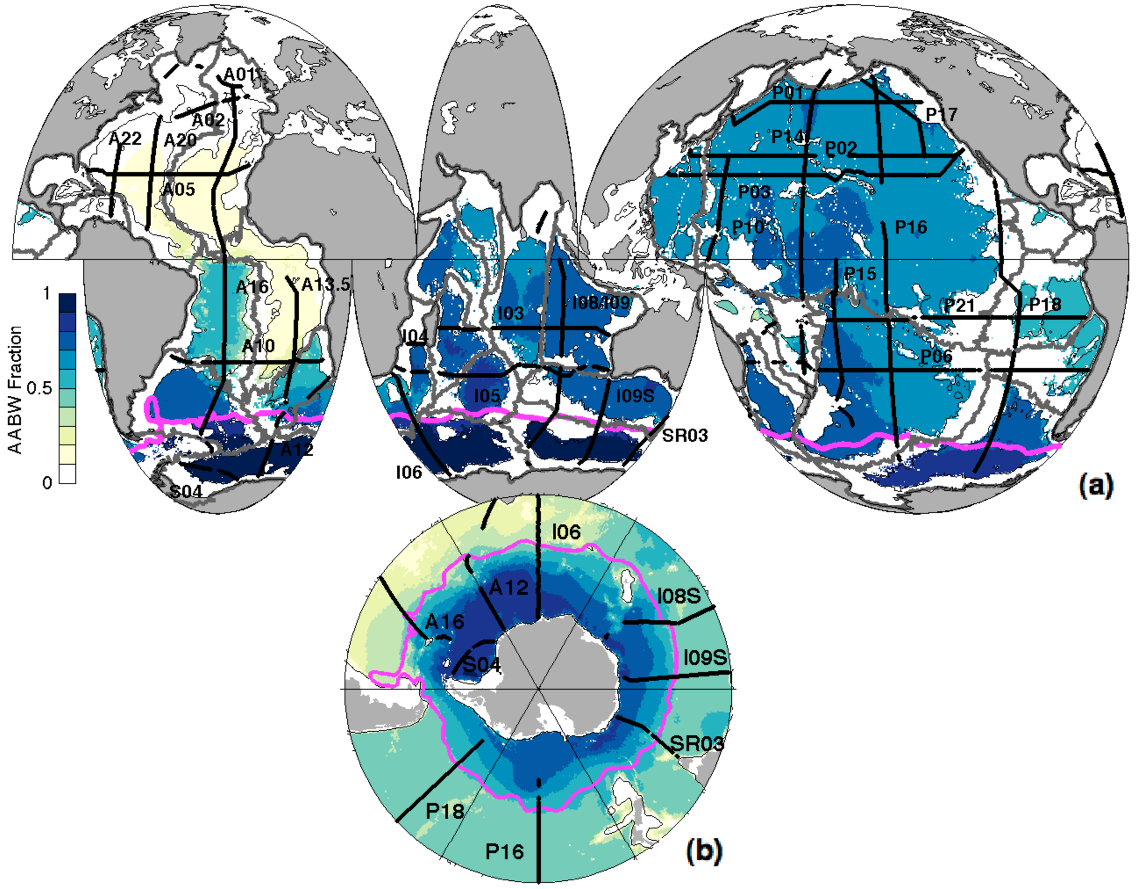

FIG. 2.1. (a) Tracklines of the 28 repeated sections studied (black lines) with WOCE designators noted adjacent. Basin boundaries are outlined (gray lines) over the depth-averaged fraction of AABW below 4000 m (colorbar) after Johnson (2008). The Sub-Antarctic Front (SAF; Orsi et al. 1995) position (magenta line) and the 4000-m isobath (thin black lines) are also shown. (b) Same as (a) but a polar projection with tracklines of the 9 repeated sections that extend south of the SAF plotted over the depth-averaged fraction of AABW from 1000 – 4000 m with the 1000-m isobath and without basin boundaries.

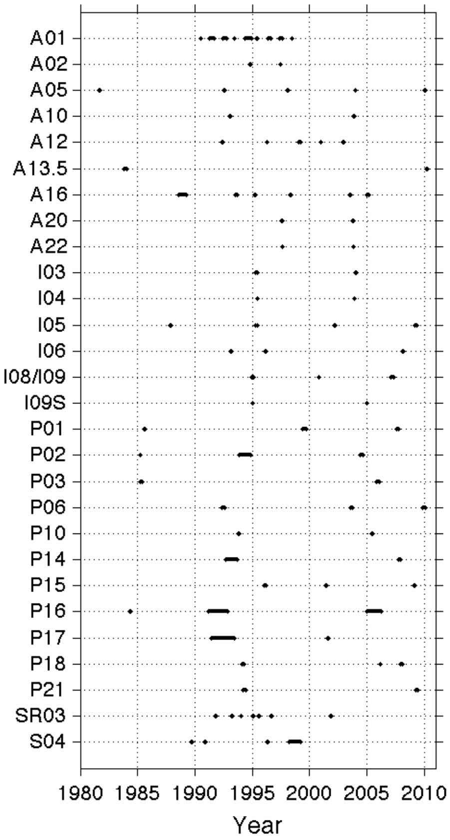

FIG. 2.2. Occupation dates for each of the 28 repeated sections analyzed here listed by their WOCE designators (see Fig. 2.2.1 for locations). Lines extend over the entire time period over which data were collected for a given occupation of a section. Longer lines indicate where multiple legs of sections taken over the course of up to a year or more are joined.

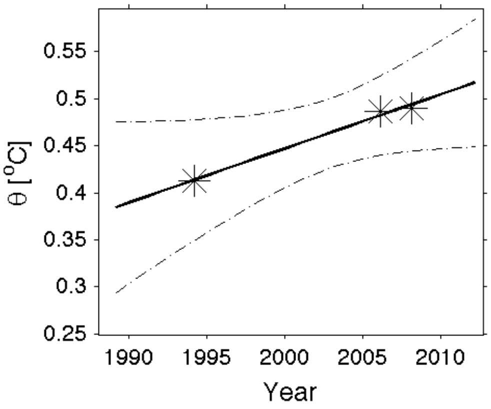

FIG. 2.3. Local *dθ/dt* estimate for a location with more than two section occupations. Potential temperature data (asterisks) from three occupations along P18 (see Fig. 2.4, green asterisk, for location) at 56°S and 4000 dbar plotted vs. time are used to fit a line by least squares (solid line), producing an error estimate here shown at 95% confidence limits (dotted line). The slope of the line is *dθ/dt*.

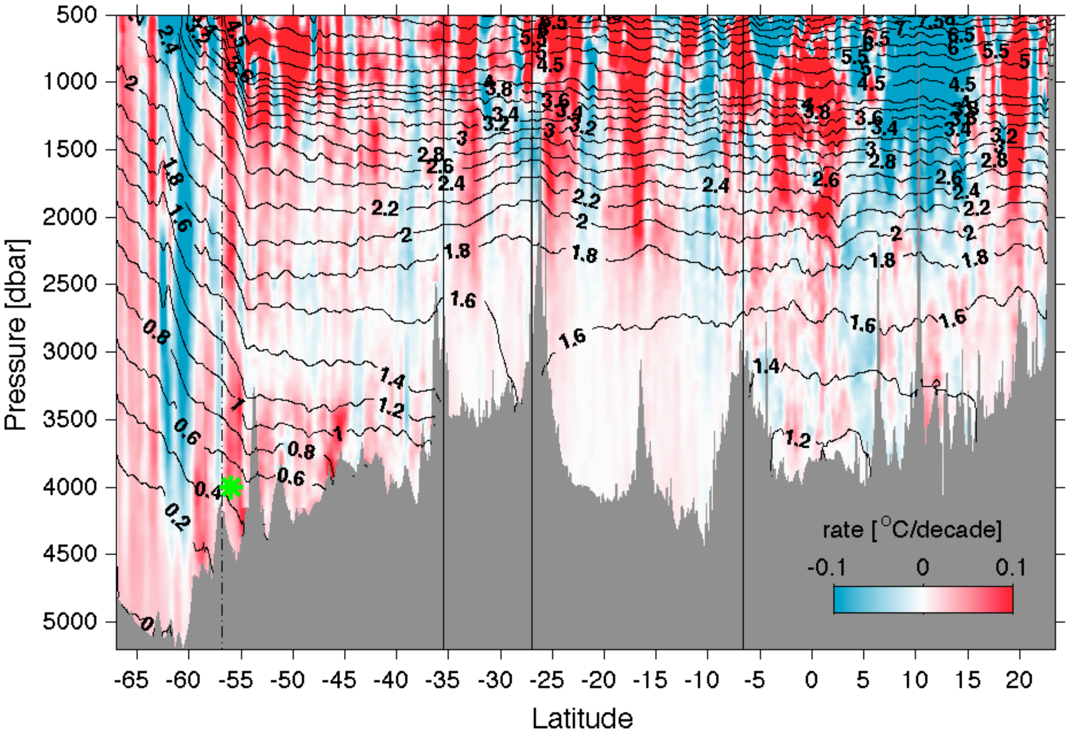

FIG. 2.4. Time rate of change of θ, $d\theta/dt$ (colorbar), along the trackline of P18 (see Fig. 2.2.1 for location). Areas of warming are shaded in red and regions of cooling are shaded in blue with intensity scaled by the magnitude of the change. Mean θ values over all occupations are contoured (black lines). This trackline is grouped into four basins for analysis (boundaries shown by vertical black lines), and the area south of the SAF (vertical dot-dashed line) is also analyzed separately. The basins from south to north are the Amundsen-Bellinghausen Basin, Chile Basin, Peru Basin, and Central Pacific Basin. Green asterisk denotes location of data used in Fig. 2.3.

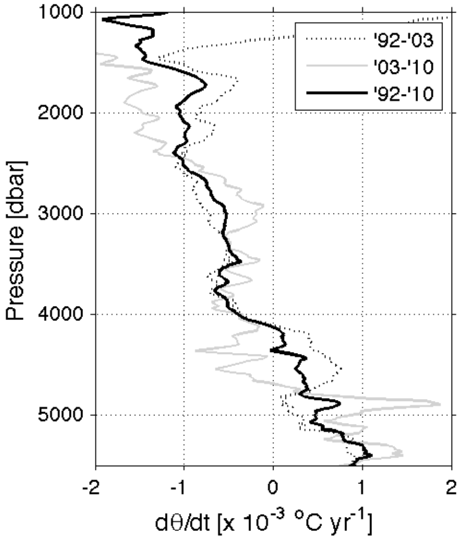

FIG. 2.5. Mean time rate of change in *θ*, *dθ/dt*, at each pressure along the portion of P06 crossing the Southwest Pacific Basin (Fig. 2.2.1) calculated using every combination of pairs of the three occupations of P06 (see legend).

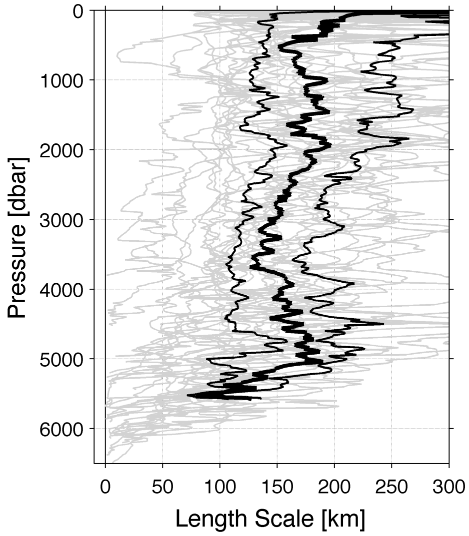

FIG. 2.6. Horizontal decorrelation length scales (km) of *dθ/dt* for each of the 28 repeat sections (gray lines) calculated at each pressure. The median (thick black line) and quartiles (thin black lines) are calculated from all sections with horizontal lengths greater than 2000 km at a given pressure. The pressure-averaged mean and median of the length scale from 500–5000 dbar is 163 km.

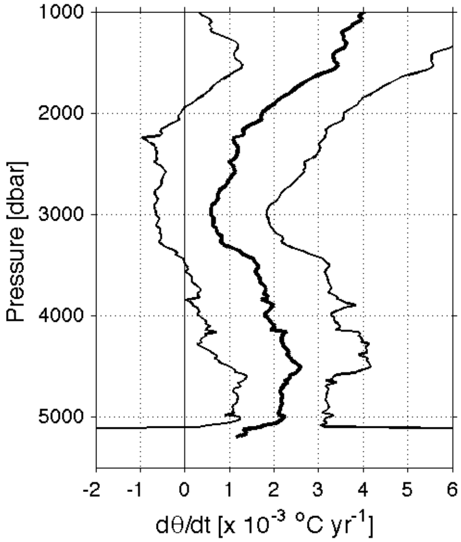

FIG. 2.7. Mean (thick black line) and 95% confidence limits (thin black lines) of *dθ/dt* for the Amundsen-Bellinghausen Basin calculated as described in the text – a length-weighted combination of the portions of repeated sections that cross the basin (in this instance P18 and P16, see Fig. 2.2.1 for locations).

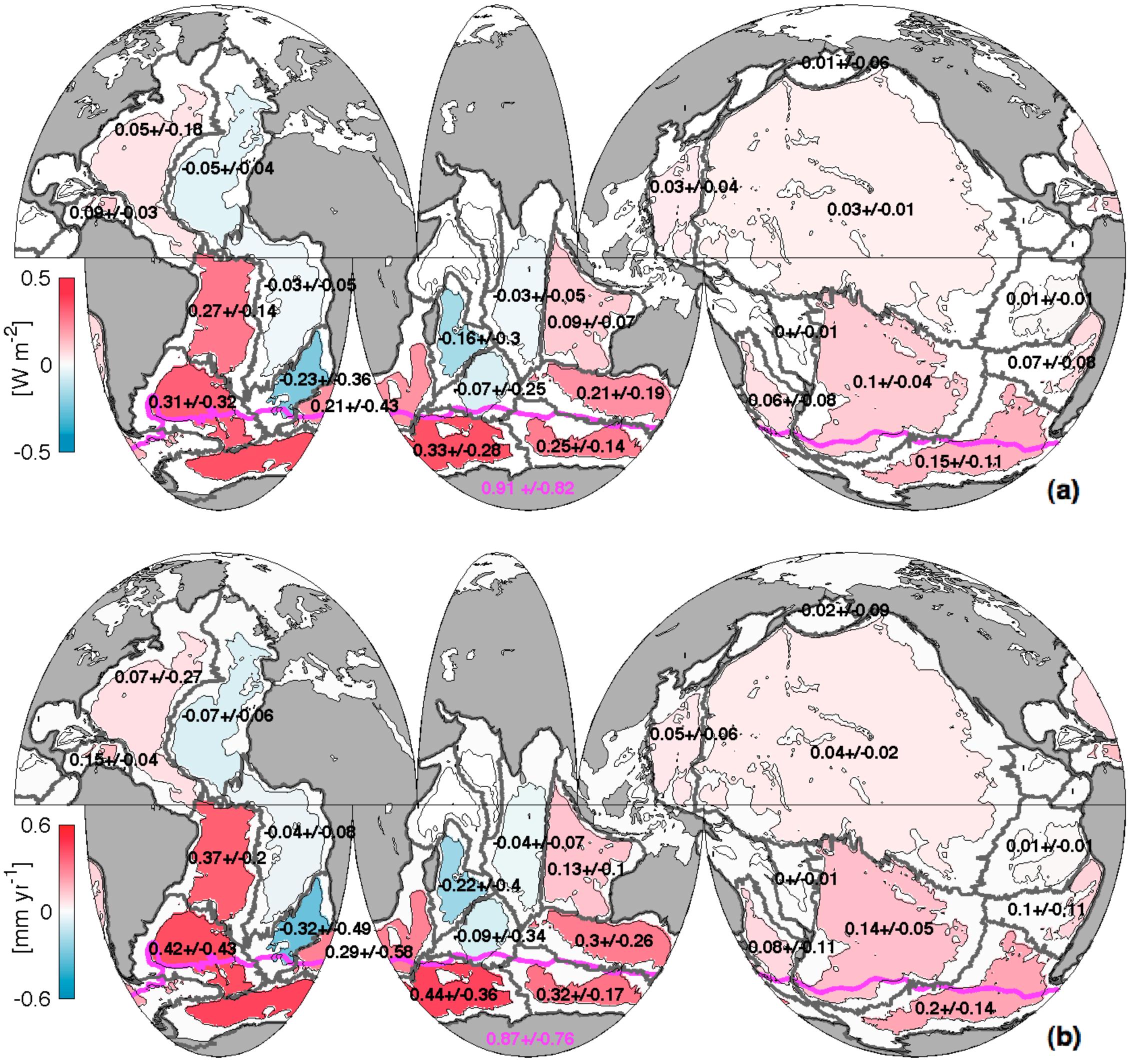

FIG. 2.8. (a) Mean local heat fluxes through 4000 m implied by abyssal warming below 4000 m from the 1990s to the 2000s within each of the 24 sampled basins (black numbers and colorbar) with 95% confidence intervals and the local contribution to the heat flux through 1000 m south of the SAF (magenta line) implied by deep Southern Ocean warming from 1000–4000 m is also given (magenta number) with its 95% confidence interval. (b) Similarly, basin means of Sea Level Rise (SLR) from the 1990s to the 2000s due to abyssal thermal expansion below 4000 m and deep thermal expansion in the Southern Ocean from 1000–4000 m south of the SAF. Basin boundaries (thick gray lines) and 4000-m isobath (thin black lines) are also shown.

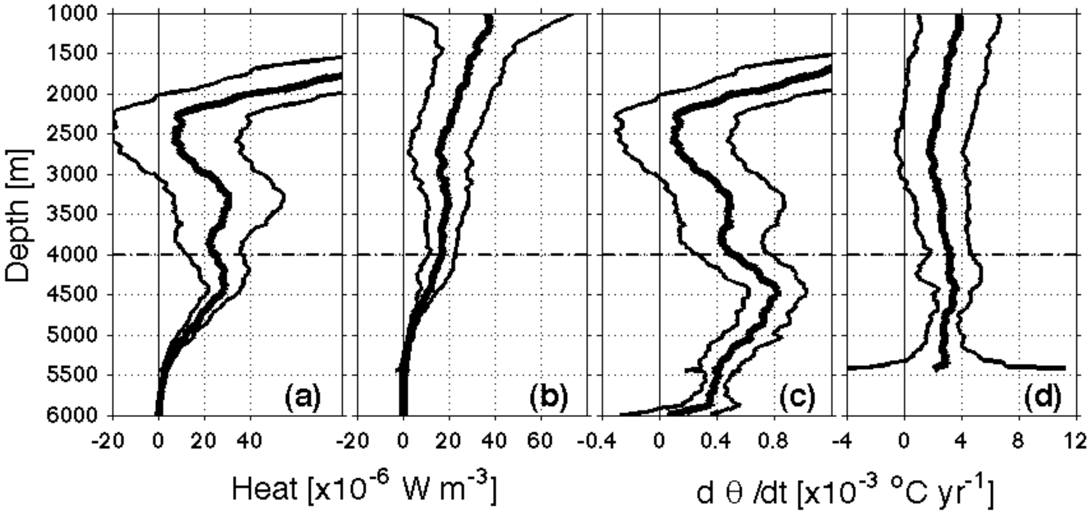

FIG. 2.9. Profiles of heat gain per meter (thick lines) with 95% confidence intervals (thin lines) estimated as described in (3) for (a) the global ocean and (b) the Southern Ocean south of the SAF. Area-weighted mean profiles of *dθ/dt* for (c) the global ocean and (d) the Southern Ocean south of the SAF.

Chapter 3

Global contraction of Antarctic Bottom Water between the 1980s and 2000s

(Citation: Purkey, S. G. and G. C. Johnson, 2012: Global contraction of Antarctic Bottom Water between the 1980s and 2000s. Journal of Climate, 25, 5830-5844, doi:10.1175/JCLI-D-11-00612.1.)

ABSTRACT

A statistically significant reduction in Antarctic Bottom Water (AABW) volume is quantified between the 1980s and 2000s within the Southern Ocean and along the bottom-most, southern branches of the Meridional Overturning Circulation (MOC). AABW has warmed globally during that time, contributing roughly 10% of the recent total ocean heat uptake. This warming implies a global-scale contraction of AABW. Rates of change in AABW-related circulation are estimated in most of the world's deep ocean basins by finding average rates of volume loss or gain below cold, deep potential temperature (θ) surfaces using all available repeated hydrographic sections. The Southern Ocean is losing water below $\theta = 0°C$ at a rate of -8.2 (±2.6) $\times 10^6$ m^3 s^{-1}. This bottom water contraction causes a descent of potential isotherms throughout much of the water column until a near-surface recovery, apparently through a southward surge of Circumpolar Deep Water from the north. To the north, smaller losses of bottom waters are seen along three of the four main northward outflow routes of AABW. Volume and heat budgets below deep, cold θ surfaces within the Brazil and Pacific basins are not in steady state. The observed changes in volume and heat of the coldest waters within these basins could be

accounted for by small decreases to the volume transport or small increases to θ of their inflows, or fractional increases in deep mixing. The budget calculations and global contraction pattern are consistent with a global scale slowdown of the bottom, southern limb of the MOC.

3.1 Introduction

The Meridional Overturning Circulation (MOC) may play a significant role in climate change (e.g., Meehl et al. 2006) and the deep ocean plays a significant role in ocean heat storage (Levitus et al. 2005; Purkey and Johnson 2010). The strength of the MOC determines the ability of the deep ocean to absorb and store anthropogenic heat and carbon (e.g., Sigman and Boyle 2000; Russell et al. 2006). While the MOC has often been considered to be in steady state in recent decades, rates of deep and bottom water production and circulation were dramatically different during the Last Glacial Maximum, and changes in the MOC have been linked to periods of rapid climate change (e.g., Clark et al. 2002; Lynch-Stieglitz et al. 2007). Models suggest the MOC will slow under global warming scenarios, possibly producing large regional variations in surface temperatures (Solomon et al. 2007). Furthermore, climate models differ widely in their projections of how much heat the deep ocean will absorb under global warming, causing a large spread in future climate projections (Boe et al. 2009).

Cold, dense water formed at high latitudes feeds the deep and bottom limbs of the MOC (Lumpkin and Speer 2007). North Atlantic Deep Water (NADW) is a combination of water masses formed in the Labrador and the Nordic seas (LeBel et al. 2008). NADW travels south at depth until it enters the Antarctic Circumpolar Current (ACC) and rises, as seen by the distinct signature of warm, salty water at mid- and upper depths (Orsi et al. 1995; Johnson 2008). In the southern hemisphere, the densest bottom water, Antarctic Bottom Water (AABW), that underlies

NADW is also a mixture of water masses, and is formed in at least three locations along the Antarctic shelf (Orsi et al. 1999). At each location, physical mechanisms including ice formation, surface cooling, and mixing with ambient water as it cascades down the continental slope (Foster and Carmack 1976) create a distinct variety of AABW. Each AABW variety enters the lower ACC, further mixing with overlying water, and leaves the Southern Ocean as a slightly less dense water mass (Orsi et al. 1999), here still referred to as AABW. AABW flows north, filling the deepest portions of the Pacific, Indian, and western Atlantic oceans (Johnson 2008).

The bottom, southern limb of the MOC transports roughly 20 Sv ($1\ \text{Sv} = 1 \times 10^6\ \text{m}^3\ \text{s}^{-1}$) northward out of the Southern Ocean (Lumpkin and Speer 2007), primarily in four deep western boundary currents (DWBCs; Fig. 3.1). Chlorofluorocarbon-11 (CFC-11) inventories confirm that true AABW and other warmer, lighter water masses formed in the Southern Ocean contribute about 21 Sv to this MOC limb (Orsi et al. 2002). Inverse models estimate northward transports of AABW into the Pacific, Atlantic, and Indian oceans from 7–11, 5–6, and 8–10 Sv, respectively, although definitions of AABW density and the location of the Southern Ocean boundary vary slightly among studies (Ganachaud and Wunsch 2000; Sloyan and Rintoul 2001; Lumpkin and Speer 2007). Velocity measurements within DWBCs along the Kerguelen Plateau in the Indian Ocean and north of the Falkland Plateau in the Atlantic Ocean imply northward transports of ~8 Sv of water for $\theta \leq 0.2$°C in each, but with high temporal variability (Whitworth et al. 1991; Fukamachi et al. 2010). In the Pacific, velocity measurements at 32°S have shown the DWBC to transport 15.8 (±9.2) Sv of bottom and deep waters, mostly of southern origin, northward (Whitworth et al. 1999).

Numerous studies have shown that the Southern Ocean has warmed significantly throughout the water column. The upper 1000 m of the Southern Ocean has warmed faster than the upper ocean global mean rate between the 1950s and 2000s (Gille 2002; 2008; Böning et al. 2008). Below 1000 m, the deep ocean has warmed by ~0.03°C decade^{-1} south of the Subantarctic Front between the 1980s and 2000s (Purkey and Johnson 2010). In addition, previous studies have shown property changes in AABW and its components near its source regions. In the Weddell Gyre, Warm Deep Water (WDW), Weddell Sea Deep Water (WSDW), and Weddell Sea Bottom Water (WSBW) have all exhibited warming trends since 1990, although, more recently, WDW has fluctuated between warming and cooling (Robertson et al. 2002; Fahrbach et al. 2004; 2011). In addition, glacier melt has freshened shelf water near the deep-water formation regions in the Weddell Sea (Hellmer et al. 2011). In the Ross Sea, shelf water and bottom water have freshened over the past 50 years (Jacobs and Comiso 1997; Jacobs and Giulivi 2010). Finally, bottom waters off the Adelie Coast have cooled and freshened on isopycnals between the mid-1990s and mid-2000s (Aoki et al. 2005; Rintoul 2007; Johnson et al. 2008a; Jacobs and Giulivi 2010).

Warming of AABW has also occurred along its spreading paths outside of the Southern Ocean (Purkey and Johnson 2010; Kouketsu et al. 2011). Regional studies within the Scotia Sea, Brazil Basin, Argentine Basin, Australian-Antarctic Basin, Pacific Basin, and Southwest Pacific Basin have all shown significant warming of AABW over the past few decades (Coles et al. 1996; Fukasawa et al. 2004; Johnson and Doney 2006; Kawano et al. 2006; Johnson et al. 2007; Zenk and Morozov 2007; Johnson et al. 2008a; Meredith et al. 2008; Kawano et al. 2010). On average, the deep ocean below 4000 m has absorbed ~0.03 W m^{-2} (expressed as a flux over the entire surface area of Earth) between the 1980s and 2000s with stronger warming near the source regions (Purkey and Johnson 2010). The deep ocean heat uptake, which is often neglected in heat and sea level rise budgets, is important in quantifying Earth's net energy imbalance (e.g., Willis et al. 2008; Church et al. 2011). In climate models, periods of decreased upper ocean heat uptake (and pauses in global average surface warming) are characterized by increases in deep ocean heat uptake (Meehl et al. 2011), further emphasizing the importance of accurately quantifying total ocean heat uptake, not just the upper few hundred meters.

It is difficult to quantify past effects of global warming on the MOC strength directly owing to a lack of the data needed to determine its historical strength and natural variability (Kanzow et al. 2007). Using data from multiple occupations of a single zonal hydrographic section across the North Atlantic, Bryden et al. (2005) found a 30% reduction in the upper, northern limb of the MOC from 1957 to 2003. However, mooring array data later showed short-term variability to be larger than the previously reported long-term trend from the temporally sparse section data, calling the previous results into question (Cunningham et al. 2007). Using the western halves of most of the occupations of this same section, a decrease in transport in the bottom, southern limb of the MOC carrying AABW northward into the North Atlantic has been reported from 1983 to 2003 (Johnson et al. 2008b), with evidence of a partial rebound in 2010 (Frajka-Williams et al. 2011). While this limb of the MOC may exhibit less temporal variability so far from its source, these transport estimates were still made using geostrophic shear and relying upon an inferred level of no motion. Similarly, a decreasing trend in northward bottom water transport across 24°N in the Pacific has been suggested between 1985 and 2005 (Kouketsu et al. 2009).

However, deep warming signals on pressure surfaces also imply deepening potential isotherms – changes in the vertical distribution of water masses through the water column (Kouketsu et al. 2009; 2011; Masuda et al. 2010). These changes have been attributed to a decrease in bottom water export from the Southern Ocean into deep ocean basins (Masuda et al. 2010; Kouketsu et al. 2011) and thus could be a signal of a slowdown in the bottom limb of the

MOC. Indeed, Kouketsu et al. (2011) found decreases in northward flowing water below 3500 m across 35°S in the Pacific and western Atlantic between the 1990s and 2000s in a data assimilation that includes the deep warming signals.

Here we estimate changes in the bottom, southern limb of the MOC globally using 32 repeated oceanographic sections (hereafter sections), with a total of 145 occupations between 1981 and 2011, by calculating the increase or decrease in volume below multiple deep potential temperature (θ) surfaces. The sections are grouped within and averaged over each measured deep ocean basin. We use the rates of change in volumes of these cold, dense waters to infer changes in the deep and bottom circulation. While the difference of a section occupied twice may still be subject to short-term variability, the calculation of rates, often over multiple occupations, together with the estimation of means from multiple sections within a basin, usually creates a statistically significant result. This technique allows more robust estimates of changes in the MOC than those derived from geostrophic transport estimates across a single transoceanic hydrographic section.

3.2 Data

The data used for this study are from an assembly of 32 full-depth, high-quality, ship-based hydrographic sections that have been occupied two or more times between 1981 and 2011 (Fig. 3.1). The data set is comprised of the publicly available conductivity-temperature-depth (CTD) instrument data on http://cchdo.ucsd.edu/ as of September 2011, collected either through the World Ocean Circulation Experiment (WOCE) hydrographic program or the Global Ship-based Hydrographic Investigations Program (GO-SHIP) program in support of the Climate Variability (CLIVAR) and carbon cycle science programs. Data along sections were collected at stations nominally spaced at 55 km. Each station includes a vertical profile of temperature, salinity, and pressure from the surface to a depth of 10–20 m from the bottom. Accuracy of temperature, salinity, and pressure are nominally 0.002°C, 0.002 PSS-78, and 3 dbar respectively (Joyce 1991). Most of the deep ocean basins are crossed by at least one section (Fig. 3.1). The time and number of occupations varies among sections, but the mean time difference between the first and last occupation for all sections considered here is 14.5 years with the mean first occupation occurring in 1991 and the mean last in 2006. For the three southernmost basins (Fig. 3.1), the mean time difference is 13.9 years with the mean first occupation in 1993 and the mean last in 2006. Prior to analysis, the data are screened so only data with good quality flags are used. In addition, only occupations deemed sufficiently close (in space) to prior occupations along a given section are used (see Purkey and Johnson 2010 for details).

A full description of the temporal and spatial distribution of the bulk of data used here can be found in Purkey and Johnson (2010). Four new sections and seven new occupations of previously used sections have become available since the publication of Purkey and Johnson (2010) and are added to the data set they used for this analysis. The new sections, identified by their WOCE designators, include: P09 running along 137°E between 10°N and 30°N with occupations in 1994 and 2010, S4P running along 67°S between 170°E and 70°W occupied in 1992 and 2011, SR01 running along 65°W between 57°S and 63°S occupied in 1993, 1994, 1996, and 1997, and I02/IR06 running roughly along 8°S between 94°E and 106°E and then diagonally between 9°S, 106°E to 24°S, 111°E occupied in 1995 and 2000 (Fig. 3.1). Additional occupations of existing sections previously used include: the 1983 occupations of A20 and A22, the 2005 occupation of A12, the 1992 and 2005 occupation of SR04, the 2008 occupation of

SR03, and the 2011 partial occupation of A16. All new sections are screened and gridded for use following Purkey and Johnson (2010).

3.3 Volumetric rate of change analysis

Along many sections, a visible rising or sinking of potential isotherms can be observed between occupations, especially in the Southern Ocean (e.g., Fig. 3.2). Except within temperature inversions, areas of sinking isotherms are correlated with areas of warming on isobars (and areas of rising with cooling). Similarly, the sinking of an isotherm within a basin implies a loss of water below that θ (Fig. 3.2), and the rising implies a gain. For example, both occupations of a meridional section across the Australian-Antarctic Basin reveal cold AABW cascading down the continental shelf into the deep ocean on the southern side of the basin (Fig. 3.2a). However, the coldest deep isotherms ($\theta \leq -0.2$°C) across this basin systematically fall with time between occupations, implying a volumetric loss of these deep and bottom waters. By $\theta = 0.2$°C the isotherms are centered around similar depths for both occupations, implying an increase with time in the volume of water within $-0.2 \leq \theta \leq 0.2$°C that compensates for the contraction of the coldest waters near the bottom, at least in this particular section.

To quantify the loss or gain of water as a function of θ, we first calculate the depth of the isotherms for each occupation along each section. We analyze 811 θ surfaces, referred to as the θ grid, ranging from -2.2°C to 32°C with a spacing of 0.01°C below 3°C and a spacing of 0.1°C above 3°C. For each occupation at each location along a section, the θ-pressure profile is converted to a θ-depth profile and linearly interpolated onto the θ grid. Any θ inversions starting from the bottom up are masked over; in other words, the depth of each θ is defined as the deepest depth at which that θ is found. This convention means that upper water column θ minimums (inversions) are not included in this analysis.

The sections are apportioned to the 33 deep basins they cross. The basin boundaries follow the bottom topography and are mostly isolated by at least the 3000 m isobath (Fig.1; Smith and Sandwell 1997). The basin boundaries are those used in Purkey and Johnson (2010) except that their Amundsen-Bellingshausen Basin (ABB) has been subdivided into the ABB and the Scotia Sea here (Fig. 3.1). Most of the major deep ocean basins are crossed by at least one repeat section (Fig. 3.1), with the exceptions of the Arabian Sea and Somali Basin, where no repeat sections are available owing to recent piracy-related safety concerns.

Along each section, within a given basin, the mean rate of change in height above the bottom ($\overline{\partial h / \partial t}$), its standard deviation ($\sigma_{\partial h/\partial t}$), and total degrees of freedom (DOF) are calculated for all values of the θ grid. The height (h) is the difference between the potential isotherm depth (d_i) and that of the sea floor (d_b; Smith and Sandwell 1997; Fig. 3.3a). The quantity $\partial h/\partial t$ is found from the slope of a least-squares linear fit of the isotherm heights to their dates of occupation (e.g., Fig 3b). The DOF are computed as the horizontal length of the section sampled for $\partial h/\partial t$ for a given isotherm divided by a horizontal decorrelation scale for deep ocean θ of 163 km estimated by Purkey and Johnson (2010). Sampled regions isolated by topography over a distance less than the decorrelation length scale and separated from adjacent sampled regions by distances more than the decorrelation length scale are assumed to be statistically independent and add one DOF.

Two screening criteria are applied to mask out regions with insufficient spatial or temporal coverage. First, if the time between the first and last occupation is less than 2.5 years, $\partial h/\partial t$ is discarded. Second, if the sum of the area covered by a given θ along a section is less than 111 km, $\overline{\partial h/\partial t}$ is not used. Isotherms sampled for less than 111 km are likely based on data from two or fewer CTD stations, making their mean depth unreliable. This criterion eliminates the coldest, deepest isotherms in many basins (such as the coldest AABW water cascading down over the Antarctic continental shelf and slope), but it ensures that we are looking at robust, basin-scale means, which are the focus of this paper.

The $\overline{\partial h/\partial t}$, $\sigma_{\partial h/\partial t}$, and DOF along all sections within a given basin are used to compute the basin-mean $\overline{\partial h/\partial t}$, $\overline{\partial h/\partial t}_{bsn}$, and its uncertainty for each θ value. If there is only one section crossing the basin, the $\overline{\partial h/\partial t}$ for that section is assumed to represent the whole basin. If there are multiple sections crossing a given basin, a length-weighted average is found using the horizontal length occupied by each θ on each section as its weight. The standard error is calculated by dividing the standard deviation by the square root of the DOF, and then a length-weighted average of the standard errors are found. The total DOF for the basin is the sum of the DOF associated with each θ for all sections within the basin. In addition to the basin variability, the 3 dbar and 0.002ºC measurement accuracy of the CTD pressure and temperature sensors translate to a 12 m uncertainty at most in isotherm depths for any given cruise. This instrumental uncertainty is neglected hereafter because it is very small compared to that arising from natural variability (e.g., Fig 2).

Finally, the $\overline{\partial h/\partial t}_{bsn}$ is scaled to a rate of change in volume (ΔV) within the basin using climatological data (Gouretski and Koltermann 2004; e.g., Fig 3c). The climatological data set has a half-degree horizontal resolution with 45 depths. At each location θ is calculated from salinity, temperature, and depth data. Each profile is interpolated onto a 20 m vertical grid using a piecewise cubic Hermite interpolation and linearly interpolated onto the θ grid following the same method described above. The climatological data are divided into the 33 basins. For each basin, the total surface area covered by each θ is calculated. The $\overline{\partial h / \partial t_{bsn}}$ and associated standard error for each basin and θ are converted to ΔV within that basin by multiplying by the corresponding climatological surface area. Two-sided 95% confidence intervals are estimated from Student's t-distribution using the standard errors and total DOF.

The result is a profile of ΔV versus θ with 95% confidence intervals for each of the 27 basins with data (e.g., Fig. 3.4). Negative values of ΔV indicate a contraction of water below the associated potential isotherm, zero indicates no change, and positive indicates net gain. When water is lost between successively warmer isotherms, the ΔV curves have a negative slope. Vertical portions of the curves indicate no additional loss of water between isotherms, but also no recovery. A positive slope indicates an increase in the amount of water between successively warmer isotherms. The error estimate reflects both the variability across sections and the number of data points. If a given θ is not well sampled, its associated error will be large. The surface area of each isotherm scales both its ΔV and the associated error. For example, the 95% confidence interval around the Weddell-Enderby Basin (WEB) ΔV curve (Fig. 3.4a) narrows with increasing depth (decreasing θ) since the total basin volume below a given isotherm decreases with decreasing temperature. In contrast, the $\overline{\partial h / \partial t_{bsn}}$ and associated error for the WEB does not (Fig. 3.5).

3.4 Southernmost basin changes

The ΔV profiles of the three southernmost basins (Fig. 3.1) all show a remarkably similar pattern (Fig. 3.4; orange curves). Each reveals a loss of volume, ranging from -1.6 to -3.6 Sv, within the coldest ~0.5°C of the water column and a recovery from the bottom water contraction within the θ classes of the Circumpolar Deep Water (CDW).

In the WEB (Fig. 3.1) of the South Atlantic Ocean, a contraction of bottom water is found for $\theta < -0.55$°C, with a maximum value of -3.6 (±2.0) Sv (Fig. 3.4a). This rate of change in volume is equivalent to a mean isotherm fall rate of ~15 m yr^{-1} (not shown). Within error bars, this maximum value of ΔV aligns with the -0.7°C boundary between WSBW and WSDW (Carmack and Foster 1975; Orsi et al. 1993) and is found roughly 1000–2000 m above the bottom of the basin. Above the WSBW, we find no significant gain or loss of WSDW for $-0.7 < \theta < 0$°C (Fig. 3.4a). The bottom water contraction is compensated higher in the water column by an increase in the volume of water with $0.25 < \theta < 0.5$°C. This water is found shallower than 1000 m, where a tongue of lower CDW rises to the south in the ACC as it enters the basin from the north. The ΔV curve for the basin suggests a southward surge of CDW into the region.

Is there a discernible regional pattern of AABW contraction within the WEB? The WEB ΔV curve contains data from three sections: The zonal section SR04 cutting across the Weddell Gyre at approximately 65°S, the meridional section A12 running along the Greenwich Meridian, and the meridional section I06 running along 30°E (Fig. 3.1). That all three sections show a negative $\partial h/\partial t$ for $\theta < 0$°C and overlap among their 95% confidence intervals indicates an overall consistency of vertical isotherm motions across the basin (Fig. 3.5). Error is reduced in the mean compared to the individual sections owing to the increase in DOF.

Bumps and wiggles in the mean curves have to be considered in the context of their associated uncertainties. Most sections in the southern basins exhibit a large contraction of water in their coldest temperature class, causing a negative bulge in the mean curve at that potential temperature. The location of the section determines this value and it does not necessarily represent the overall volume rate of change of the basin. The bulge at $\theta = -0.82$°C in the WEB (Figs. 4 and 5) is an example. This bulge is not outside the confidence limits of the rates given for the θs above and below (Fig. 3.4). Thus the θ of maximum volume loss in each basin effectively has uncertainties determined by the confidence intervals for ΔV around that θ. For example, above we assert $\theta = -0.55°C$ exhibits maximum volume loss within the WEB. But because the contraction rate at $\theta = -0.55°C$ is somewhere between 5.8 and 1.8 Sv, this is only an estimate of the isotherm – at 95% confidence the real value lies somewhere from $0.6 > \theta > -0.7°C$ (Fig. 3.4a).

The Australian-Antarctic Basin of the South Indian Ocean (Fig. 3.1), fed by both WSBW and Adelie Land Bottom Water (ALBW; Mantyla and Reid 1995), shows a loss of -2.2 (±1.1) Sv of water with $\theta < 0°C$ (Fig. 3.4b), equivalent to a mean isotherm fall rate of 14 m yr^{-1}. The mean ΔV curve does not show a full recovery from the bottom water contraction until $\theta = 2.5°C$, although the curve is not significantly different from zero for $\theta \geq 0.5°C$. These increasing volumes of warmer temperatures suggest a surge of upper CDW from the north is replacing the bottom water losses.

In the ABB of the South Pacific Ocean (Fig. 3.1), a maximum loss of -1.1 (±0.3) Sv of water colder than 0°C is found (Fig. 3.4c), equivalent to a mean fall rate of 13 m yr^{-1}, a pattern similar to that for the Australian-Antarctic Basin (Fig. 3.4b). Water colder than 0°C is within the temperature range of AABW produced in the Ross Sea. It is known as Ross Sea Bottom Water (RSBW), and previously characterized by salinities > 34.7 and $\theta < 0°C$ (Jacobs et al. 1970). The ABB exhibits a more diffuse recovery from the bottom water contraction than the WEB; in the former the ΔV curve increases slowly between 0 and 1.5°C. Water with $\theta \sim 1.5°C$ is upper CDW, found around 1000 m depth in the ABB. Our results suggest an influx of upper CDW from the north in the ABB.

3.5 Changes along the northward paths of AABW

AABW spreads north, primarily along four main DWBCs, out of the Southern Ocean (Fig. 3.1), filling the bottom-most reaches of most of the world's deep basins (Johnson 2008; Lumpkin and Speer 2007). The Southern Ocean retains a large reservoir of AABW (Fig. 3.6) as deep ridges restrict its northward transport, their sills limiting the density (and cold temperature) of water that continues north (Orsi et al. 1999; Johnson 2008). The temperature of outflowing waters should be warmed by the observed descent of isotherms in the southern basins, provided they fall at sills. The ΔV curves reveal a clear pattern of decreased AABW volume transport to the north along three of the four main DWBCs leaving the Southern Ocean (Fig. 3.4). In each case, the θ class below which the contraction is observed increases to the north due to mixing along the path and, presumably, isotherms sinking with time at the sills (Fig. 3.4).

In the West Atlantic, the basins directly to the north of the WEB along the DWBC of AABW show a volume loss within the AABW (Fig. 3.4a). Water as cold as $\theta = -0.6$°C leaves the WEB (Fig.6; Gouretski and Koltermann 2004) and flows into both the Scotia Sea and the Argentine Basin (Meredith et al. 2008) although extensive volumes of cold water within these basins do not start until around -0.2°C (Gouretski and Koltermann 2004). In the WEB a 10 m yr^{-1} isotherm descent rate is observed below -0.2°C. Along the north ridge of the WEB, the vertical θ gradient is about 0.1°C in 300 m, suggesting the outflowing water should have warmed by roughly 0.07°C over the past ~20 years. This hypothesis is supported by the ΔV curves in the Scotia Sea and Argentine Basin to the north.

The Scotia Sea exhibits at most a small and highly uncertain volume loss of -0.4 (±2.1) Sv below 0.2°C. The Scotia Sea is crossed by two meridional sections: A16 and S01. A16 shows a large ~30 m yr^{-1} descent of isotherms between -0.5 and 0.5°C, consistent with the isotherm descent observed in the WEB. However, S01, located farther to the west, shows a rising of isotherms but with an extremely large uncertainty. As a result, the mean (not shown) shows no significant volume loss or gain at any potential temperature. Although no statistically significant trend was found in our analysis, Meredith et al. (2008) reported a decrease in volume of water colder than 0°C in the Scotia Sea between 1995 and 2005 in the A16 data.

Cold water from both the Scotia Sea and directly from the WEB feed the Argentine Basin (Fig. 3.1; Meredith et al. 2008). A maximum bottom water contraction of -2.2 (±2.1) Sv of water below -0.2°C is observed there (Fig 4a, green curve) equivalent to an isotherm fall rate of ~15 m yr^{-1}, again consistent with observations in the WEB. The first isotherm to span the width of the basin fully is θ = -0.2°C. Between -0.2°C and the coldest sampled water, a small volume loss is observed (Fig. 3.4). Colder than -0.2°C, isotherms cascade downward on the south side of the basin, and thus only cover a small volume of water. These waters may be undersampled here. We do not quantify volume changes for θ < -0.4°C because there are either no data or insufficient data. A full recovery from the bottom water contraction appears to occur by ~ 2°, although for θ > -0.15°C the volume changes are no longer significantly different from zero (Fig. 3.4a). South of the equator, a strong deep thermocline for $1 < \theta < 2$°C denotes the vertical interface between the north flowing AABW and the south flowing NADW above (e.g., Johnson and Doney 2006). The ΔV pattern indicates that the AABW contraction may be compensated by an increase in NADW in the Argentine Basin.

Farther to the north, in the Brazil Basin (Fig. 3.1), we again find significant loss of the deepest, coldest northward flowing bottom waters. The coldest water to exit the Argentine Basin into the Brazil Basin is θ ~ 0.2°C, but again, the bottom of the basin is filled with warmer waters, around 0.3°C. Here, a loss of -0.6 (±0.3) Sv (or a mean isotherm fall rate of 9 m yr^{-1}) for waters colder than 0.3°C is observed in the deepest water. The contraction continues to a maximum loss of -0.8 (±0.3) Sv for waters below 0.86°C (Fig. 3.4a, purple curve) and does not fully recover until above 2°C, again near the upper extent of AABW influence (e.g., Johnson and Doney 2006).

In the west Indian Ocean DWBC (Fig. 3.1), bottom water flows out of the WEB into the Crozet Basin, followed by the Madagascar Basin, Somali Basin, and Arabian Sea (e.g., Mantyla and Reid 1995; Sloyan 2006). While this DWBC is fed by the same source water as the northward flowing western Atlantic DWBC, there are no statistically significant cold θ depth changes along this path outside of the WEB, possibly due to a lack of data (Fig. 3.1). Changes in this DWBC system are not discussed further here.

In the east Indian Ocean, water above 0.5°C flows north out of the Australian-Antarctic Basin into the South Australian Basin through the Australian-Antarctic Discordance (Fig. 3.1; e.g., Sloyan 2006). Colder than 0.5°C, a descent rate of -10 (±16) m yr^{-1} is observed in the Australian-Antarctic Basin, suggesting about a 0.1°C increase in the coldest bottom water leaving the Australian-Antarctic Basin, given the vertical temperature gradient near the basin's northern boundary. The South Australian Basin shows a slight loss of ~ -0.3 Sv of water colder than 0.7°C, but it is not significantly different from zero (Fig. 3.4b). Any possible contraction is recovered by 1.2°C and with a continued positive slope the basin shows a net gain in water by 1.7°C. The uncertainties for the ΔV curve in this basin are large, and none of these results are significant at the 95% confidence level.

The Wharton Basin (Fig. 3.1), however, does show a statistically significant loss of bottom water (Fig. 3.4b). About 4.4–5.8 Sv of water colder than 0.64°C flows out of the South Australian Basin into the Wharton Basin through a gap between the Broken and Naturaliste plateaus (Sloyan 2006). We find a small but statistically significant contraction of -0.1 (±0.05) Sv below this θ value in the Wharton Basin, which shows a maximum decrease of -0.75 (±0.4) Sv at 0.8°C, again corresponding to the coldest waters to span the whole basin. This bottom water contraction slowly recovers between 0.8 and 1.3°C. AABW-derived waters in the Wharton Basin cross the Mid-Indian Ridge into the Mid-Indian Basin (Warren and Johnson 2002), but we find no significant trend of cold bottom water volumes in the Mid-Indian Basin (not shown).

In the Pacific, water from both the Australian-Antarctic Basin and ABB feed the DWBC that flows northward through the Southwest Pacific Basin (Fig. 3.1; Whitworth et al. 1999). The coldest water to enter the Southwest Pacific Basin has $\theta \sim 0.4$°C, and there is a substantial volume in the basin below 0.6°C. The Australian-Antarctic Basin and ABB show an isotherm fall rate between 3 and 6 m yr^{-1} below 0.6°C. Subsequently, the Southwest Pacific Basin ΔV profile shows loss of -5 (±4.5) Sv of the coldest measured water at 0.54°C (Fig. 3.4c). Above the large bottom water loss, the isotherms between 0.57 and 0.62 all descend by ~12 m yr^{-1}, causing a continued significant contraction rate of ~2 Sv which is recovered by around 1°C.

The northward flow of bottom water continues into the Pacific Basin (Fig. 3.1) through the Samoan Passage with deep northward flow estimated at 10.6 (±1.7) Sv below $\theta = 1.1$°C and 4.8 (±0.3) Sv below 0.8°C (Roemmich et al. 1996). Here we find a statistically significant reduction of -3.4 (±1.4) Sv below 1.1°C and a small change of ~ -0.1 Sv below 0.8°C (Fig. 3.4c). Above 1.1°C there is a slight recovery, but the curve stays statistically significantly negative, with an isotherm decent of ~ 0.5 m yr^{-1} until 5°C.

3.6 Basin budgets

In steady state, maintenance of the vertical θ structure in abyssal basins can be modeled as a balance among the lateral inflow of cold AABW, geothermal heating at the sea floor, vertical mixing with warmer water above, and vertical advection (upwelling). However, the ΔV curves imply that heat and volume budgets below deep, cold θ surfaces are not in steady state in many deep basins. We diagnose these departures from steady state with volume and heat budgets for the Pacific Basin below $\theta = 1$ °C and the Brazil Basin below 0.8 °C and determine how inflowing AABW transport or θ, geothermal heating, or vertical mixing would have to change in order to account for the observed volume and heat changes. We chose these examples because accurate temperature and volume transport estimates are available for these basins below isotherms at which we find significant ΔVs.

Observed ΔVs imply ~15% imbalances in the deep basin volume budgets. Morris et al. (2001) estimate the net lateral inflow of water (through several channels) of $\theta < 0.8$ °C into the Brazil Basin at 3.70 Sv from current meter data, dominated by a 4.02 Sv inflow through the Vema Channel. Steady-state volume balance would require upwelling at a rate of 3.70 Sv through $\theta = 0.8$ °C. However, the observed ΔV of 0.56 Sv at $\theta = 0.80$ °C (Fig. 3.4a), requires a 14% reduction of inflow through the Vema Channel to 3.46 Sv or a 15% increase in upwelling to 4.26 Sv. Similarly, Roemmich et al. (1996) found 11.22 Sv of inflow for $\theta < 1$ °C into the Pacific Basin through the Samoa Passage and environs. With no lateral outflow of water for $\theta < 1$ °C, upwelling through this surface must also be 11.22 Sv in steady state. The observed ΔV of 1.98 Sv at $\theta = 1$ °C (Fig. 3.4c), requires a 18% reduction of inflow or increase of upwelling.

The extent to which the observed ΔV changes perturb the steady-state heat budget can be diagnosed following Morris et al. (2001). By assuming steady state conservation of volume and heat below cold, deep potential isotherms in the Brazil Basin, Morris et al. (2001) estimated vertical diffusion coefficients. We start with a slightly modified steady-state equation (see Table 3.1) that balances lateral transports and upwelling of heat, vertical mixing of heat, and geothermal heating at the sea floor.

An imbalance term, the rate of change in heat storage (Table 3.1, rightmost column), is calculated from the ΔV curves (Fig. 3.4) below select isotherms (θ_{top}). Since the ΔV curves are cumulative sums over θ intervals they are first differentiated with respect to θ, multiplied by $\theta_{top} - \theta$ (since water must be heated to θ_{top} before exiting the control volume), and then integrated from the bottom up to θ_{top}. In both the Pacific and Brazil basins the time-dependent heat storage terms are not negligible compared to the dominant terms in the steady-state budget. In the Pacific Basin, the heat storage term is ~6% of the advective or mixing terms and comparable to the geothermal term (Table 3.1). In the Brazil Basin, the heat storage term is about 8% of the advective or mixing terms and about four times higher than the geothermal term (Table 3.1).

We diagnose the changes in water volume transports through deep passages (U_i), transport-weighted potential temperatures of U_i (θ_i), κ, θ_z, or Q (Table 3.1) required to account for the observed changes in heat storage below θ_{top} in the Brazil and Pacific basins. These estimates all assume a new steady-state balance has been reached. First, Q would have to almost double in the Pacific Basin and more than quintuple in the Brazil Basin to account for the observed changes in heat storage. We know of no evidence or plausible reason that such a change in geothermal heating has occurred.

In both basin budgets, the heat storage term is about 6 to 8% of the advective and mixing terms. Hence, for the Pacific Basin, U_i at the Samoa Passage would have to decrease by 0.65 Sv below 1 °C , from 11.22 to 10.57 Sv, to account for the change in heat storage. For the Brazil Basin, U_i in the Vema Channel would have to decrease by 0.33 Sv below 0.8 °C, from 4.02 to

3.69 Sv. Both changes are less than those required to balance volume. Alternatively, θ_i in the Samoa Passage would have to increase by 0.013 °C, from 0.77 to 0.78 °C, a plausibly small amount. In the Brazil Basin, θ_i through the Vema Channel would have to warm by 0.06 °C, from 0.03 to 0.09 °C, broadly consistent with an observed 0.03 °C decade^{-1} increase in the coldest θ in that channel over recent decades (Zenk and Morozov 2007).

Changes in κ or θ_z required to account for the observed changes in heat storage (Table 3.1) are equally small. For the Pacific Basin κ would have to increase from 5.63 to 5.98 × 10^{-4} m^2 s^{-1} or θ_z from 0.28 to 0.30 × 10^{-3} °C m^{-1}. In the Brazil Basin, κ would have to increase from 4.34 to 4.70 × 10^{-4} m^2 s^{-1} or θ_z from 1.41 to 1.53 × 10^{-3} °C m^{-1} to account for the change in heat storage. Such undetectably small changes cannot be ruled out. However, θ_z increases would be unexpected, since warming bottom waters should decrease θ_z.

3.7 Discussion

Here we have shown a large decrease of the volume of AABW over time in the Southern Ocean, consistent with a slowdown of the bottom, southern limb of the MOC. Classically defined AABW ($\theta \leq 0$°C) is largely limited to the Australian-Antarctic Basin, ABB, WEB, Argentine Basin, Scotia Sea, and Agulhas-Mozambique Basin. In these basins, $\theta = 0$°C has fallen at a rate of -13.2 (±6.7), -11.4 (±2.9), -8.1 (±4.5), -9.5 (±9.6), -8.6 (±40.3), and -6.4 (±12.1) m yr^{-1}, respectively. The area-scaled sum of these rates yields an estimated contraction rate of -8.2 (±2.6) Sv for water colder than 0°C (Table 3.2). To the north, along the three best-sampled paths for exporting AABW-derived bottom waters from the Southern Ocean in the lower limb of the MOC, we find a smaller contraction of the volume of the coldest, deepest water. These volume losses suggest a global slowdown of the bottom limb of the MOC.

Ventilation timescales along the bottom limb of the MOC from the Southern Ocean to the abyssal north Pacific are of order 1000 years (e.g., DeVries and Primeau 2011), much longer than the timescales of this study. However, previous studies have demonstrated that a reduction of AABW formation around Antarctica can be communicated through the abyss in just decades by planetary waves (e.g., Masuda et al. 2010). Budget calculations in two well-measured deep basins suggest that the observed bottom water temperature trends could be owing to a change in the transport of bottom water entering the basin.

These results hinge on the assumption that the data analyzed are representative of the deep sampled basins both spatially and temporally over the past 30 years. The spatial coverage of the data appears generally good, with most basins analyzed having repeat sections crossing them at roughly even distances, especially in the Southern Ocean (Figs. 1 and 6). This assumption of spatial representativeness can be checked by comparing the isotherm height rates of change ($\partial h/\partial t$) [Eq. (1)] along all sections within basins with multiple crossings. For example, in the WEB, the portions of three sections crossing that basin all show a similar pattern and amplitude in their $\partial h/\partial t$ curves (Fig. 3.5). On average, isotherms within the WSBW have a descent rate of -22.5 (±21.6) and -11.5 (±13.4) m yr^{-1} along A12 and SR04, respectively (Fig. 3.5). Within the WSDW, A12, SR04, and I06 exhibit average isotherm descent rates of -3.8 (±7.1), -9.4 (±4.8), and -16.5 (±12.9) m yr^{-1}, respectively (Fig. 3.5). Given the location of the sections (Figs. 1 and 6) and their relatively uniform patterns of isotherm descents (Fig. 3.5), it seems unlikely that the volume of the coldest waters has remained constant and instead has shifted around this basin due to changes in gyre strength or location, as suggested previously (Fahrbach et al. 2011). Furthermore, when the ΔV curves for this basin and many others are calculated with different subsamples of the sections crossing those basins, there usually are only small variations in the curves.

Second, here we assume that the temporal data coverage is sufficient to capture any trend. For sections with more than two occupations, this assumption usually appears valid (e.g., Fig. 3.2b). Although looking for geostrophic transport trends in multiple occupations of a single section can be misleading because variations in a few stations can dominate such a calculation (e.g., Cunningham et al. 2007), here all the station data from multiple occupations of multiple sections are being averaged over very large areas. This procedure should reduce smaller scale temporal or spatial noise. Furthermore, our error analysis quantifies the variability within our data set. In most of the basins presented here, results are statistically significantly different from zero, which suggests that these results are more robust than previous studies of multiple occupations of a single section.

A slowdown of the AABW production rate is consistent with the freshening of shelf waters in AABW formation regions in the Ross and Weddell seas in recent decades (Aoki et al. 2005; Jacobs and Giulivi 2010; Hellmer et al. 2011). The surface freshening increases the stability of the water column, making it more difficult for surface waters to sink, possibly causing a slowing of the bottom limb of the MOC (Stouffer et al. 2007). In the Ross Sea, the shelf water and RSBW have freshened by ~0.03 and ~0.01 decade^{-1}, respectively, between 1958 and 2008 (Jacobs and Giulivi 2010), most likely caused by recent glacial melt along the Amundsen and Bellingshausen seas freshening the westward flowing coastal current (Rignot et al. 2008; Jacobs and Giulivi 2010). Along the coast at 140ºE and within the central Australian-Antarctic Basin, AABW has also warmed and freshened (Aoki et al. 2005; Johnson et al. 2008a), again pointing toward a freshening of the shelf water end member of either, or both, RSBW and ALBW. In the

Weddell Sea, the northwestern shelf water has freshened by 0.09 between 1989 and 2006, owing to increasing glacial melt water input, changes in sea ice extent, and higher precipitation (Hellmer et al. 2011).

The recent positive trend in the Southern Annular Mode (SAM) has been connected directly and indirectly to AABW formation rates. Due to past ozone depletion, the summer time SAM index has been trending positive since the 1950s and is predicted to continue positive due to global warming (Thompson et al. 2011). A positive trend in the SAM is associated with stronger and more poleward westerly winds over the Southern Ocean (Gillett and Thompson 2003; Arblaster and Meehl 2006; Thompson et al. 2011) and southward migration of the ACC with associated warming (Gille 2008). Even though the SAM trend is only significant during the summer months and AABW is formed during winter, SAM changes may contribute to increased glacial melt, a southward shift in the ACC, warmer temperatures, and increased precipitation over the Southern Ocean. Given the timescales involved with these phenomena, summer SAM changes could be linked to the observed slowdown of AABW. Further, models have shown the strengthening and the southward migration of westerlies is tied to a net increased of inflow of NADW into the South Atlantic (e.g., Oke and England 2004) and an increase in the northward Ekman transport, which leads to a strengthening of CDW upwelling (e.g., Russell et al. 2006), consistent with our results. Finally, models have also demonstrated that SAM variability can lead to changes in ice formation and melting connected directly to bottom water formation (Gordon et al. 2007; Klinger and Cruz 2009; Kirkman and Bitz 2011).

In addition to a slowdown in AABW formation rates, shifts in other physical processes could also have contributed to the observed AABW volume loss. First, geothermal heating could have increased and warmed AABW. We have no reason to believe geothermal heating in the

Southern Ocean has increased dramatically in the past several decades. In more northerly basins, Q would have to increase unrealistically in order to account for observed heat storage changes (Section 6).

Second, one might argue that the same amount of AABW is being produced, but is now warmer and fresher, hence lighter. As noted above, shelf water components of AABW have freshened in recent decades, linked to freshening of ALBW and RSBW (Aoki et al. 2005; Jacobs and Giulivi 2010). In addition, the shelf water entrains adjacent waters as it descends the continental slope to form AABW. Therefore, recently reported warming of adjacent water masses such as CDW (e.g., Böning et al. 2008) or changes in entrainment rates could also affect AABW properties. Indeed, a southward surge of CDW to replace the reduction in AABW, suggested by our calculations, could affect AABW properties. However, if the AABW changes were in its properties and not its formation rate, the ΔV curves in the southernmost basins would exhibit a sharp negative spike centered around the change in θ of the AABW, which is not observed (Fig. 3.4).

Third, a small change in mixing rates could produce a basin-wide deep warming (e.g., Section 6). However, we know of no reason to believe mixing rates have changed over recent decades. Of course, if AABW formation rates have slowed, AABW residence times within these basins could increase, at least while the system adjusts, allowing more time for AABW to mix with overlying waters even if the mixing coefficient does not change. In this respect, the rates of AABW volume changes estimated here can be thought of as an upper bound on changes in formation rates, because mixing may account for some of the changes during any adjustment period.

Here we have suggested that AABW formation has decreased by as much as -8.2 (±2.6) Sv for the period 1993–2006 relative to some previous time period, without addressing the absolute values of AABW formation or when that previous time period might be. How much AABW is being produced presently and how much was produced in the past? While roughly 20 Sv of deep water of Southern Ocean origin has been exported northward in the bottom limb of the MOC in recent decades according to CFC inventories (Orsi et al. 2002) and inverse models (Ganachaud and Wunsch 2000; Sloyan and Rintoul 2001; Lumpkin and Speer 2007), a more relevant formation rate estimate for the classic definition of AABW (roughly $\theta < 0°C$) is 8.1–9.4 Sv from a CFC inventory (Orsi et al. 1999). This inventory-based estimate is centered around 1980, and gives a rough residence time of 120 years using a climatological volume for $\theta < 0°C$ (although the concept of a reference time becomes complex when both the ventilation rate and reservoir volume are changing). If the 8.1–9.4 Sv AABW production rate is representative of earlier decades, our results would seem to imply that AABW production rates have slowed to near zero during the period 1993–2006. Since measurements show AABW is still being produced during these times (e.g., Gordon et al. 2001; Whitworth and Orsi 2006; Williams et al. 2008) this conclusion seems unlikely.

It may be more reasonable to suspect that AABW production rates were already lower around 1980 than in previous decades, so that earlier pure AABW formation could have as much as double the CFC inventory estimate, as supported by the following two arguments. First, a similar NADW formation rate estimate (LeBel et al. 2008) is twice that for pure AABW, and about equal for the total contribution of Southern Hemisphere waters to the bottom limb of the MOC, but these southern bottom waters fill about 1.7 times more of the ocean volume than NADW (Johnson 2008), suggesting that over the past millennia or so AABW formation rates may have been on average larger than NADW formation rates. Second, as discussed above, the SAM index has been rising at least since the 1950s, and may be associated with a reduction in AABW production rates. Therefore, AABW production rates may have started declining from previous larger values as early as the 1950s.

Acknowledgments. We thank all those who participated in the collection of the WOCE and GO-SHIP data used here. Arnold Gordon made some useful suggestions regarding AABW kinematics. The comments from three anonymous reviewers greatly improved the manuscript. The findings and conclusions in this article are those of the authors and do not necessarily reflect the views of the National Oceanic and Atmospheric Administration (NOAA). This work was supported by the NOAA Climate Program Office, NOAA Research, and NASA Headquarters under the NASA Earth and Space Fellowship Program - Grant NNX11AL89H.

REFERENCES

Aoki, S., S. R. Rintoul, S. Ushio, S. Watanabe, and N. L. Bindoff, 2005: Freshening of the Adélie Land Bottom Water near 140°E. *Geophys. Res. Lett.,* **32**, L23601, doi:10.1029/2005GL024246.

Arblaster, J. M., and G. A. Meehl, 2006: Contributions of external forcings to Southern Annular Mode trends. *J. Climate*, **19**, 2896–2905.

Boe, J., A. Hall, and X. Qu, 2009: Deep ocean heat uptake as a major source of spread in transient climate change simulations. *Geophys. Res. Lett.*, **36**, L22701, doi:10.1029/2009GL040845.

Böning, C. W., A. Dispert, M. Visbeck, S. R. Rintoul, and F. U. Schwarzkopf, 2008: The response of the Antarctic Circumpolar Current to recent climate change. *Nature Geosci,.* **1**, 864–869.

Bryden, H. L., H. R. Longworth, and S. A. Cunningham, 2005: Slowing of the Atlantic meridional overturning circulation at 25°N. *Nature*, **438**, 655–657, doi:10.1038/nature04385.

Carmack, E. C., and T. D Foster, 1975: On the flow of water out of the Weddell Sea, *Deep Sea Res.*, **22**, 711–724.

Church, J. A., and Coauthors, 2011: Revisiting the Earth's sea-level and energy budgets from 1961 to 2008. *Geophys. Res. Lett.*, **38**, L18601, doi:10.1029/2011GL048794.

Clark, P., N. G. Pisias, T. F. Stocker, and A. J. Weaver, 2002: The role of the thermohaline circulation in abrupt climate change. *Nature*, **415**, 863–869.

Coles, V. J., M. S. McCartney, D. B. Olson, and W. M. Smethie Jr., 1996: Changes in Antarctic Bottom Water properties in the western South Atlantic in the late 1980s. *J. Geophys. Res.*, **101**, 8957–8970.

Cunningham, S. A., and Coauthors, 2007: Temporal variability of the Atlantic Meridional Overturning Circulation at 26.5°C. *Science*, **317**, 935–938.

DeVries, T., and F. Primeau, 2011: Dynamically and observationally constrained estimates of water-mass distributions and ages in the global ocean. *J. Phys. Oceanogr.*, **41**, 2381–2401, doi:10.1175/JPO-D-10-05011.1

Fahrbach, E., M. Hoppema, G. Rohardt, M. Schroder, and A. Wisotzki, 2004: Decadal-scale variations of water mass properties in the deep Weddell Sea. *Ocean Dynamics*, **54**, 77–91.

Fahrbach E., M. Hoppema, G. Rohardt, O. Boebel, O. Klatt, and A. Wisotzki, 2011: Warming of deep and abyssal water masses along the Greenwich meridian on decadal time scales: The Weddell gyre as a beat buffer. *Deep-Sea Res. II,* **58**, 2508–2523, doi:10.1016/j.dsr2.2011.06.007.

Foster, T. D., and Carmack, E. C., 1976: Frontal zone mixing and Antarctic Bottom Water formation in the southern Weddell Sea. *Deep-Sea Res.*, **23**, 301–317.

Frajka-Williams, E., S. A. Cunningham, H. Bryden, and B. A. King, 2011: Variability of Antarctic Bottom Water at 24.5°N in the Atlantic. *J. Geophys. Res.*, **116**, C11026, doi:10.1029/2011JC007168.

Fukamachi, Y., S. R. Rintoul, J. A. Church, S. Aoki, S. Sokolov, M. A. Rosenberg, and M. Wakatsuchi, 2010: Strong export of Antarctic Bottom Water east of the Kerguelen plateu, *Nature Geosci.*, **3,** 327–331, doi:10.1038/NGE0842.

Fukasawa, M., H. Freeland, R. Perkin, T. Watanabe, H. Uchida, and A. Nishima, 2004: Bottom water warming in the North Pacific Ocean. *Nature*, **427**, 825–827.

Ganachaud, A., and C. Wunsch, 2000: Improved estimates of global ocean circulation, heat transport and mixing from hydrographic data. *Nature*, **408**, 453–457, doi:10.1038/35044048.

Gille, S. T., 2002: Warming of the Southern Ocean since the 1950s. *Science*, **295**, 1275–1277.

Gille, S. T., 2008: Decadal-scale temperature trends in the Southern Hemisphere ocean. *J. Climate*, **21**, 4749–4765.

Gillett, N. P., and D. W. J. Thompson, 2003: Simulation of recent Southern Hemisphere climate change. *Science*, **302**, 273–275.

Gordon, A. L., M. Visbeck, and B. Huber, 2001: Export of Weddell Sea Deep and Bottom Water. *J. Geophys. Res.*, **106**, 9005–9017, doi:10.1029/2000JC000281.

Gordon, A. L., M. Visbeck, and J. C. Comiso, 2007: A possible link between the Weddell Polynya and the Southern Annual Mode. *J. Climate*, **20**, 2558–2571.

Gouretski, V. V., and K. P. Koltermann, 2004: *WOCE Global Hydrographic Climatology.* Berichte des bundesamtes für seeshifffahrt und hydrographie, 35, pp. 52+2 CD-ROMs.

Hellmer, H., O. Huhn, D. Gomis, and R. Timmermann, 2011: On the freshening of the northwestern Weddell Sea continental shelf. *Ocean Sci.*, **7**, 305–316, doi:10.5194/os-7-305-2011.

Hofmann, M., and M. A. Morales Maqueda, 2009: Geothermal heat flux and its influence on the oceanic abyssal circulation and radiocarbon distribution, *Geophys. Res. Lett.,* **36**, L03603, doi:10.1029/2008GL036078.

Jacobs, S. S., and J. C. Comiso, 1997: Climate variability in the Amundsen and Bellingshausen seas. *J. Climate*, **10**, 697–709.

Jacobs, S. S., and C. F. Giulivi, 2010: Large multi-decadal salinity trends near the Pacific-Antarctic Continental Margin. *J. Climate***,** **23**, 4508–4524, doi:10.1175/2010JCLI3284.1.

Jacobs, S., A. F. Amos, and P. M. Bruchhausen, 1970: Ross Sea oceanography and Antarctic Bottom Water formation. *Deep-Sea Res.***,** **17**, 935–962.

Johnson, G. C., 2008: Quantifying Antarctic Bottom Water and North Atlantic Deep Water volumes. *J. Geophys. Res*., **113**, C05027, doi:10.1029/2007JC004477.

Johnson, G. C., and S. C. Doney, 2006: Recent western South Atlantic bottom water warming. *Geophys. Res. Lett*., **33**, L14614, doi:10.1029/2006GL026769.

Johnson, G. C., S. Mecking, B. M. Sloyan, and S. E. Wijffels, 2007: Recent bottom water warming in the Pacific Ocean. *J. Climate*, **20**, 5365–5375.

Johnson, G. C., S. G. Purkey, and J. L. Bullister, 2008a: Warming and freshening in the abyssal southeastern Indian Ocean. *J. Climate*, **21**, 5353–5365.

Johnson, G. C., S. G. Purkey, and J. M Toole, 2008b: Reduced Antarctic meridional overturning circulation reaches the North Atlantic Ocean. *Geophys. Res. Lett.,* **35**, L22601, doi:10.1029/2008GL035619.

Joyce, T. M., 1991: Introduction to the collection of expert reports compiled for the WHP Program. WOCE Hydrographic operations and methods. WOCE Operations Manual. WHP Office Report WHPO-91-1, WOCE Report 68/91.

Kanzow, T., and Coauthors, 2007: Observed flow compensation associated with the MOC at 26.5°N in the Atlantic. *Science*, **317** (5840), 938–941.

Kawano, T., M. Fukawasa, S. Kouketsu, H. Uchida, T. Doi, I. Kaneko, M. Aoyama, and W. Schneider, 2006: Bottom water warming along the pathways of lower circumpolar deep water in the Pacific Ocean. *Geophys. Res. Lett*., **33**, L23613, doi:10.1029/2006GL027933.

Kawano, T., T. Doi, H. Uchida, S. Kouketsu, M. Fukasawa, Y. Kawai, and K. Katsumata, 2010: Heat content change in the Pacific Ocean between the 1990s and 2000s. *Deep-Sea Res. II,* **57**, 1141–1151, doi:10.1016/j.dsr2.2009.12.003.

Kirkman, C. H., IV, and C. M. Bitz, 2011: The effect of the sea ice freshwater flux on Southern Ocean Temperatures in CCSM3: Deep-ocean warming and delayed surface warming, *J. Climate*, **24**, 2224–2237, doi:10.1175/2010JCLI3625.1.

Klinger, B. A., and C. Cruz, 2009: Decadal response of global circulation to Southern Ocean zonal wind stress perturbation. *J. Phys. Oceanogr.*, **39**, 1888–1904. doi:10.1175/2009JPO4070.1.

Kouketsu, S., M. Fukasawa, I. Kaneko, T. Kawano, H. Uchida, T. Doi, M. Aoyama, and K. Murakami, 2009: Changes in water properties and transports along 24°N in the North Pacific between 1985 and 2005. *J. Geophys. Res.*, **114**, C01008, doi:10.1029/2008JC004778.

Kouketsu, S., and Coauthors, 2011: Deep ocean heat content changes estimated from observation and reanalysis product and their influence on sea level change. *J. Geophys. Res.*, **116**, C03012, doi:10.1029/2010JC006464.

LeBel, D. A., and Coauthors, 2008: The formation rate of North Atlantic Deep Water and Eighteen Degree Water calculated from CFC-11 inventories observed during WOCE. *Deep-Sea Res. I,* **55**, 891–910.

Levitus, S., J. Antonov, and T. Boyer, 2005: Warming of the world ocean, 1955–2003. *Geophys. Res. Lett.,* **32**, L02604, doi:10.1029.2004GL021592.

Lumpkin, R., and K. Speer, 2007, Global ocean meridional overturning. *J. Phys. Oceanogr.,* **37**, 2550–2562.

Lynch-Stieglitz, J., and Coauthors, 2007: Atlantic meridional overturning circulation during the last glacial maximum. *Science,* **316**, 66–69, doi:10.1126/science.1137127.

Mantyla, A., and J. Reid, 1995: On the origins of deep and bottom waters of the Indian Ocean. *J. Geophys. Res.,* **100***,* doi:10.1029/94JC02564.

Masuda, S., and Coauthors, 2010: Simulated rapid warming of abyssal North Pacific water. *Science*, **329**, 319–322, doi:10.1126/science.1188703.

Meehl, G. A., and Coauthors, 2006: Climate change projections for the Twenty-First Century and climate change commitment in the CCSM3. *J. Climate*, **19**, 2597–2616. doi:10.1175/JCLI3746.1.

Meehl, G. A., J. M. Arblaster, J. T. Fasullo, A. Hu, and K. E. Trenberth, 2011: Model-based evidence of deep-ocean heat uptake during surface-temperature hiatus periods. *Nature Climate Change*, **1**, 360–364, doi:10.1038/NCLIMATE1229.

Meredith, M. P., A. C. Naveira Garabato, A. L. Gordon, and G. C. Johnson, 2008: Evolution of the deep and bottom water of the Scotia Sea, Southern Ocean, during 1995–2005. *J. Climate*, **21**, 3327–3343.

Morris, M., M. M. Hall, L. C. St. Laurent, and N. G. Hogg, 2001: Abyssal mixing in the Brazil Basin. *J. Phys. Oceanogr.*, **31**, 3331–3348.

Oke, R. R., and M. H. England, 2004: Oceanic response to changes in the latitude of the Southern Hemisphere subpolar westerly winds. *J. Climate*, **17**, 1040–1054.

Orsi, A. H., W. D. Nowlin Jr., and T. Whitworth III, 1993: On the circulation and stratification of the Weddell Gyre. *Deep-Sea Res. I*, **40**, 169–203.

Orsi, A. H., T. Whitworth III, and W. D. Nowlin Jr., 1995: On the meridional extent and fronts of the Antarctic Circumpolar Current. *Deep-Sea Res. I*, **42**, 641–673.

Orsi, A. H., G. C. Johnson, and J. L. Bullister, 1999: Circulation, mixing and production of Antarctic Bottom Water. *Prog. Oceanogr.*, **43**, 55–109.

Orsi, A. H., W. M. Smethie Jr., and J. L. Bullister, 2002: On the total input of Antarctic Waters to the deep ocean: A preliminary estimate from chlorofluorocarbon measurements. *Geophys. Res. Lett.*, **107**, doi:10.1029/2001JC000976.

Purkey, S. G., and G. C. Johnson, 2010, Warming of global abyssal and deep Southern Ocean waters between the 1990s and 2000s: Contributions to global heat and sea level rise budgets. *J. Climate*, **23**, 6336–6351. doi:10.1175/2010JCLI3682.1.

Rignot, E., J. L. Bamber, M. R. van Den Broeke, C. Davis, Y. Li, W. Jan Van De Berg, and E. van Meijgaard, 2008: Recent Antarctic ice mass loss from radar interferometry and regional climate modeling. *Nature Geoscience*, **1,** 106–110, doi:10.1038/ngeo102.

Rintoul, S. R., 2007: Rapid freshening of Antarctic Bottom Water formed in the Indian and Pacific oceans. *Geophys. Res. Lett.*, **34**, L06606, doi:10.1029/2006GL028550.

Robertson R., M. Visbeck, A. L. Gordon, and E. Fahrbach, 2002: Long-term temperature trends in the deep waters of the Weddell Sea. *Deep-Sea Res. II*, **49**, 4791–4806.

Roemmich, D., S. Hautala, and D. Rudnick, 1996: Northward abyssal transport through the Samoan passage and adjacent regions. *J. Geophy Res.,* **101**, 14 039–14 055.

Russell, J. L., D. W. Dixon, A. Gnanadesikan, R. J. Stouffer, and J. R. Toggweiler, 2006: The Southern Hemisphere Westerlies in a warming world: Propping open the door to the deep ocean. *J. Climate*, **19**, 6382–6390.

Sigman, D. M., and E. A. Boyle, 2000: Glacial/interglacial variations in atmospheric carbon dioxide. *Nature*, **407**, 859–869.

Sloyan, B. M., 2006: Antarctic bottom and lower circumpolar deep water circulation in the eastern Indian Ocean. *J. Geophy. Res.*, **111**, C02006, doi:10.1029/2005JC003011.

Sloyan, B. M., and S. R. Rintoul, 2001: The Southern Ocean limb of the global deep overturning circulation. *J. Phys. Oceanogr.*, **31**, 143–173, doi:10.1175/1520-0485(2001)031<0143:TSOLOT>2.0.CO;2.

Smith, W. H. F., and D. R. Sandwell, 1997: Global seafloor topography from satellite altimetry and ship depth sounding. *Science*, **277**, 1956–1962.

Solomon, S., D. Qin, M. Manning, Z. Chen, M. Marquis, K. B. Averyt, M. Tignor, and H. L. Miller, Eds., 2007: Climate Change 2007: The Physical Basis. Contribution of Working Group I to the Fourth Assessment Report of the Intergovernmental Panel on Climate Change**,** Cambridge University Press, Cambridge, United Kingdom and New York, NY, USA.

Stouffer, R. J., D. Seidov, and B. J. Haupt, 2007: Climate response to external sources of freshwater: North Atlantic vs. the Southern Ocean. *J. Climate*, **20**, 436–448.

Thompson, D. W. J., S. Solomon, P. J. Kushner, M. H. England, K. M. Grise, and D. J. Karoly, 2011: Signatures of the Antarctic ozone hole in Southern Hemisphere surface climates change. *Nature Geoscience*, **4**, 741–749, doi:10.1038/NGEO1296.

Warren, B. A., and G. C. Johnson, 2002: The overflows across the Ninetyeast Ridge, *Deep-Sea Res. II*, **49,** 1423–1439*,* doi:10.1016/S0967-0645(01)00156-4.

Whitworth, T., III, and A. H. Orsi, 2006: Antarctic Bottom Water production and export by tides in the Ross Sea. *Geophys. Res. Lett.*, **33**, L12609, doi:10.1029/2006GL026357.

Whitworth, T., III, W. D. Nowlin, R. D. Pillsbury, M. I. Moore, and R. F. Weiss, 1991: Observations of the Antarctic Circumpolar Current and deep western boundary current in the southwestern Atlantic. *J. Geophys. Res.*, **96**, 15 105–15 118.

Whitworth, T., III, B. A. Warren, W. D. Nowlin, Jr., S. B. Rutz, R. D. Pillsbury, and M. I. Moore, 1999: On the deep western-boundary current in the Southwest Pacific Basin. *Prog.*

Oceanogr., **43**, 1–54.

Williams, G. D., N. L. Bindoff, S. J. Marsland, and S. R. Rintoul, 2008: Formation and export of dense shelf water from the Adélie Depression, East Antarctica. *J. Geophys. Res.*, **113**, C04039, doi:10.1029/2007JC004346.

Willis, J. K., D. P. Chambers, and R. S. Nerem, 2008: Assessing the globally averaged sea level budget on seasonal to interannual timescales. *J. Geophys. Res.,***113**, C06015, doi:10.1029/2007JC004517.

Zenk, W., and E. Morozov, 2007: Decadal warming of the coldest Antarctic Bottom Water flow through the Vema Channel. *Geophys. Res. Lett.*, **34**, L14607, doi:10.1029/2007GJ030340.

Basin, θ_{top}	Steady State			$\sum_{\theta}^{\theta_{top}} \left(\theta_{top} - \theta\right) \frac{\partial \Delta V}{\partial \theta}$
	$\sum_i U_i \theta_i + W\theta_{top}$	$\kappa\theta_z \times SA$	$\frac{Q \times SA}{\rho C_p}$	
Pacific Basin, 1 °C	-2.57	2.38	0.19	-0.15
Brazil Basin, 0.8 °C	-3.11	3.05	0.06	-0.25

TABLE 3.1. Heat budget terms (in Sv °C) compared to the observed imbalances for two deep basins. From left to right, the advective term is the sum of all cold water volume transports (U_i) through passages i into or out of the basin each with transport-weighted potential temperatures (θ_i) below a top bounding potential isotherm (θ_{top}). Upwelling transport through that top surface (W) is derived assuming volume conservation. Values for U_i and θ_i are from Morris et al. (2001) in the Brazil Basin and Roemmich et al. (1996) in the Pacific Basin. The vertical diffusion term at θ_{top} is the product of the vertical diffusivity coefficient (κ), the vertical temperature gradient (θ_z), and surface area (SA) and is estimated from the residual of the other two steady-state terms. For the geothermal heating term, $Q = 0.05$ W m^{-2}, an average deep ocean value (Hofmann and Morales Maqueda 2009), is applied over SA, appropriately scaled by density (ρ) and heat capacity (C_p). Climatological maps (Gouretski and Koltermann 2004) are used to estimate θ_z, SA, ρ, and C_p for each basin. The imbalance term (rightmost column) is determined by summing the product of $\partial\Delta V/\partial\theta$ and $\theta_{top} - \theta$ from the coldest waters in the basin to θ_{top} (see text for further explanation).

Basin	Volume Change [Sv]
Weddell-Enderby	-2.85 (±1.59)
Australian-Antarctic	-2.24 (±1.14)
Amundsen-Bellingshausen	-1.09 (±0.28)
Argentine	-1.67 (±1.70)
Scotia Sea	-0.23 (±1.10)
Agulhas-Mozambique	-0.16 (±0.33)
Sum	-8.2 (±2.6)

TABLE 3.2. Rate of volume change below $\theta = 0°\mathrm{C}$ with 95% confidence intervals (in parentheses) for the six basins containing water this cold (see Fig. 3.4), and their sum.

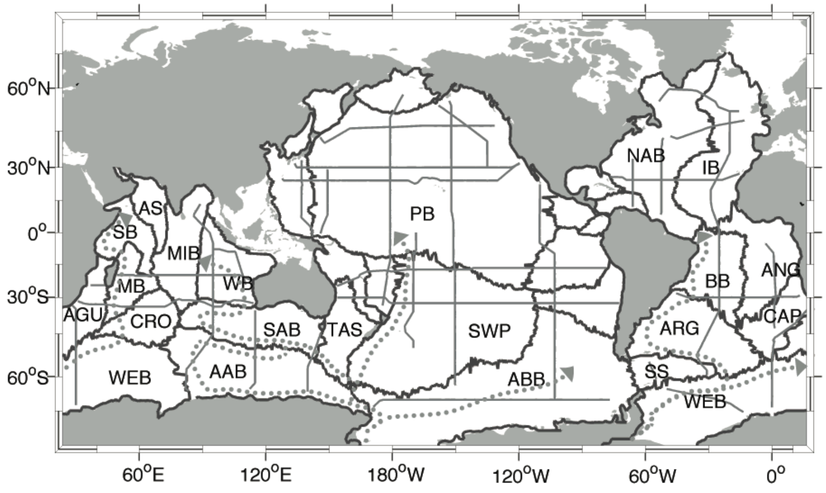

FIG. 3.1. Basin boundaries (thick lines), oceanographic sections (thin lines), and schematics of the four northward pathways of Antarctic Bottom Water out of the Southern Ocean (gray dotted lines). Key basins are labeled with abbreviations: Agulhas-Mozambique Basin (AGU), Crozet Basin (CRO), Madagascar Basin (MB), Somali Basin (SB), Arabian Sea (AS), Mid-Indian Basin (MIB), Wharton Basin (WB), South Australian Basin (SAB), Australian-Antarctic Basin (AAB), Tasman Sea (TAS), Pacific Basin (PB), Southwest Pacific Basin (SWP), Amundsen-Bellingshausen Basin (ABB), Scotia Sea (SS), Weddell-Enderby Basin (WEB), Argentine Basin (ARG), Brazil Basin (BB), North Atlantic Basin (NAB), Iberian/Canary/Cape Verde Basin (IB), Angola Basin (AB), and Cape Basin (CAP).

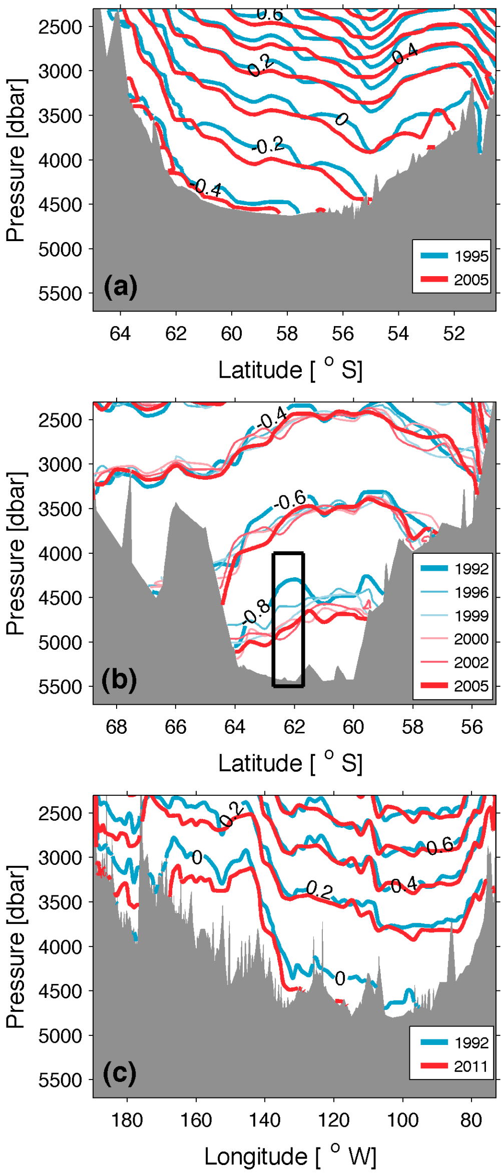

FIG. 3.2. Vertical-lateral profiles of select potential isotherms for each occupation of a) I09 across the Australian-Antarctic Basin, b) A12 across the Weddell-Enderby Basin, and c) S4P across the Amundsen-Bellingshausen Basin (Figs. 1 and 6). Contours of the earliest occupations are labeled and bottom topography (Smith and Sandwell 1997) is shaded gray. The black box in b is discussed in Fig. 3.3.

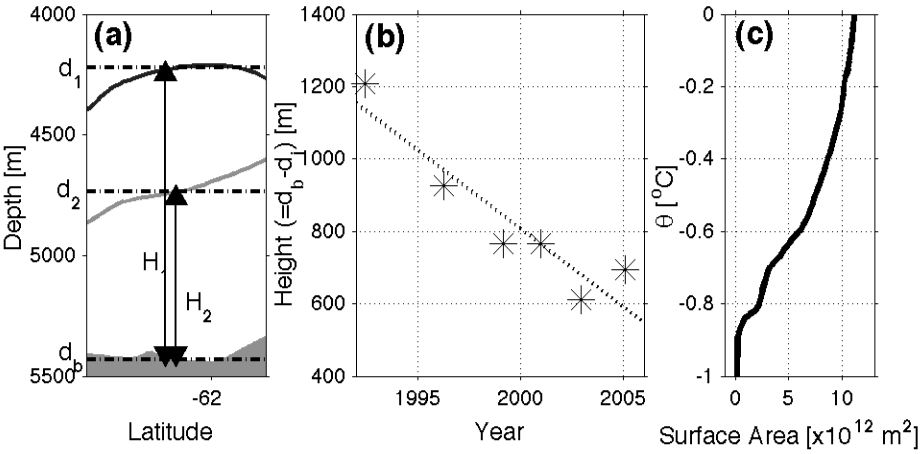

FIG. 3.3. Illustration of a sample volume contraction calculation taken from A12 in the Weddell-Enderby Basin at 62.2°S. a) Detail of black box in Fig. 3.2b. Only the depth and thickness for the 1992 (dark gray line and H_1) and 2005 (light gray line and H_2) -0.8°C potential isotherm are shown with bottom topography (Smith and Sandwell 1997) shaded gray. b) Height of $\theta = -0.8$°C above the bottom (H) at 62.2°S during each occupation (asterisks) with a least-squares linear fit (dotted line). c) Surface area of each given θ in the Weddell-Enderby Basin estimated from a climatology (Gouretski and Kolterman 2004).

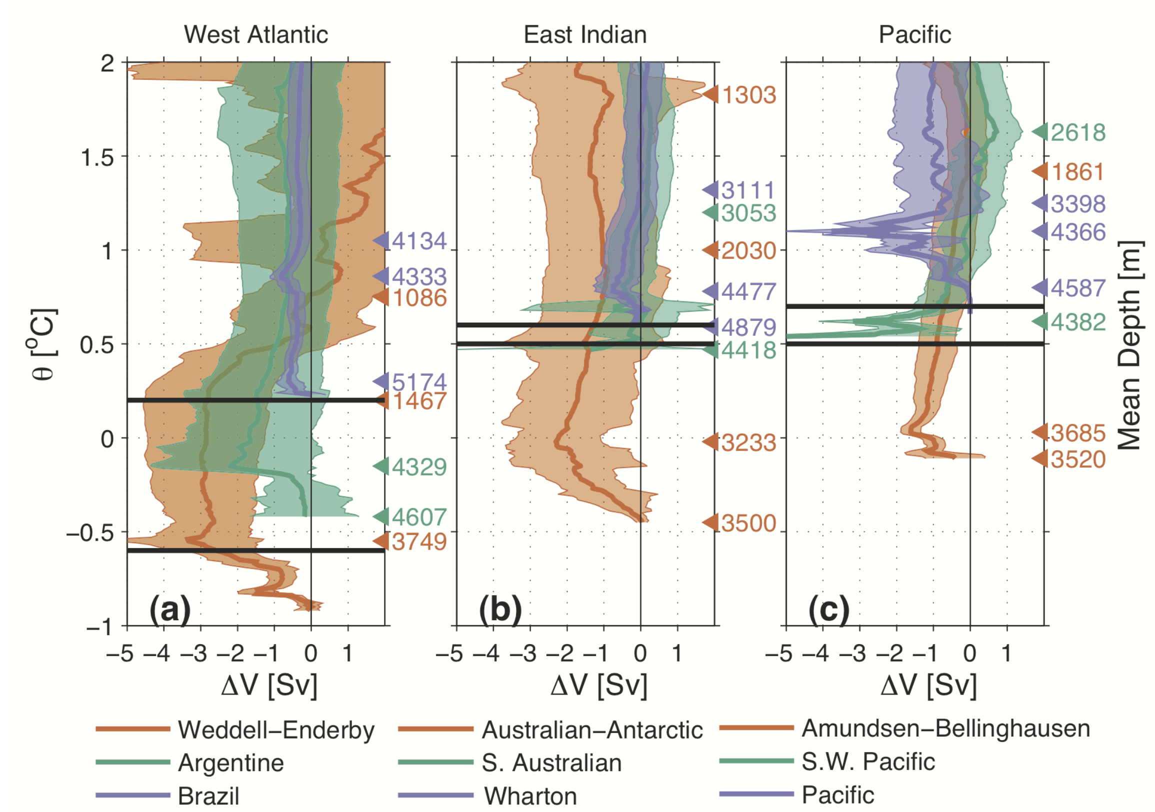

FIG. 3.4. Total rates of volume change for select basins (legends) below each potential isotherm (ΔV curves, solid lines) with 95% confidence intervals (shading) along three of the four northward pathways for AABW out of the Southern Ocean from south to north (orange through green to purple). Minimum θ values spreading from the orange to the green basins (lower horizontal black lines) and the green to the purple basins (upper horizontal black lines) are estimated from a climatology (Gouretski and Kolterman 2004). Color-coded numbers along the right axis indicate mean depths of selected θs for the corresponding basin.

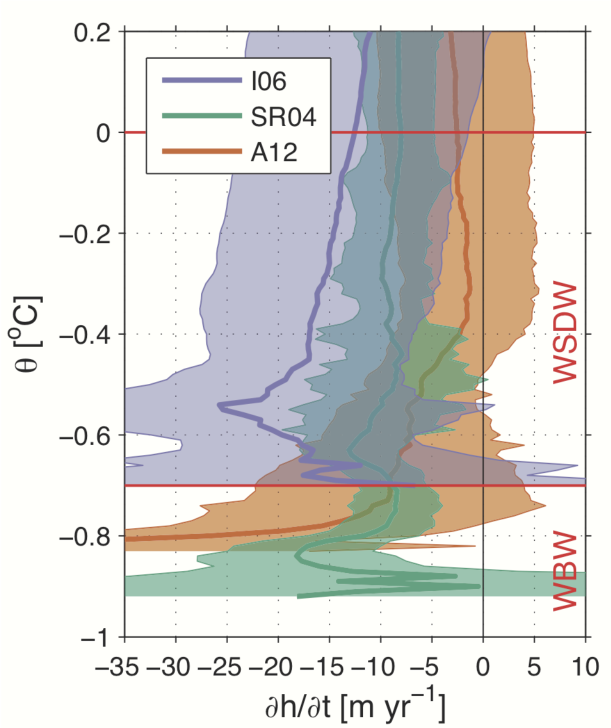

FIG. 3.5. Mean time rate of change in height above the bottom for potential isotherms along three repeat hydrographic sections across the Weddell-Enderby Basin (solid lines; legend; see Fig. 3.6 for locations) with 95% confidence intervals (shaded). Horizontal red lines indicate classically defined (Carmack and Foster 1975) limits of WSBW ($\theta < -0.7$°C) and WSDW ($-0.7 < \theta < 0$°C).

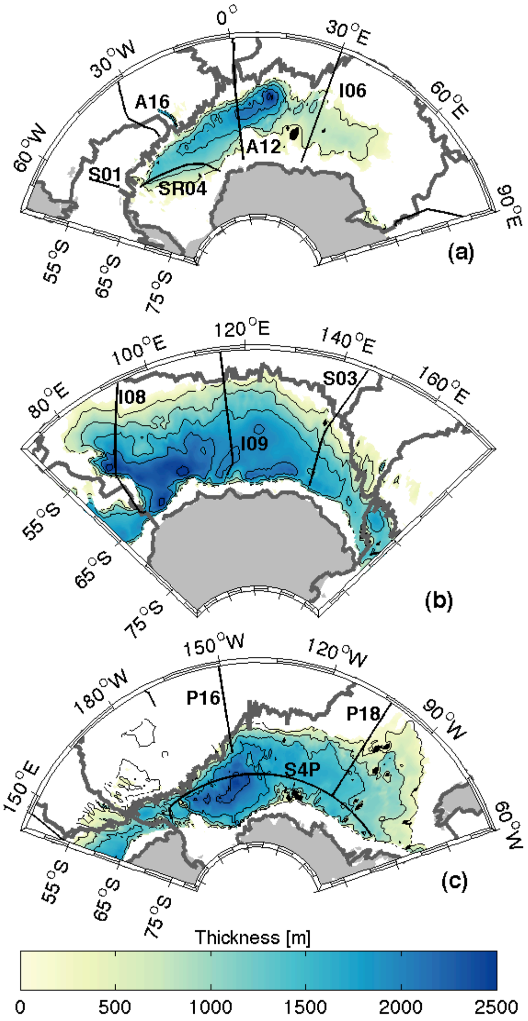

FIG. 3.6. Thickness (color contours) below select climatological (Gouretski and Kolterman 2004) potential isotherms contained in the southern basins: a) θ = -0.6°C isotherm in the Weddell-Enderby Basin, b) θ = 0.4°C isotherm in the Australian-Antarctic Basin, and c) θ = 0.4°C isotherm in the Amundsen-Bellingshausen Basin. Basin boundaries (thick gray lines), land (shaded gray), and repeat oceanographic sections (black lines) with their WOCE designators are plotted.

Chapter 4

Antarctic Bottom Water warming and freshening: Contributions to sea level rise, ocean freshwater budgets, and global heat gain

(Ciitation: Purkey, S. G. and G. C. Johnson, 2013: Antarctic Bottom Water warming and freshening: Contributions to sea level rise, ocean freshwater budgets, and global heat gain. Journal of Climate, 26, 6105-6122, doi:10.1175/JCLI-D-12-00834.1)

Abstract:

Freshening and warming of Antarctic Bottom Water (AABW) between the 1980s and 2000s are quantified, assessing the relative contributions of water-mass changes and isotherm heave. The analysis uses highly accurate, full-depth, ship-based, conductivity-temperature-depth measurements taken along repeated oceanographic sections around the Southern Ocean. Fresher varieties of AABW are present within the South Pacific and South Indian oceans in 2000s compared to the 1990s, with the strongest freshening in the newest waters adjacent to the Antarctic continental slope and rise indicating a recent shift in the salinity of AABW produced in this region. Bottom waters in the Weddell Sea exhibit significantly less water-mass freshening than those in the other two southern basins. However, a decrease in the volume of the coldest, deepest waters is observed throughout the entire Southern Ocean. This isotherm heave causes a salinification and warming on isobaths from the bottom up to the shallow potential temperature maximum. The water-mass freshening of AABW in the Indian and Pacific sectors is equivalent to a freshwater flux of 73 ±26 Gt yr^{-1}, roughly half of the estimated recent mass loss of the West

Antarctic Ice Sheet. Isotherm heave integrated below 2000 m and south of 30 °S equates to a net heat uptake of 34 ±14 TW of excess energy entering the deep ocean from deep volume loss of AABW and 0.37 ±0.15 mm yr^{-1} of sea level rise from associated thermal expansion.

4.1 Introduction

Antarctic Bottom Water (AABW) is the Southern Ocean's coldest, densest water mass. It ventilates the lower limb of the Meridional Overturning Circulation (MOC; e.g. Lumpkin and Speer 2007), filling most of the world's deep basins (Johnson 2008). In recent decades AABW has warmed (e.g. Purkey and Johnson 2010; hereafter P&J 2010), freshened (e.g. Johnson et al. 2008; Swift and Orsi 2012), and decreased in volume (e.g. Kouketsu et al. 2011; Purkey and Johnson 2012, hereafter P&J 2012), possibly linked to the increase in the glacial melt fresh water fluxes into AABW formation regions around Antarctica (e.g. Jacobs and Guilivi 2010). The freshening decreases the salinity of the shelf waters, thence AABW, and appears to slow AABW production and thus the lower limb of the MOC. Here we examine AABW property changes throughout the Southern Ocean, separating the component owing to θ–S (potential temperature–salinity) changes from that due to changes in the depth of potential isotherms (heave). Heave reflects changes in AABW volume, related to changes in the formation rate, circulation, or perhaps even formation properties of AABW. A shift in the θ–S curve indicates a change in water-mass properties. Decomposing the observed deep changes into these components allows for evaluation of the relative contributions of these changes to local Sea Level Rise (SLR), freshwater, and heat budgets.

AABW is a combination of very cold and relatively fresh water formed on shallow continental shelves and warmer, saltier offshore Circumpolar Deep Water (CDW; Foster and

Carmack 1976). The shelf waters form over shallow ice-covered continental shelves where brine rejection from sea ice formation and export increases the salinity of surface waters. This water sinks, mixing with adjacent CDW, and circulates under the ice shelf, melting the overlying ice at depth, causing the shelf waters to freshen (Jacobs 2004). These processes result in a reservoir of very cold, dense shelf water that, when it leaves the shelf, flows down the continental slope, further mixing with CDW (Jacobs 2004).

AABW formation occurs in the Ross Sea, Adelie Coast, and Weddell Sea, producing three distinct varieties of AABW (Orsi et al. 1999): Ross Sea Bottom Water (RSBW), Adelie Land Bottom Water (ALBW), and Weddell Sea Bottom Water (WSBW). These water masses mix with overlying CDW in the Antarctic Circumpolar Current (ACC) before feeding into the lower limb of the MOC and traveling to the northern ends of the Pacific, West Atlantic, and Indian oceans (Johnson 2008). AABW is often defined as water with neutral density $\gamma_n > 28.27$ kg m^3 found south of the SubAntarctic Front (SAF; Orsi et al. 1999). Here we use an older definition for AABW of deep Southern Ocean waters of $\theta < 0$°C (e.g. Gordon 1972), because we use θ, rather than γ_n, as a vertical coordinate.

AABW freshening has been observed (Aoki et al. 2005; Jacobs and Giulivi 2010; Swift and Orsi 2012) and slowdown of AABW formation rates inferred (P&J 2012) in the Ross Sea and Australian-Antarctic Basin starting as early as the 1950s. Ross Sea Shelf Water, an important constituent of RSBW, has freshened by 0.03 decade^{-1} between 1958 and 2008 (here salinity is reported on the 1978 Practical Salinity Scale (PSS-78) a dimensionless scale derived from the conductivity of the sampled seawater). This freshening is associated with freshening of the coastal current connecting the Amundsen Coast to the Ross Sea Shelf (Jacobs and Giulivi 2010). Along the west side of the Ross Gyre, within the deep western boundary current transporting the recently formed RSBW northwestward, the densest water seen in 1994 completely disappeared by 2011, the deep and surface constituents of the shelf water freshened, and thickness of the RSBW outflow decreased by a few hundred meters (Swift and Orsi 2012). Directly downstream from its formation region in the Australian-Antarctic Basin, ALBW has freshened by 0.03 PSS-78 between 1994 and 2002 (Aoki et al. 2005). In the deep Australian-Antarctic Basin, ventilated by both RSBW and ALBW, freshening is evident throughout the basin, owing either to fresher bottom water or different ratios of RSBW and ALBW (Whitworth III 2002; Rintoul 2007; Johnson et al. 2008). In both the Australian-Antarctic Basin and the Ross Sea, cooling on isopycnals and warming on isobars are also present (Aoki et al. 2005; Johnson et al. 2008; Jacobs and Guilivi 2010; P&J 2010).

In the Weddell Sea, bottom water and deep water have been warming with little change in salinity (Robertson et al. 2002; Fahrbach et al. 2004; 2011; P&J 2010). To the north, the deep waters in the Scotia Sea and Argentine Basin, both directly fed by WSBW, have warmed and decreased in volume for at least the past three decades (Coles et al. 1996; Johnson and Doney 2006; Meredith et al. 2008; P&J 2012).

Outside the Southern Ocean, the abyssal waters along the bottom limb of the MOC fed by AABW (Johnson 2008), have warmed around the globe (P&J 2010; Kouketsu et al. 2011). The global-scale warming could be caused by a decrease in AABW formation rates, causing isopycnals to fall, hence the observed warming on isobaths. This signal can be communicated remotely by planetary waves throughout the world ocean on much shorter time scales than advective changes (Masuda et al. 2010; Kouketsu et al 2011; P&J 2012). AABW warming has been analyzed in the Western South Atlantic (Johnson and Doney 2006; Zenk and Morozov

2007), throughout the Pacific (Fukasawa et al. 2004; Johnson et al. 2007; Kawano et al. 2010) and in the eastern Indian Ocean (Johnson et al. 2008; P&J 2010).

Much of the recent AABW property changes observed around the globe may be owing to increased glacial freshwater discharge from a number of locations around Antarctica over recent decades (e.g. Jacobs and Guilivi 2010). Antarctic ice shelf thinning and glacial discharge acceleration are strongest along the West Antarctic Peninsula and the Amundsen Coast (Rignot and Jacobs 2002; Rignot et al. 2008), with a net ice sheet loss of 88 ±54 Gt yr^{-1} in the West Antarctic and 60 ±46 Gt yr^{-1} along the peninsula between 1992–2006 (Rignot et al. 2008). Between 1991 and 2001 154 ±16 km^3 of glacier ice was lost to the Amundsen Sea with acceleration of coastward glacier flow (Shepherd et al. 2002). At Pine Island Glacier, a location with one of the highest melt rates, the ice shelf has recently been thinning at a rate of 5.5 m yr^{-1} through basal melting owing to a 0.5 °C warming of ocean waters under the ice shelf (Shepherd et al. 2004). Similarly, along the Amundsen and Bellingshausen coasts where warm CDW has access to the shelf, the melting rates on the submerged undersides of glaciers have been correlated with warming ocean temperatures, with melting increasing by 1 m per 0.1 °C of warming (Rignot and Jacobs 2002).

The observed AABW property and circulation changes are important for global heat and SLR budgets (P&J 2010; Kouketsu et al 2011). The deep ocean warming below 4000 m globally is equivalent to a net heat uptake of 0.027 ±0.009 W m^{-2} over the surface the Earth and 0.05 mm yr^{-1} mean global SLR (P&J 2010). In the Southern Ocean, the warming below 1000 m is equivalent to as much as a 1.2 W m^{-2} local heat flux and 1.3 mm yr^{-1} local SLR (P&J 2010).

Here we evaluate salinity and temperature changes within the deep Southern Ocean, distinguishing between heave and water property changes. Section 2 discusses the data set and processing, including inter-cruise salinity adjustments (see also Appendix A). Section 3 presents methods used to distinguish heave from water-mass changes. Section 4 discusses freshening trends throughout the Southern Ocean, using multiple Southern Ocean sections occupied two or more times since the 1980s. Section 5 estimates basin-mean rates of change to find the contributions of the deep Southern Ocean to changes in SLR, heat budgets and freshwater budgets. Section 6 discusses these results.

4.2 Data and Processing

We use full-depth, high-resolution, highly accurate, ship-based hydrographic data collected in the Southern Ocean since 1980 at locations with two or more occupations. The data were mostly collected as part of the international World Ocean Circulation Experiment (WOCE) Hydrographic Programme under the Global Ocean Ship-based Hydrographic Investigation Program (GO-SHIP). All publicly available data at http://cchdo.ucsd.edu as of November 2012 are considered here. We refer to each section by its WOCE ID (Fig. 4.1, Table 4.A1). All data collected along a section within a year are combined and referred to as a single occupation of that section, referenced by the calendar year in which the earliest station was taken (Table 4.A1).

We focus on sections located at or south of 30 °S (Fig. 4.1): nine meridional sections roughly spaced every 45° longitude, two zonal sections at ~67 °S across the Ross Sea and the Weddell Sea, and three zonal sections that together completely circumnavigate the globe near 30 °S (Fig. 4.1). Most of the meridional sections in the Indian and Atlantic sectors extend to the Antarctic continental shelf, but both of the sections in the Pacific sector stop short of the shelf (Fig. 4.1). Along each section data were collected from the surface to approximately 10 m from the bottom at stations nominally spaced every 55 km. Each re-occupation of a given section analyzed here lies within 10 km of the original. Data along each section are interpolated onto an evenly spaced 20-dbar vertical and 2’ horizontal grid following P&J (2010).

Data were collected between 1980 and 2012, with the length-weighted mean first occupation in 1991 and the last in 2008. Each section has been occupied between two and eight times with the length-weighted mean and median for the study region of 3.6 and 3.0 occupations, respectively (Table 4.A1). Therefore, the along-section trends discussed here span on average an 18-year period. Most trend estimates are based on data from at least three occupations; however, some trends are based on the difference between two occupations (Table 4.A1).

All data were collected with a Conductivity-Temperature-Depth (CTD) instrument with target measurement accuracy better than 0.002 °C for temperature, 3 dbar for pressure, and 0.002 PSS-78 for salinity (Joyce 1991). All CTD temperature data were reported in, or converted to, the 1968 International Practical Temperature Scale (IPTS-68) for use with the 1980 Equation of State (EOS-80). The CTD salinity measurements were all standardized with International Association for Physical Science of the Oceans (IAPSO) Standard Seawater (SSW), with all salinity values reported here on PSS-78. We consider only data with good quality flags and remove any obvious spikes in salinity data.

We apply known salinity offsets owing to the different IAPSO SSW batches used on the different cruise legs to the salinity data (Table 4.A1). Batch-to-batch offsets are from Kawano et al. (2006) and T. Kawano (personal communication 2011). They range from -1.2×10^{-3} to 2.5×10^{-3} PSS-78 (Table 4.A1). SSW offsets could not be applied to 13 of the 73 Southern Ocean cruise legs analyzed here owing to 8 legs having no SSW batch number information available and 5 cruises using SSW batches too recent to have an offset estimate.

Additional ad-hoc salinity adjustments are estimated and applied to the CTD salinity data to further minimize intercruise measurement biases (Appendix A, Table 4.A1, Figure A1). These salinity offsets are calculated by comparing salinity data in select geographical regions containing water that has been isolated from the surface for a relatively long time and is hence well-mixed with a very tight (low variance) θ-S relation (Appendix A). These additional offsets are necessary because of the relatively large contribution of salinity to density and the relatively high ratio of measurement error to signal observed here (Appendix A).

The ad-hoc salinity offsets are applied to 67 of the 73 Southern Ocean legs with magnitudes ranging from essentially zero ($< 10^{-6}$ PSS-78) to as high as 0.0056 PSS-78, with 63 of the applied offsets being less than the WOCE target accuracy of 0.002 PSS-78 (Fig. A1). The four legs with offset magnitudes > 0.002 PSS-78 are the 1984 occupation of P16, the 1993 and 1995 occupations of S03, and the 2011 occupation of A16 (Fig. A1; Table 4.A1). A salinity offset could not be applied to six legs. These legs include the three occupations of S01 through the Drake Passage (Fig. 4.1) where highly variable water properties did not allow a suitable place for intercruise comparisons. Also three subsections of full lines are not long enough for salinity comparisons, namely the 1995, 2006, and 1991 occupations of I09, P18, and S03, respectively. The salinity offsets are applied to the raw CTD salinity data and each section occupation is re-gridded vertically and horizontally (P&J 2010).

4.3 Methods: Heave vs. Water Property Changes

Interior ocean property changes can be caused by heave or water-mass changes (e.g., Fig. 4.2). A number of methods have been deployed for distinguishing between heave and water-mass changes. For example, Bindoff and McDougall (1994) decompose ocean property changes using S and θ changes on both density and pressure surfaces and the original θ-S curve to solve for the contributions of isopycnal heave, temperature changes, and salinity changes, whereas McDonagh et al. (2005) calculate water-mass changes by calculating the "minimum distance" between chronological θ-S curves, scaling them by thermal expansion and haline contraction coefficients.

Here we use θ as the independent variable instead of density to allow detection of very small deep θ-S changes. We make this choice because S errors have significantly more impact on density than θ errors, especially in cold deep waters. For example, at 4000 m in the Ross Sea, the expected measurement salinity error of 0.002 PSS-78 will cause an error in density fifteen times larger than the expected temperature error of 0.001 °C would cause. Therefore we choose the most accurate measurement, θ, to be the independent variable in our analysis, rather than density, which would amplify any remaining S errors.

As a result of this choice, here heave refers to a vertical shift of the water column caused by a change in depth (equivalently pressure) of a potential isotherm that has no effect on the local θ-S relationship (Fig. 4.2b). Alternatively, a water-mass change is reflected in a shift in the shape of the θ-S curve with time (e.g. Fig. 4.2a). If density surfaces were used as the vertical coordinate, water mass and heave changes reported here would be amplified, as salinity generally decreases with descreasing temperature within AABW in the Southern Ocean.

While this method clearly identifies where θ-S changes occur, it casts all the water-mass changes in terms of salinification (or freshening) and all warming (or cooling) as owing to heave. For example, imagine a scenario in the deep Southern Ocean (where θ decreases and S increases with increasing depth) where the whole water column warms, causing the θ-S curve to be displaced upwards. Our analysis would cast this water-mass change as freshening, with a value proportional to the warming by the local slope of the θ-S curve. While deep AABW freshening presented here is traced back to the shelf water changes that are freshening faster than warming (e.g., Jacobs and Guilivi 2010), the limitations of our method should be kept in mind.

To decompose the deep property changes, first we define an initial θ-S relation (θ-S_i) representative of the θ-S at the time of the first occupation at every location along a section. Each vertical profile of S and θ of each section is linearly interpolated onto an evenly spaced θ grid from -2 to 5 °C at 0.01 °C intervals. The interpolation extends from the bottom to the first θ maximum (usually the θ-maximum associated with CDW). All values above the maximum are masked out. The bottom S value of each interpolated S profile is extended to the minimum bottom θ measured at that location among all occupations of the section by using the slope of the linear fit of S vs. θ over the coldest 0.1 °C of each profile. This extension is only applied if the bottom $\theta < 3$ °C, the profile depth > 500 m, and the bottom 0.1 °C spans more than 100 m of the water column. These criteria limit extensions to deeper offshore regions, excluding thermocline or continental shelf waters. Finally, S_i at each θ-grid is estimated for the time of the first occupation from linear fits of S vs. time for all occupations. If there are only two occupations, then S_i matches S of the first occupation, but if there are multiple occupations of a section, then S_i will differ from S of the first occupation.

The θ-S_i relations are used to calculate expected S values, S_H, if heave were the only contributor to the changes in S. At each vertical and horizontal gridpoint for each occupation, a value of S_H is computed from θ using a spline interpolant and the local θ-S_i relation.

Finally, we calculate S rates of change for the total (S_T), S_H, and water-mass shift (S_{WM}) with time and associated error as follows. At every horizontal and vertical grid point along each section with at least two occupations spanning more than 2.5 years (following P&J 2010) the rate of change of total S with time (dS_T/dt) and dS_H/dt are estimated by linear least-squares (e.g. Fig. 4.3). Where only two occupations exist, the rates of change reflect differences between these two occupations. Within the Southern Ocean below 300 m, the trend error along sections with more than two occupations is usually less than 0.4×10^{-3} PSS-78 yr^{-1}, smaller than most of the along-section signal (e.g. Fig. 4.3). The rate of change in salinity with time owing to water–mass shifts, $dS_{WM}/dt = dS_T/dt - dS_H/dt$, is calculated along each section (e.g. Fig. 4.3a,d,g,j,m). In addition, the rate of change of θ with time (dθ/dt) is found also using a linear least-squares fit (not shown, see P&J 2010).

For each deep basin (following P&J 2012; Fig. 4.1), the rates along all sections within a given basin are used to find basin-mean rates and associated errors within 0.05 °C-thick bins below 5 °C. Along each section within a basin, using the mean θ from all occupations, a θ-bin is identified as the region where θ falls within ±0.025 of a given value. Within each θ-bin area, first the vertical mean dθ/dt, dS_T/dt, dS_{WM}/dt, and dS_H/dt are calculated along the sections. The vertical length of the given θ-bin at each location along the section is used to find a horizontal length-weighted mean rate (hereafter basin mean rates) for each θ-bin using all sections within a basin as if they were lined up end-to-end. The horizontal variance along a θ-bin is much larger than the vertical variance within a θ-bin. Therefore, we calculate and use the horizontal standard deviation of the vertical mean rates along a given isotherm (hereafter, basin standard deviations) for the basin error analyses. The basin standard deviations are also calculated as if all sections within a basin were connected end-to-end, a more conservative choice than the section length-weighted mean technique used in P&J (2010). In addition, the basin standard deviations are usually larger than the slope errors on the rates themselves. Slope errors are neglected in the final error analysis, since they cannot be determined for most sections. Finally the degrees of freedom (DOF) for each isotherm bin are calculated using the horizontal length of the θ-bin following P&J 2010 assuming a 163–km decorrelation length scale (P&J 2010). The 95% confidence intervals are found for each basin for each θ-bin assuming a Student's t-distribution (e.g. Fig. 4.4).

The 95% confidence intervals reported here are based on the spatial variance of trends along the sections and do not fully resolve the error associated with temporal variability in the trend. However, as noted earlier, the trend errors in time along sections with more than two occupations (the majority of the sections analyzed) are generally smaller than the signal. In addition, the consistent patterns seen throughout the Southern Ocean in all sections analyzed (section 4), all occupied over varying time periods, increases confidence that the basin mean rates reported here reflect a fairly consistent decadal change, at least from the 1980s through the 2000s. Furthermore, in the few areas with better temporal sampling, fairly steady AABW warming has been observed over the past few decades (e.g., Zenk and Morozov 2007). However, to resolve fully the temporal variability and determine if the changes are associated with a secular trend, an oscillation, or have a more complex temporal pattern over the 30-year reporting period would require a higher temporal resolution large-scale data set.

4.4 Results

Throughout the Southern Ocean, water colder than 0 °C in each of the deep basins is freshening owing to water-mass changes, albeit in varying amounts, and becoming saltier below the CDW S-maximum owing to heave. The net effect is a deep freshening in the Indian and Pacific below 0°C with salinification above (Fig. 4.3a–l; Fig. 4.4b-c). In the South Atlantic, heave dominates to effect a nearly full water column salinification (Fig. 4.3m–o; Fig. 4.4a).

In the South Pacific, water-mass freshening dominates the total S signal in waters of θ < 0 °C throughout the Ross Gyre (west of 140ºW; Fig 3a,b,c), with freshening increasing by an order of magnitude to 3 (±2) × 10^{-3} PSS-78 yr^{-1} in the waters along the continental rise on the western side of the basin where the purest and most recently formed RSBW flows westward (Jacobs and Giuivi 2010). This strongest freshening along the continental rise in the coldest waters (θ < -0.4 ºC) is almost completely owing to water-mass shifts (Fig. 4.4f), and is consistent with the total freshening reported by Swift and Orsi (2012) in this region. Within the interior of the Ross Gyre, water-mass freshening is ~0.2 × 10^{-3} PSS-78 yr^{-1} for θ < 0 °C (Fig. 4.3a; Fig. 4.4c). The heave component causes an ~0.03 × 10^{-3} PSS-78 yr^{-1} salinification between the bottom and 1000 m (Fig. 4.3b; Fig. 4.4c) owing to a reduction in the volume of the coldest bottom waters, significantly different from zero at 95% confidence in the basin mean for 0.2 < θ < 0.9 °C. These two counteracting factors combine such that water-mass freshening dominates for θ < 0 °C, with a net freshening of 0.16 × 10^{-3} PSS-78 $decade^{-1}$, while heave dominates between 0°C and 1000 m causing a net salinification (Fig. 4.3c; Fig. 4.4c;f). The Amundsen Basin (east of 140ºW) exhibits a slight water-mass freshening and heave salinification for zero net change in salinity along S4P (Figs. 3a–c) and in the two meridional sections that cross the basin (Fig. 4.1; not shown).

In the South Indian, water-mass freshening is present throughout AABW (Fig 3d,g,j), strongest along the continental slope, where recently formed RSBW and ADLW flow westward before flowing north, ventilating the deep Australian-Antarctic Basin (Orsi et al. 1999). Consistent with previous studies (Aoki et al. 2005; Rintoul 2007; Johnson et al. 2008; Jacobs and Giuivi 2010; Shimada et al. 2012), our results show a strong water-mass freshening, with basin-mean rates ranging from 1.2 (±0.6) × 10^{-3} PSS-78 yr^{-1} within the coldest (θ ~ -0.5 °C) bottom water to 0.2 (±0.1) × 10^{-3} PSS-78 yr^{-1} at $\theta = 0$ °C (Fig. 4.4b,e). The freshening signal in the bottom waters ($\theta < -0.2$ °C) becomes gradually fainter from west to east: starting at ~0.6 × 10^{-3} PSS-78 yr^{-1} in S03 (Fig. 4.3d, ~140ºE), to ~0.5 × 10^{-3} PSS-78 yr^{-1} in I09 (Fig. 4.3g, ~115ºE), to ~0.3 × 10^{-3} PSS-78 yr^{-1} in I08 (Fig. 4.3j, ~90ºE). Again, heave partially counteracts this freshening in all sections (Fig. 4.3e,h,k). The basin mean dS_H/dt accounts for ~0.15 × 10^{-3} PSS-78 yr^{-1} of salinification, statistically significantly different from zero for $-0.3 < \theta < 0.5$ °C (Fig. 4.4b,e). The basin-mean dS/dt shows a net freshening for $\theta < 0$ °C and mostly a net salinification for $\theta > 0$ °C (Fig. 4.3f,i,l; Fig. 4.4b,e).

In the South Atlantic, less water-mass freshening is observed with more heave salinification, causing a very slight, and statistically insignificant net salinification of ~0.1 (±0.13) × 10^{-3} PSS-78 yr^{-1} throughout the deep waters ($\theta < 0.4$ °C; e.g. Fig.3 m,n,o; Fig. 4.4a,d). The zonal SR04 section across the Weddell Gyre exhibits the most consistent trend among the sections crossing the Weddell-Enderby Basin with a water-mass freshening of ~0.05 × 10^{-3} PSS-78 yr^{-1} in the interior and slightly higher values along its east and west flanks, where the deep westward flow of the southern limb of the Weddell Gyre and the northward-flowing current carrying recently formed WSBW are found, respectively (Gordon et al. 2010). The heave, however, causes a bottom intensified salinification of ~0.1–0.3 × 10^{-3} PSS-78 yr^{-1} throughout much of the water column, consistent with a decrease in the volume of WSBW in the basin (P&J 2012), resulting in a net salinification across most of the section (Fig 3o). Section A12 (0 °E; not shown), which cuts meridionally through eastern end of the Weddell Gyre, is noisier than SR04, but roughly consistent within errors with the pattern seen along SR04. Further to the east, Section I06 (30ºE) across the Enderby Basin shows water-mass freshening of less than 0.1 × 10^{-3} PSS-78 yr^{-1}, smaller than the measurement error, but again consistent with other lines in this basin, along with a compensating heave of ~0.2×10^{-3} PSS-78 yr^{-1} (not shown). Together, these three lines yield a basin-mean salinification of 0.1×10^{-3} PSS-78 yr^{-1}, significantly different from zero at 95% confidence for $-0.2 < \theta < 0.5$ °C (Fig. 4.4a).

North of the Weddell-Enderby Basin, the Scotia Sea and the Argentine Basin, both fed by AABW from the Weddell Sea and vicinity (Fig. 4.1), show little bottom water salinity change rising above the noise. SR01 across Drake Passage (not shown) is extremely noisy and we can find no discernable signal. All sections crossing the Argentine Basin shows little water-mass change but a slight salinification owing to deep isotherm heave (not shown).

Finally, the basin-mean $d\theta/dt$ for all three of the southernmost basins exhibits statistically significant warming trends ranging from 0.002–0.005 °C yr^{-1} for $\theta < 0.5$ °C (Fig.4g-i). This trend is comparable to the 0.003 °C yr^{-1} warming P&J (2010) found below 3000 m south of the SAF, only here we have averaged along depths of mean potential isotherms within each basin instead of on isobaths as done in P&J (2010). The basin-mean $d\theta/dt$ is more consistent along depth of mean isotherms (Fig. 4.4g–I vs. P&J (2010) Fig. 9d), arguably making this new calculation the preferable method.

4.5 Freshwater, heat, and SLR budgets

Here we apply the basin means (Fig. 4.4) for water-mass, heave, total S, and θ trends over the entire Southern Ocean, here defined as south of 30°S, to evaluate their contributions to ocean freshwater budgets (Section 5a), global heat budgets (Section 5b), and SLR (Section 5c). For basins and the entire domain, the budget calculations are conducted from the bottom to three upper bounds: climatological $\theta = 0$ °C as a rough proxy for the upper boundary of AABW (Foster and Carmack, 1976), 4000 m for a deep ocean estimate where water properties are most strongly influenced by AABW (Johnson 2008; following P&J 2010), and 2000 m to extended our analysis to the current maximum sampling depth of Argo floats (e.g. Roemmich et al. 2009).

The basin-mean rates and errors are applied to the climatological θ and S fields (Gouretski and Koltermann 2004). The climatological θ and S vertical profiles are put onto a uniform 20-m depth grid using a shape-preserving piecewise cubic interpolation. Each basin-mean rate and its standard deviation on the θ-grid (Fig. 4.4) are interpolated onto the climatological θ profiles at each horizontal gridpoint, assigning all four rates and their standard deviations as discussed above. Regions above the CDW θ maximum are not considered here since the method used does not allow it. Given the focus on AABW changes, this limitation is minor.

4.5.1 Freshwater budget:

Here we quantify the fresh water uptake owing to deep water-mass changes in the deep Southern Ocean, including in AABW, and compare its magnitude to that of the excess mass flux off Antarctica in recent decades from ice melt. We estimate the freshwater flux by calculating the amount of freshwater (V_{fw}) necessary to add to an initial volume (V_i) with initial salinity (S_i) in order to cause the water to freshen at the observed dS_{WM}/dt over a 1-year period to a final salinity (S_f). If salt is conserved and we only change the salinity by adding freshwater to the system to change V_i to a final volume (V_f), then V_{fw} is calculated as:

$$V_{fw} = \int V_f - V_i = \int \left(\frac{S_i}{S_f} - 1 \right) \cdot dv, \tag{1}$$

neglecting the relatively small change in density. Here S_i is the gridded climatological salinity (Gouretski and Koltermann 2004) and S_f is calculated by applying dS_{WM}/dt for one year at each climatological grid point. The *dv* for each grid point is calculated as the volume of the half-degree longitude by a half-degree latitude by 20-m depth box. Local freshwater fluxes in m yr^{-1} are found by integrating in the vertical from the bottom upwards to $\theta = 0$ ºC, 4000 m, and 2000 m (Fig. 4.5) and basin totals by integrating over the whole basin below these same surfaces (Table 4.1). The standard deviations of V_{fw} for the basin means are found by applying S_f ± one standard deviation of S_f in (1). The basin DOFs are θ volume-weighted mean along-isotherm DOFs below a given surface (Fig. 4.4) and the 95% confidence intervals (Table 4.1) are calculated using Student's t-distribution. Finally, a total for the whole Southern Ocean below each top surface is calculated as a sum of all the basin values south of 30 °S with 95% confidence intervals found using the sum of the basin standard deviations and DOFs (Table 4.1). Again, the 95% confidence intervals reflect the spatial variance of the trend estimates, and assume that the along-section variability in each basin is representative of that within the entire basin (Table 4.1).

Local estimates from the bottom to $\theta = 0$ ºC show the largest deep freshening occurring in the west Pacific and Indian Ocean sectors (Fig. 4.5). The local freshwater flux in these regions for $\theta = 0$ ºC exceeds 0.02 m yr^{-1} over the north-west corner of the Amundsen–Bellingshausen Basin and most of the deep portions of the Australian-Antarctic Basin (Fig. 4.5a), despite $\theta < 0$ ºC occupying only ~1000–1500 m of the water column. This flux is equivalent to total freshwater additions of 25 ±9 and 48 ±36 Gt yr^{-1} into the Amundsen-Bellingshausen and Australian-Antarctic basins, respectively (Table 4.1), suggesting that a large fraction of the estimated recent 140 Gt yr^{-1} freshwater flux from ice melt (Rignot et al. 2008) may be taken up by freshening AABW.

The Weddell-Enderby Basin also shows a slight freshwater flux of 5cm yr^{-1} below $\theta = 0$ °C (Fig.5). This small amount reflects the very slight observed 0.1×10^{-3} PSS-78 yr^{-1} water-mass freshening (Fig. 4.4a) applied to the relatively large volume of AABW, with water of $\theta \leq 0$ °C as much as 4000 m in thickness (e.g. Fig. 4.3m). The relatively large volume of AABW combined with the small water-mass freshening, gives an uncertain total freshening of 24 ±54 Gt yr^{-1}.

Integrating vertically to 4000 and 2000 m further emphasizes the pattern discussed above south of the SAF and shows a strong water-mass salinification in the North Atlantic Deep Water (NADW) north of the SAF at intermediate depths (Fig. 4.5, Table 4.1). Integrating to 4000 m (Fig 5b), containing only a fraction of $\theta < 0$ °C (Fig. 4.3; bold black contours), gives a fraction the freshening seen for $\theta < 0$ °C (Fig. 4.5a). Integrating to 2000 m (Fig. 4.5c), the local water-mass freshwater flux south of the SAF is almost identical as that from integrating to the 0 °C isotherm, indicating that water-mass freshwater changes are mostly constrained to $\theta < 0$ °C with little water-mass freshening in the waters between 0 °C and 2000 m (Fig. 4.3a,d,g,j). South of the SAF 2000 m lies below CDW entering from the north, therefore, none of these isotherms or isobar surfaces reflect changes in CDW south of the SAF. However, north of the SAF between 2000 and 3000 m, in the waters heavily influenced by NADW ($\theta \sim 2.8$ °C) a strong salinification is observed, seen as a negative local fresh water fluxes of between -1 and -10 cm yr^{-1} in the local fluxes (Fig 5c). These waters are also freshening and warming from heave (not shown). The property changes in these regions are separate from the deep AABW changes discussed in this paper, and likely indicate physical changes in the NADW in these regions.

4.5.2 Heat budget

We find large and statistically significant heat uptake in each basin and the whole Southern Ocean for $\theta < 0$°C, below 4000 m, and below 2000 m (Table 4.1). The rate of heat gain (Q) is given by

$$Q = \int \rho \cdot C_p \cdot {}^{d\theta}\!/_{dt} \cdot dv, \tag{2}$$

where density (ρ) and heat capacity (C_p) are calculated from the climatological θ, S, and pressure at each grid point. The standard deviation of Q is found by replacing dθ/dt in (2) with the standard deviations of dθ/dt. We sum the errors because the individual grid points are not independent of each other. The total DOF and 95% confidence intervals for each basin and total Southern Ocean (Table 4.1) are estimated by previously described methods (Section 5a). We find a large, statistically significant, heat gain thoughout the water column in the Southern Ocean. Totals found here are slightly smaller than P&J 2010 (discussed further in Section 6), but agree within uncertainties.

4.5.3. Sea Level Rise

Changes in density of AABW owing to dS_T/dt, dS_{WM}/dt, dS_H/dt and dθ/dt contribute to halosteric and thermosteric SLR. We calculate the contribution of each component to SLR using:

$$SLR_{halosteric} = \frac{\int -\beta \cdot {}^{dS}\!/_{dt} \cdot dv}{SA} \text{ and } SLR_{thermosteric} = \frac{\int \alpha \cdot {}^{d\theta}\!/_{dt} \cdot dv}{SA}, \tag{3}$$

where the thermal expansion coefficient, α, and the haline contraction coefficient, β, are calculated locally from the climatological gridded θ, S, and pressure. For a local estimate, the integral is evaluated vertically from the bottom to a top surface at each grid point where the surface area (SA) has the surface area of that grid point, yielding its contribution to local SLR in mm yr^{-1} (Fig. 4.6). Again, the top surfaces considered here are θ = 0 °C, 4000 m, and 2000 m. For each basin an average SLR is calculated following (3) where the volume integral is now over the entire region from the bottom to the top surface under consideration, and SA is the surface area of that top surface for the basin (Table 4.1). The gridded standard deviations are integrated again using (3) to estimate the total basin standard deviation. The 95% confidence intervals are estimated assuming Student's t-distribution and using the total DOF below a given surface as described in Section 5a.

Water-mass freshening tends to reduce SLR in all three southernmost basins while the heave salinification raises SLR (Fig. 4.6). The local effects of water-mass freshening vary spatially, but follow the spatial patterns seen in the freshwater flux (Fig. 4.5), with the strongest signal seen in the South Pacific and South Indian (Fig 6a,e,i). Heave salinification counteracts some of the SLR, except in the Amundsen-Bellingshausen Basin where S is almost constant versus θ in deeper, colder waters (Fig. 4.6b,f,j; Table 4.1). The net effect is a slight (~-0.02 mm yr^{-1}) local negative SLR in the South Atlantic and a net positive (~0.03 mm yr^{-1}) SLR in the South Pacific and South Indian sectors of the Southern Ocean (Fig. 4.6c,g,k; Table 4.1). In total, the Southern Ocean salinity changes have a near-zero net effect on SLR (Table 4.1), owing to the contribution of salinification in the Weddell-Enderby and Argentine basins almost exactly canceling the contribution of freshening in Australian-Antarctic and Amundsen-Bellingshausen basins. The salinity contribution is smaller than the warming contribution of 1–2 mm yr^{-1} throughout the Southern Ocean (Fig. 4.6d,h,l; Table 4.1).

4.6 Discussion

The Southern Hemisphere has experienced dramatic changes in recent decades owing to increases in atmospheric concentration of greenhouse gases and ozone–depleting chemicals. These changes include increased Southern Ocean warming (Gille 2008), increased glacial melt in the East Antarctic and Antarctic Peninsula (Rignot et al. 2008), a global slowdown of the bottom limb of the MOC (Kawano et al. 2010, Kouketsu et al. 2011; P&J 2012), and freshening of

AABW (Jacobs and Guilivi 2010, Swift and Orsi 2012). Here we have examined property changes in the deep Southern Ocean, distinguishing between changes in the θ–S relation and vertical heave of θ surfaces within and associated with AABW. We conclude with a discussion comparing the amount of warming and freshening estimated in AABW to the net global radiative imbalance, total glacial meltwater runoff from Antarctica, and global mean SLR.

Freshening of AABW in the Pacific and Indian sectors of the deep Southern Ocean appears to accounts for roughly half of the net Antarctic continental ice melt of recent years. The strongest freshening owing to water-mass shifts is seen near the AABW source regions and follows the path of AABW deep circulation in the three southernmost basins (Fig. 4.5a) reflecting the introduction of a fresher variety of AABW into the deep Southern Ocean. The strongest freshening signal in the youngest AABW waters to the south with no freshening observed in the older AABW further to the north (Fig. 4.5) suggests that this freshening flux may have started relatively recently. The Amundsen coast freshwater flux into the South Pacific and South Indian oceans that freshens the shelf water components of AABW there is probably largely owing to net continental ice melt (Jacobs and Guilivi 2010), estimated to be 140 Gt yr^{-1} over recent decades (Rignot et al. 2008). Our estimates are that the deep Amundsen-Bellingshausen and Australian-Antarctic basins have exhibited increases of 25 ±9 and 48 ±36 Gt $yr^{-1,}$ respectively, of fresh water between roughly 1991 and 2008, making the deep ocean a significant sink for the recent increase in glacial melt. The Weddell Basin also exhibits hints of water-mass freshening, albeit at a slower rate that is smaller than the measurement error. However, the spatial pattern of strongest freshening in the newest AABW and the consistency of the freshening throughout the basin (Fig. 4.3m) suggest that AABW in the Weddell may also be getting fresher.

The heave component of AABW changes found here reflects a loss of volume in AABW over time, seen farther from the source than the advected water mass freshening signal because production rate changes are communicated by pressure waves on much shorter time scales (e.g., Masuda et al. 2010). P&J (2012) found an 8 SV loss in volume of deep Southern Ocean water colder than 0°C, suggesting a recent decrease in the production of AABW. Paleoproxies indicate that the bottom limb of the MOC has been in multiple steady states during different climate regimes (Lynch-Stieglitz et al. 2007). Current water-mass volumes and chemistry of the global inventory of AABW vs. NADW suggest that past rates of AABW production may have been higher, also supporting the hypothesis of smaller production rates of AABW in recent decades (Broecker et al. 1999; Johnson 2008). Here we separate heave from water-mass changes in the deep ocean and show that while the water-mass changes are currently limited to the deep basins adjacent to Antarctica, heave is responsible for part of the deep ocean changes there, and most, if not all, of the deep ocean changes in AABW further north. Furthermore, the deep volume loss of water colder than 0 °C is consistent with the warming and salinification of the water between 0 °C isotherm and 1000 m in the South Indian and South Pacific oceans (Fig. 4.3b,e,h,k,n).

Further investigation of the relative contribution of heave verses water-mass changes in AABW, including the source of the freshening, could be conducted using chemical tracers such as oxygen, nutrients, $\delta^{18}O$, and chlorofluorocarbons along repeated sections. Temporal changes in these chemical tracers would provide additional information about changes in the age, water-properties, and formation rates of the AABW. High-resolution models could also be used to examine the possible mechanisms of AABW changes. However, ocean global circulation models (OGCMs), such as those used for climate projections, do not yet resolve the complex set of processes involved in AABW formation and thus are not yet likely to reproduce accurately observed AABW changes.

AABW warming from heave contributes to the net ocean heat uptake. Earth is currently out of radiative balance owing to increasing atmospheric greenhouse gas concentrations. Satellite and in situ measurements show that Earth has been gaining heat at a rate of 183 TW between 1972 and 2008 (Church et al. 2011) with 90% of the excess energy being absorbed by the ocean. For comparison, the 33.8 ±13.6 TW of warming found here south of 30ºS below 2000 m (Table 4.1) amounts to about 0.07 ±0.03 W m^{-2} when calculated as a flux over the entire Earth surface. This is about 14% of the above total heat uptake.

The values of heat gain we find in the Southern Ocean are generally smaller than those of P&J (2010), and have smaller confidence intervals. Our mean heat fluxes below 4000 m in the Amundsen-Bellingshausen, Australian-Antarctic, and Weddell-Enderby basins are 0.14 ±0.04, 0.11 ±0.11, and 0.23 ±0.18 W m^{-2}, respectively. Comparable values from P&J (2010) are 0.20 ±0.14, 0.32 ±0.17, and 0.44 ±0.36 W m^{-2}, respectively. These two sets of estimates agree within confidence limits. While some data have been added for the most recent estimates, much of the difference is owing to a change in methods. We now find basin means on mean θ depths and apply them by θ to the climatological mean θ field instead of doing calculations on isobars. This new method gives smaller heat gains than P&J (2010) because the large warming in the deep southernmost waters raises the whole basin mean along an isobar, thus raising the basin total when integrated on isobars. When the rates are calculated and applied on θ, the strongest signal is contained geographically to the deep southernmost region, thus giving a more accurate, but smaller total heat flux. The 95% confidence intervals are slightly smaller here than in P&J

(2010) partly because we use more data, but mostly because the variations across the basin are smaller on mean depths of isotherms than along isobars.

Finally, both the observed heave and water-mass freshening signals in the deep Southern Ocean contribute to SLR (Table 4.1). Global mean sea level is estimated to rise at a rate of 3.2 ± 0.4 mm yr^{-1} between 1993 and 2008, with 0.7 ±0.3 mm yr^{-1} owing to thermal expansion in the upper water column and the rest owing to ice melt, terrestrial water storage changes, and deep ocean warming (Church et al. 2011). Water property changes south of 30ºS for $\theta < 0$ °C cause a local mean SRL of 0.52 ±0.18 mm yr^{-1} with almost all of this owing to changes in θ (Table 4.1). The heave component, comprised of the sum of +0.52 mm yr^{-1} SLR owing to warming and -0.08 SLR mm yr^{-1} from salinification heave (Table 4.1), accounts for a SLR of +0.44 mm yr^{-1}. The water-mass freshening causes an additional 0.09 mm yr^{-1}. Therefore, in the deep Southern Ocean, local SLR owing to AABW changes are a significant fraction of the global mean rate of SLR.

Acknowledgments:

We thank the hundreds of people who helped to collect, calibrate, process, and archive the WOCE and CLIVAR data sets, without whom global assessments of ocean variability like this one would be impossible. We also thank those who provided us with unreported SSW batch numbers for many cruises. D. Roemmich suggested an improvement for the error analysis. Finally, suggestions of two anonymous reviewers and editor Anand Gnanadesikan improved this manuscript. This work was supported by the NOAA Climate Program Office, NOAA Research, and NASA Headquarters under the NASA Earth and Space Fellowship Program - Grant NNX11AL89H.

4. 7 APPENDIX: Ad-hoc Salinity Adjustments

We attempt to correct for small intercruise salinity biases as offsets for all occupations of repeated hydrographic sections (Table 4.A1; see P&J 2012 for full data set description). We estimate these offsets by comparing S data in select geographical regions containing old, well-mixed, low-variability water, where the adjective old denotes a long time since the water was last in contact with the atmosphere. These small intercruise S biases can arise from differences in sampling, measuring, and calibration routines conducted by different personnel.

Intercruise S offsets are identified for all occupations of every section. First, each cruise is divided into subsections based on topographic and dynamic boundaries (such as fronts). Areas near boundaries, strong currents, or water-mass fronts are excluded. For each occupation at each location along a section, the S data are linearly interpolated onto to a 0.01 °C resolution θ-grid. The intercruise difference in S, ΔS, is calculated at each θ and each location along the section by subtracting the mean S of all the co-located occupations from each individual occupation. A mean (ΔS_{mean}) and variance (ΔS_{var}) are calculated for each subsection along θ surfaces. Within each subsection, a 0.1 °C-thick layer is chosen balancing where ΔS_{var} is small and the waters are oldest, as determined by examination of the chlorofluorocabon, oxygen, nitrate, and $\Delta^{14}C$ distributions for the WOCE occupation of each section using the WOCE Atlases (e.g., Orsi and Whitworth, 2005). These portions of the water column are chosen to maximize the likelihood that ΔS estimates are owing to cruise measurement biases, not physical changes. The weighted means of ΔS_{mean}, $\Delta \overline{S}_{mean}$, within the selected isotherm bands are found using the inverses of ΔS_{var} for weights. Similarly, the weighted means of ΔS_{var}, $\Delta \overline{S}_{var,}$ are found using ΔS_{var} as weights. Finally, the S offset for an entire cruise is calculated as the $\Delta \overline{S}_{\text{var}}$ weighted mean of $\Delta \overline{S}_{\text{mean}}$ (Table 4.A1).

The global array of repeated hydrographic sections collected through WOCE and GO-SHIP programs are considered here, consisting of 33 lines with a total of 146 legs collected between 1981 and 2012. SSW batches and their recommended SSW offsets (Kawano et al. 2006; T. Kawano personal comm. 2011) are noted along with the additional ad-hoc offset found here (Table 4.A1). Offsets are added to salinity data to obtain the final value. SSW batch offsets are available for 91% of the legs, with missing values either because the SSW batch used is too new for an offset to be estimated or because the SSW batch used is unknown. Additional ad-hoc offsets are found for 87% of the legs, with the missing offsets owing to the leg length being too short or the absence of a location on the section suitable to identify an offset. Of the 132 net offsets, 118 are less than the stated CTD salinity accuracy of 0.002 PSS-78, with the mean magnitude of the offsets being 0.0008 PSS-78 (Fig A1). While the application of SSW batch offsets improves the agreement among occupations of each section, it does not eliminate the need for ad-hoc offsets to reduce intercruise salinity biases (Fig. A1).

While these offsets are small, they are important for sea level rise estimates. For example, a 0.002 PSS-78 increase in S applied a 1000-m of a 0°C, 34.6 PSS-78 column of water results in a 0.14 mm decrease in SLR compared to only a 0.03 mm SLR increase from a 0.002 °C increase in temperature. In addition, the observed freshening between sequential cruises ~10 years apart, ranges from 0 to 1 order of magnitude greater than the WOCE stated salinity accuracy but 1 to 2 orders of magnitude greater than the WOCE temperature accuracy.

References

Aoki, S., S. R. Rintoul, S. Ushio, S. Watanabe, and N. L. Bindoff, 2005: Freshening of the Adélie Land Bottom Water near 140°E. *Geophys. Res. Lett.,* **32**, L23601, doi:10.1029/2005GL024246.

Church, J. A.., N. J. White, L. F. Konikow, C. M. Domingues, J. G. Cogley, E. Rignot, J. M. Gregory, M. R. van den Broeke, A. J. Monaghan, and I. Velicogna, 2011: Revisiting the Earth's sea-level and energy budgets from 1961 to 2008. *Geophys. Res. Lett.,* **38,** L18601, doi:10.1029/2001GL048794.

Coles, V. J., M. S. McCartney, D. B. Olson, and W. M. Smethie Jr., 1996: Changes in Antarctic Bottom Water properties in the western South Atlantic in the late 1980s. *J. Geophys. Res*., **101**, 8957–8970.

Bindoff, N.L., and T.J. McDougall, 1994: *Diagnosing Climate Change and Ocean Ventilation using Hydrographic Data.* Journal of Physical Oceanography, **24**, 1137-1152. ISSN 1520-0485.

Broecker, W. S., S. Sutherland, and T. H. Peng, 1999: A possible 20th-century slowdown of Southern Ocean deep water formation. *Science* **286**, 1132-1135, doi:10.1126/science.286.5442.1132.

Fahrbach, E., M. Hoppema, G. Rohardt, M. Schroder, and A. Wisotzki, 2004: Decadal-scale variations of water mass properties in the deep Weddell Sea. *Ocean Dynamics*, **54**, 77–91.

Fahrbach E., M. Hoppema, G. Rohardt, O. Boebel, O. Klatt, and A. Wisotzki, 2011: Warming of deep and abyssal water masses along the Greenwich meridian on decadal time scales: The Weddell gyre as a beat buffer. *Deep-Sea Res. II,* **58**, 2508–2523, doi:10.1016/j.dsr2.2011.06.007.

Foster, T. D., and Carmack, E. C., 1976: Frontal zone mixing and Antarctic Bottom Water formation in the southern Weddell Sea. *Deep-Sea Res.*, **23**, 301–317.

Fukasawa, M., H. Freeland, R. Perkins, T. Watanabe, H. Uchida, and A. Nishima, 2004: Bottom water warming in the North Pacific Ocean. *Nature*, **427**, 825–827.

Gille, S. T., 2008: Decadal-scale temperature trends in the Southern Hemisphere ocean. *J. Climate*, **21**, 4749–4765.

Gordon, A. L., 1972: Spreading of Antarctic Bottom Waters, II In: *Studies in Physical Oceanography - A Tribute to George Wust on His 80th Birthday*. A.L. Gordon (ed), Gordon and Breach, Science Publ., N.Y.: 1-17.

Gordon A. L., B. Huber, D. McKee, and M. Visbeck, 2010; A Seasonal cycle in the export of bottom water from the Weddell Sea. *Nature Geoscience*, **3**, 551-556, doi:10.1038/ngeo916.

Gouretski, V. V., and K. P. Koltermann, 2004: *WOCE Global Hydrographic Climatology.* Berichte des bundesamtes für seeshifffahrt und hydrographie, 35, pp. 52+2 CD-ROMs.

Jacobs, S. S., 2004: Bottom water production and its links with the thermohaline circulation. *Antarctic Science*., **4**,427-437, doi:10.1017/S095410200400224X.

Jacobs, S. S., and C. F. Giulivi, 2010: Large multi-decadal salinity trends near the Pacific-Antarctic Continental Margin. *J. Climate***,** **23**, 4508–4524, doi:10.1175/2010JCLI3284.1.

Johnson, G. C., 2008: Quantifying Antarctic Bottom Water and North Atlantic Deep Water volumes. *J. Geophys. Res*., **113**, C05027, doi:10.1029/2007JC004477.

Johnson, G. C., and S. C. Doney, 2006: Recent western South Atlantic bottom water warming. *Geophys. Res. Lett*., **33**, L14614, doi:10.1029/2006GL026769.

Johnson, G. C., S. Mecking, B. M. Sloyan, and S. E. Wijffels, 2007: Recent bottom water warming in the Pacific Ocean. *J. Climate*, **20**, 5365–5375.

Johnson, G. C., S. G. Purkey, and J. L. Bullister, 2008: Warming and freshening in the abyssal southeastern Indian Ocean. *J. Climate*, **21**, 5353–5365.

Joyce, T. M., 1991: Introduction to the collection of expert reports compiled for the WHP Program. WOCE Hydrographic operations and methods. WOCE Operations Manual. WHP Office Report WHPO-91-1, WOCE Report 68/91.

Kawano, T., M. Aoyama, T. Joyce, H. Uchida, Y. Takatsuki, and M. Fukasawa, 2006: The latest batch-to-batch difference table of standard seawater and its application to the WOCE onetime sections. *J. Oceanogr.,* **62**, 777-792.

Kawano, T., T. Doi, H. Uchida, S. Kouketsu, M. Fukasawa, Y. Kawai, and K. Katsumata, 2010: Heat content change in the Pacific Ocean between the 1990s and 2000s. *Deep-Sea Res. II,* **57**, 1141–1151, doi:10.1016/j.dsr2.2009.12.003.

Kouketsu, S., and Coauthors, 2011: Deep ocean heat content changes estimated from observation and reanalysis product and their influence on sea level change. *J. Geophys. Res.*, **116**, C03012, doi:10.1029/2010JC006464.

Lumpkin, R., and K. Speer, 2007, Global ocean meridional overturning. *J. Phys. Oceanogr.,* **37**, 2550–2562.

Lynch-Stieglitz, J., and Coauthors, 2007: Atlantic meridional overturning circulation during the last glacial maximum. *Science,* **316**, 66–69, doi:10.1126/science.1137127.

Masuda, S., and Coauthors, 2010: Simulated rapid warming of abyssal North Pacific water. *Science*, **329**, 319–322, doi:10.1126/science.1188703.

McDonagh E. L., H. L. Bryden, B. A. King, R. J. Sanders, S. A. Cunningham, and R. Marsh, 2005: Decadal changes in the south Indian Ocean thermocline. *J. Climate*, **18**, 1575-1590.

Meredith, M. P., A. C. Naveira Garabato, A. L. Gordon, and G. C. Johnson, 2008: Evolution of the deep and bottom water of the Scotia Sea, Southern Ocean, during 1995–2005. *J. Climate*, **21**, 3327–3343.

Orsi., A. H. , T. Whitworth II, Hydrographic Atlas of the World Ocean Circulation Experiment (WOCE). Volume 1: Southern Ocean (eds. M. Sparrow. P. Chapman and J. Gould), International WOCE Project Office, Southampton, U.K., ISBN 0 904175-49-9. 2005.

Orsi, A. H., G. C. Johnson, and J. L. Bullister, 1999: Circulation, mixing and production of Antarctic Bottom Water. *Prog. Oceanogr.*, **43**, 55–109.

Purkey, S. G., and G. C. Johnson, 2010, Warming of global abyssal and deep Southern Ocean waters between the 1990s and 2000s: Contributions to global heat and sea level rise budgets. *J. Climate*, **23**, 6336–6351. doi:10.1175/2010JCLI3682.1.

Purkey, S. G. and G. C. Johnson, 2012: Global contraction of Antarctic Bottom Water between 1980s and 2000s. *J. Climate*, **25**, 5830–5844. doi:10.1175/JCLI-D-11-00612.1

Rignot, E., J. L. Bamber, M. R. van Den Broeke, C. Davis, Y. Li, W. Jan Van De Berg, and E. van Meijgaard, 2008: Recent Antarctic ice mass loss from radar interferometry and regional climate modeling. *Nature Geoscience*, **1,** 106–110, doi:10.1038/ngeo102.

Rignot E., and S. S. Jacobs, 2002: Rapid bottom melting widespread near Antarctic ice sheet grounding lines. *Science*, **296**, 2020-2023, doi:10.1126/science.1070942.

Rintoul, S. R., 2007: Rapid freshening of Antarctic Bottom Water formed in the Indian and Pacific oceans. *Geophys. Res. Lett.*, **34**, L06606, doi:10.1029/2006GL028550.

Robertson R., M. Visbeck, A. L. Gordon, and E. Fahrbach, 2002: Long-term temperature trends in the deep waters of the Weddell Sea. *Deep-Sea Res. II*, **49**, 4791–4806.

Roemmich, D., G. C. Johnson, S. Riser, R. Davis, J. Gilson, W. B. Owens, S. L. Garzoli, C. Schmid, and M. Ignaszewski. 2009. The Argo Program: Observing the global oceans with profiling floats. *Oceanography*, **22(2)**, 34-43.

Shepherd, A., D. J. Wingham, and J. A. D. Mansley, 2002: Inland thinning of the Amundsen Sea sector, West Antartica. *Geophys. Res. Lett*, **29**, doi:10.1029/2001GL014183.

Shepherd, A., D. Wingham, and E. Rignot, 2004: Warm ocean is eroding West Antarctic Ice Sheet. *Geophys. Res. Lett*, **31**, L23402, doi:10.1029/2004GL021106.

Shimada, K., S. Aoki, K. I. Ohshima, and S. R. Rintoul, 2012: Influence of Ross Sea Bottom Water changes on the warming and freshening of the Antarctic Bottom Water in the Australian-Antarctic Basin. *Ocean Sci.*, **8**, 419-432, doi: 10.5194/os-8-419-2012.

Swift J. H., and A. H. Orsi, 2012: Sixty-four days of hydrography and storms: RVIB Nathaniel B. Palmer's 2011 S04P Cruise. *Oceanography*, **25(3)**, 54-55, doi:10.5670/oceanog.2012.74.

Whitworth, T., III, 2002: Two modes of bottom water in the Australian-Antarctic Basin, *Geophys. Res. Lett.*, **29**, 1073, doi:10.1029/2001GL014282.

Zenk, W., and E. Morozov, 2007: Decadal warming of the coldest Antarctic Bottom Water flow through the Vema Channel. *Geophys. Res. Lett.*, **34**, L14607, doi:10.1029/2007GJ030340.

Table 4.1: Fresh water gain (FW; Gt yr^{-1}), Sea Level Rise (SLR; mm yr^{-1}) and heat uptake (TW) with uncertainties at the 95 % confidence level below θ = 0 °C, 4000 m, and 2000m in the Amundsen-Bellingshausen Basin (ABB), Australian-Antarctic Basin (AAB), Weddell-Enderby Basin (WEB), and the whole Southern Ocean south of 30°S (Fig. 4.1). Freshwater estimates are calculated following (1) using basin mean freshening trends owing to only water-mass changes. Steric SLR trends are estimated from (3) broken into water-mass, heave, total salinity, and warming trends. The total steric SLR is also given. Heat uptake is calculated following (2) using basin mean warming trends. Values statistically different from zero at the 95% confidence are given in bold.

		FW (Gt yr^{-1})	SLR (mm yr^{-1})					Heat (TW
		Water-mass	Water-mass	Heave	Salinity	θ	Total	θ
Below 0 C	ABB	**25 ±9**	**0.17 ±0.06**	0.00 ±0.02	**0.18 ±0.07**	**0.31 ±0.10**	**0.49 ±0.13**	**1.0 ±0.3**
	AAB	**48 ±36**	**0.22 ±0.16**	**-0.07 ±0.05**	0.15 ±0.18	**0.5 ±0.28**	**0.65 ±0.33**	**2.5 ±1.4**
	WEB	24 ±54	0.05 ±0.11	-0.12 ±0.12	-0.07 ±0.12	**0.66 ±0.45**	**0.59 ±0.46**	**7.7 ±5.3**
	Total S of 30S	**99 ±56**	**0.09 ±0.05**	**-0.08 ±0.04**	0.00 ±0.06	**0.52 ±0.17**	**0.52 ±0.18**	**14 ±5**
Below 4000m	ABB	**9 ±4**	**0.03 ±0.01**	-0.01 ±0.01	**0.02 ±0.02**	**0.18 ±0.06**	**0.20 ±0.06**	**1.1 ±0.3**
	AAB	**17 ±13**	**0.12 ±0.1**	-0.02 ±0.03	**0.11 ±0.1**	**0.14 ±0.13**	**0.25 ±0.17**	**0.4 ±0.4**
	WEB	10 ±28	0.03 ±0.09	-0.05 ±0.08	-0.02 ±0.05	**0.30 ±0.23**	**0.28 ±0.24**	**1.9 ±1.5**
	Total S of 30S	**53 ±21**	**0.02 ±0.01**	**-0.02 ±0.01**	0.01 ±0.01	**0.13 ±0.05**	**0.14 ±0.05**	**5 ±2**
Below 2000m	ABB	-28 ±43	-0.05 ±0.08	0.02 ±0.07	-0.03 ±0.08	**0.44 ±0.26**	**0.41 ±0.27**	**5.7 ±3.4**
	AAB	48 ±66	0.15 ±0.2	-0.12 ±0.21	0.03 ±0.29	**1.03 ±0.83**	**1.06 ±0.89**	**8.1 ±6.1**
	WEB	27 ±81	0.06 ±0.17	-0.13 ±0.19	-0.07 ±0.2	0.70 ±0.70	0.63 ±0.73	**7.8 ±8.0**
	Total S of 30S	**-454 ±241**	**-0.12 ±0.06**	**0.09 ±0.07**	-0.03 ±0.06	**0.37 ±0.15**	**0.34 ±0.16**	**34 ±14**

Table 4.A1: IAPSO Standard Sea Water (SSW) batch number with recommended SSW batch salinity offset (Kawano et al. 2006; T. Kawano personal communication 2011) for each leg listed by WOCE ID (with alternative ID used on http://cchdo.ucsd.edu in parentheses if different) and year. If more than one leg of a section is occupied per year, legs are differentiated by geographical region (East (E), West (W), North (N), South (S), Central (C), or Antarctic (A)) or, if an exact repeat of a leg is done twice in one year, then legs are listed chronologically by the date of the first station occupied. If no SSW batch number is listed, we were unable to determine this information from cruise reports or through personal queries to data originators. As of September 2012, there is no known offset for batch numbers P113 and P152, therefore no SSW batch offset is applied for cruises using those SSW batches. The last column lists the additional ad-hoc salinity offsets estimated by and applied for our analyses (see Appendix). If legs do not have an ad-hoc salinity offset listed, then one was not possible to estimate owing to the section location or length. Both offsets are added to salinity data.

WOCE ID	yr	ssw batch number	ssw offset (x1000)	ad-hoc offsets (x1000)
A01(AR07)E	1990	P112	1.9	0.186
A01(AR07)W	1990	P104	1.1	N/A
A01(AR07)E	1991	P112/P114	1.9/2	N/A
A01E	1991	P112	1.9	-0.289
A01(AR07)E	1992	P119	0	-0.836
A01(AR07)W	1992	P112	1.9	N/A
A01(AR07)W	1993	P117	N/A	N/A
A01(AR07)E	1994	N/A	N/A	N/A
A01(AR07)W	1994	P123	0.7	N/A
A01W	1994	P124	0.6	-0.496
A01(AR07)E	1995	N/A	N/A	-0.551
A01W	1995	P126	0.6	N/A
A01(AR07)E	1996	N/A	N/A	1.870
A01(AR07)W	1996	P124	0.6	N/A
A01(AR07)E	1997	P129	0.4	N/A
A01(AR07)W	1997	P129	0.4	N/A
A01(AR07)W	1998	P133	0.3	N/A
A02	1994	P124	0.6	-1.849
A02	1997	P129	0.4	1.849

A05	1981	P93	0.9	-2.867
A05	1992	P120	-0.9	0.114
A05(AR01)	1998	P125	0.2	0.259
A05	2004	P143/P144	-0.2/-0.5	1.028
A05	2010	N/A	N/A	1.952
A10	1992	P120	-0.9	-1.110
A10	2003	P142	0.2	0.134
A10	2011	P152	N/A	0.829
A12	1992	P114	2	-0.553
A12(S04)	1996	P127	0.8	0.437
A12	1999	P134	0.3	-0.038
A12	2000	P135	0.2	0.624
A12	2002	P140	-0.3	-0.034
A12	2005	P144	-0.5	0.273
A13.5	1983	P92	-0.2	-1.276
A13.5	2010	P147	-0.5	1.276
A16N	1988	P108	1.7	0.587
A16C	1989	P108	1.7	-0.494
A16S	1989	P108	1.7	0.435
A16	1993	P119	0	-0.869
A16(A23)	1995	P125	0.2	0.332
A16(AR21)	1998	P133	0.3	0.166
A16	2003	P143	-0.2	-0.384
A16	2005	P143	-0.2	0.087
A16	2011	N/A	N/A	2.276
A20	1997	P131	0.1	-1.446
A20	2003	P140	-0.3	1.446
A22	1997	P131	0.1	-0.283
A22	2003	P140	-0.3	0.283
I02	1995	P128	1.4	0.246
I02	2000	P133/P138	0.3/-0.1	-0.246
I03	1995	P126	0.6	0.328
I03	2003	P142	0.2	-0.328
I04	1995	P126	0.6	-0.274
I04	2003	P142	0.2	0.274
I05	1987	P97	2.1	-1.406
I05W	1995	P126	0.6	0.836
I05E	1995	P126	0.6	0.449
I05	2002	P140	-0.3	1.031
I05	2009	P149	0.8	0.234
I06	1993	P121	0.4	-0.264
I06	1996	N/A	N/A	-0.042
I06	2008	N/A	N/A	0.186
I08S	1994	P124	0.6	-0.802
I08(I09N)N	1995	P126	0.6	0.479
I08	2000	P133/P138	0.3/-0.1	-0.564
I08(I09N)N	2007	P147	-0.5	0.206

I08S	2007	P147	-0.5	0.802
I09	1995	P124	0.6	-0.338
I09(S03)S	1995	P121/P123	0.4/0.7	N/A
I09	2004	P141	-0.3	0.338
IR6	1995	N/A	N/A	0.597
IR6	1995	N/A	N/A	0.828
IR6(I02)	2000	P133/P138	0.3/-0.1	-1.339
P01	1985	P96	2.5	1.154
P01C	1999	P135	0.2	-0.680
P01E	1999	P133/P134	0.3/0.3	0.386
P01H	1999	P135	0.2	N/A
P01W	1999	P133	0.3	-0.849
P01C	2007	P148	0.2	-0.304
P01W/E/H	2007	P148	0.2	-0.651
P02	1985	P96	2.5	0.956
P02E	1993	P123	0.7	1.175
P02	1994	P144	-0.5	-1.968
P02C	1994	P121	0.4	-2.600
P02W	1994	P144	-0.5	4.534
P02	2004	P144	-0.5	0.274
P03	1985	P96	2.5	1.764
P03E	2005	P145	-0.8	-1.553
P03W	2005	P145	-0.8	-2.009
P03	2006	P145	-0.8	N/A
P06C	1992	P116	1.4	-1.205
P06E	1992	P116	1.4	0.357
P06W	1992	P116	1.4	-1.167
P06W	2003	P142	0.2	0.358
P06E	2003	P142	0.2	-0.837
P06	2009	N/A	N/A	0.866
P09	1994	P123	0.7	-0.200
P09	2010	P152	N/A	0.200
P10	1993	P114/P120	2/-0.9	0.323
P10	2005	P145	-0.8	-0.323
P14	1992	P120	-0.9	0.087
P14	1993	P122	0.4	0.571
P14N	2007	P148	0.2	-0.777
P14S	2007	P148	0.2	-0.376
P15	1996	P114	2	-1.304
P15	2001	P140	-0.3	0.840
P15	2009	P148/P150	0.2/0.8	0.490
P16	1984	P92	-0.2	2.901
P16C	1991	P114	2	0.932
P16N	1991	P110	1.9	-1.431
P16S	1991	P108/P114	1.7/2	0.010
P16A	1992	P120	-0.9	0.222
P16S	2005	P144	-0.5	-0.319

P16N	2006	P145	-0.8	-1.141
P17S	1991	P108/P114	1.7/2	-0.512
P17C	1991	P120	-0.9	2.470
P17A	1992	P120	-0.9	0.460
P17N	1993	P122	0.4	0.915
P17	2001	P139	0.4	-1.754
P18S	1994	P114	2	-0.209
P18N	1994	P114	2	0.335
P18(AAIW)	2006	P146	-1.2	N/A
P18N	2007	P147	-0.5	-0.483
P18S	2008	P147	-0.5	0.209
P21W	1994	P123	0.7	-0.447
P21E	1994	P123	0.7	-0.240
P21	2009	P150	0.8	0.396
S01	1993	N/A	N/A	N/A
S01	1994	N/A	N/A	N/A
S01	1996	N/A	N/A	N/A
SR03	1991	P115	2.5	N/A
SR03	1993	P121	0.4	-5.643
SR03	1994	P121/P123/P137/P140	0.4/0.7/-0.4/-0.3	0.206
SR03(S03)	1995	P121/P123	0.4/0.7	-0.997
SR03	1995	P128/P130	1.4/0.3	3.454
SR03	1996	P128/P130	1.4/0.3	1.606
SR03	2001	P113/P133/P137/P140	N/A/0.3/-0.4/-0.3	1.385
SR03	2008	P140/P147/P148	-0.3/-0.5/0.2	0.884
S04	1989	P111	2.1	-0.703
S04	1990	P113	N/A	1.523
S04	1992	N/A	N/A	0.667
S04	1996	P127/P148	0.8/0.2	-1.893
S04	1998	P113	N/A	0.995
S04	2005	P144	-0.5	-0.716
S4P	1992	P108	1.7	0.059
S4P	2011	P152	N/A	-0.059

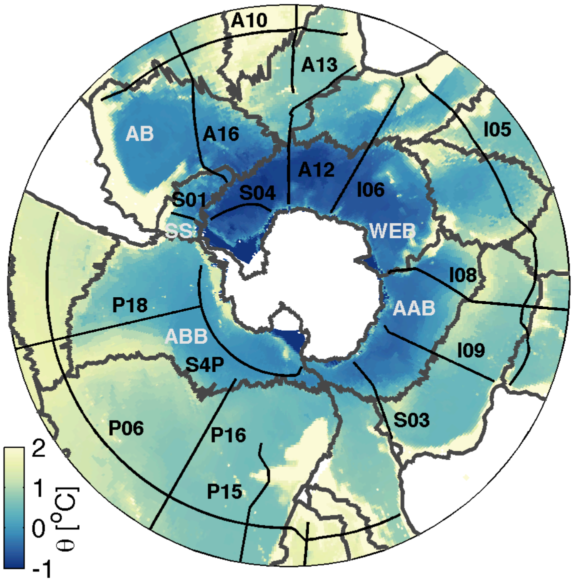

Figure 4.1. Southern Ocean section locations (black lines) labeled with WOCE IDs (black characters) and basin boundaries (gray lines) over bottom potential temperature (color shading; Gourstski and Koltermann 2004) with land (white shading). Basin names (white characters) are indicated by abbreviations including: Weddell-Enderby Basin (WEB), Australian-Antarctic Basin (AAB), Amundsen-Bellingshausen Basin (ABB), Scotia Sea (SS), and the Argentine Basin (AB).

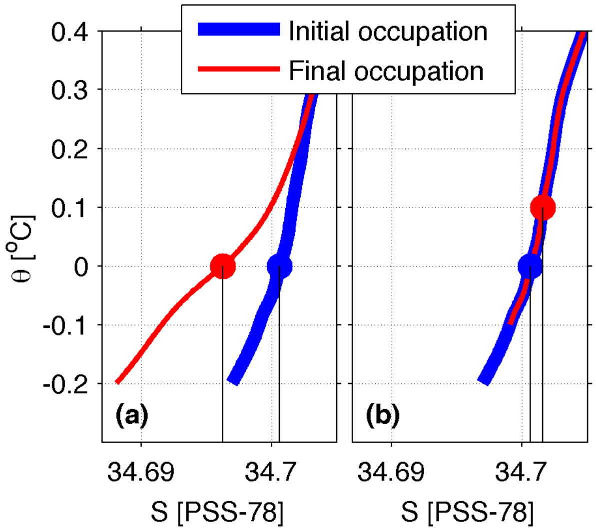

Figure 4.2: Schematics of changes in salinity between an initial (blue) and final (red) occupation of a given station owing to (a) water-mass change and (b) isotherm heave. Water-mass changes (a) can be seen as a change in the θ-S curve causing a deep freshening signal between occupations (black lines) at the same depths (dots). Isotherm heave (b), caused by a vertical displacement of potential isotherms, causes water at the same depth (dots) to warm and become more saline between occupations (black lines).

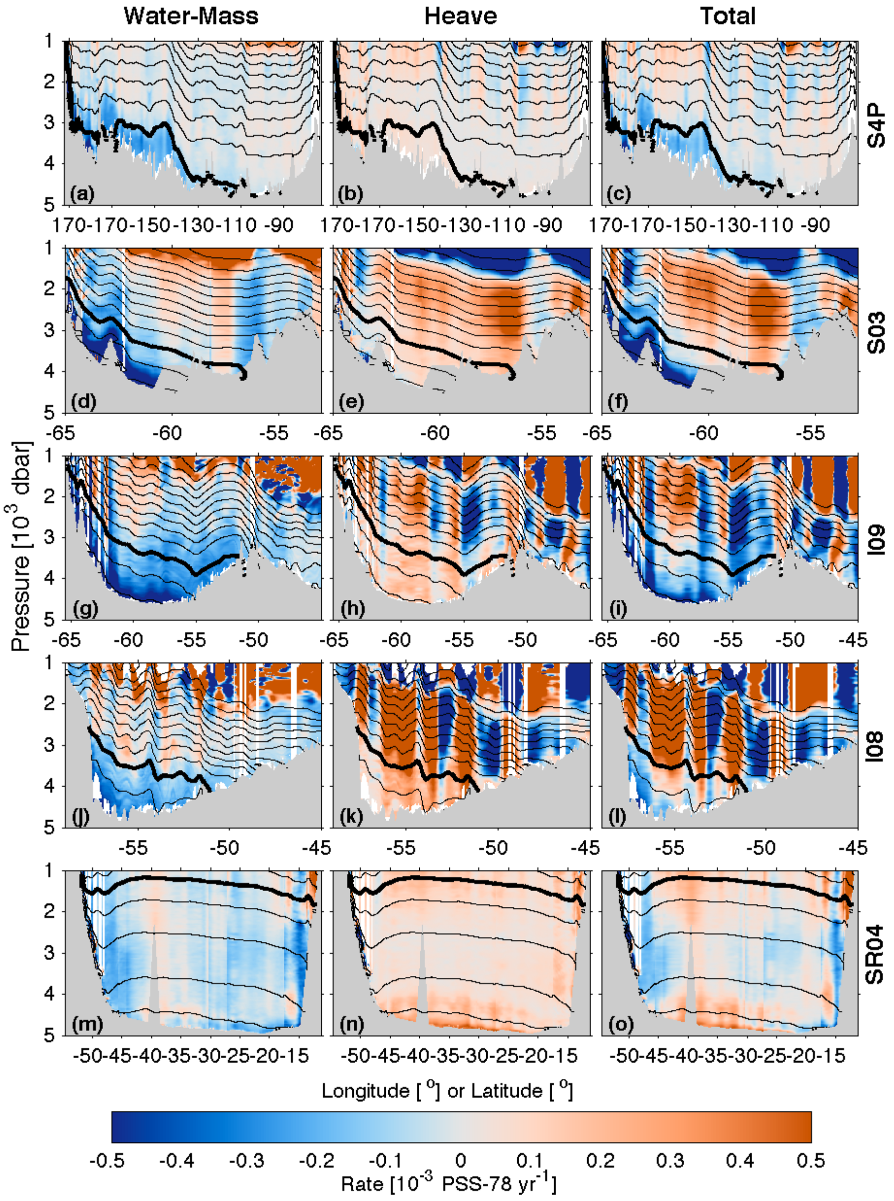

Figure 4.3. Rate of change in S (color; in PSS-78 yr^{-1}) vs. pressure and latitude or longitude along S4P (a-c), S03 (d-f) across the Australian-Antarctic Basin, I09 (g-i) across the Australian-Antarctic Basin, I08 (j-l) across the Australian-Antarctic Basin, and SR04 (m-o) across the Weddell Sea (see Fig.1 for locations). Orange indicates areas of salinification and blue areas of freshening with mean isotherms contoured at 0.2 °C intervals (thin black lines; 0°C isotherm thick black line). The water mass (a, d, g, j, m) and heave (b,e,h,k,n) contributions to the total (c,f,i,l,o) are separated.

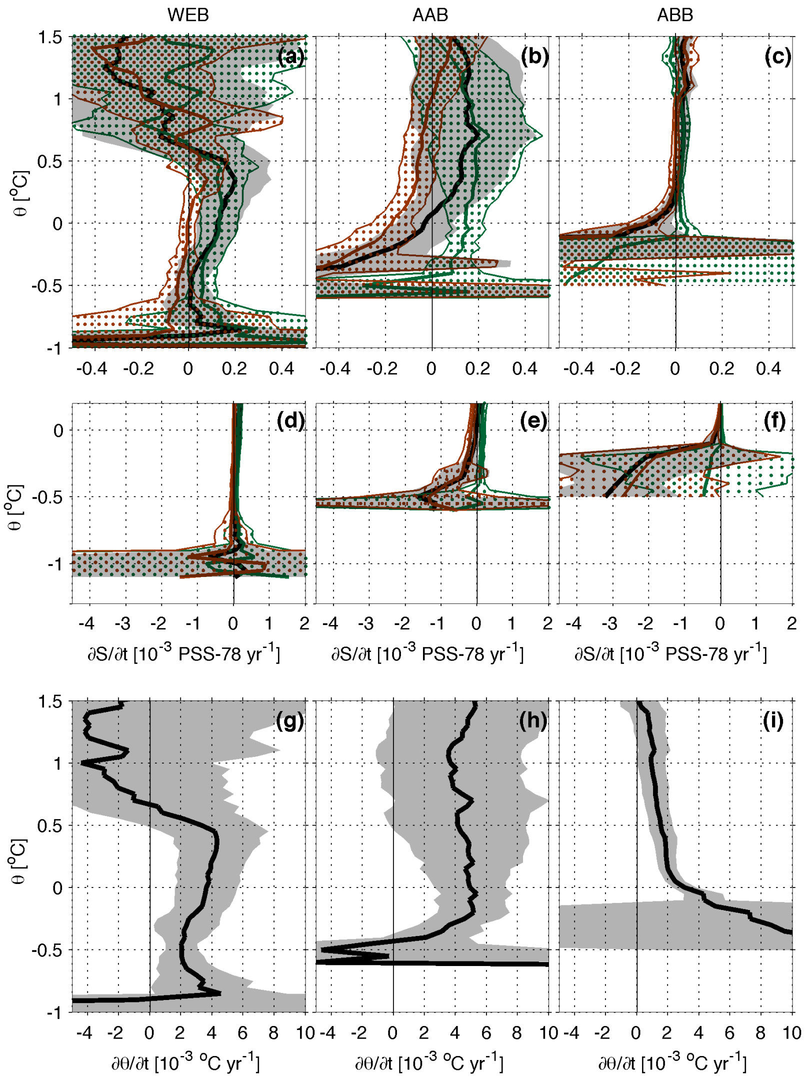

Figure 4.4: Basin-mean rates of change in S (black; a–f; PSS-78 yr^{-1}) and θ (black g–I; °C yr^{-1}) with 95% confidence intervals (gray shading) estimated along time-mean θ surfaces in the Weddell-Enderby Basin (WEB), Australian-Antarctic Basin (AAB) and Amundsen-Bellingshausen Basin (ABB). The water-mass (red) and heave (green) contributions to the total with 95% confidence intervals (dots) are shown over a large θ range to show interior changes (a-c) as well as vertically expanded over a limited θ range (d-f) to show large changes found in the coldest waters along the continental slope (see Fig 3).

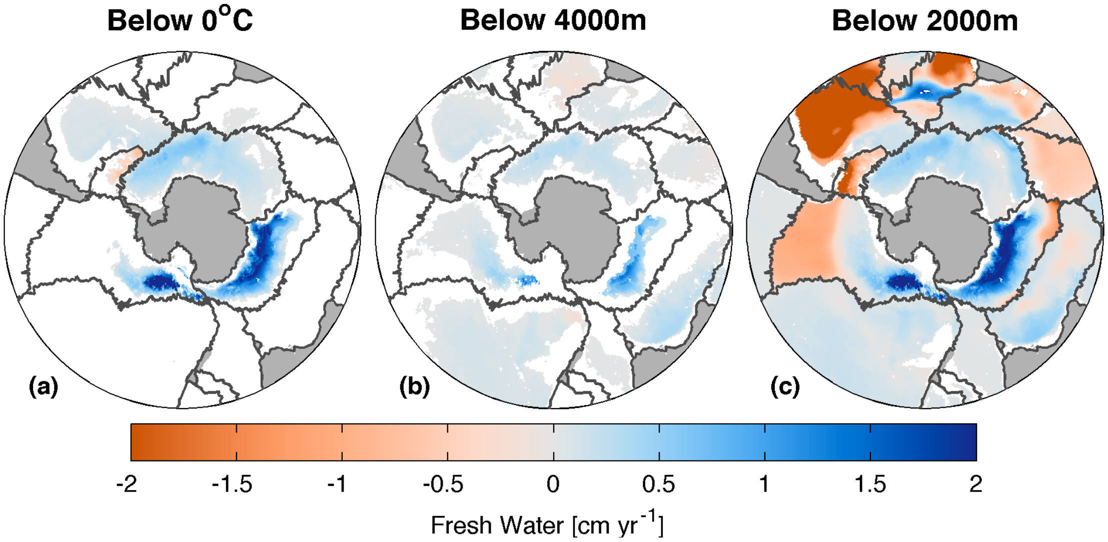

Figure 4.5. Local vertical column freshwater fluxes in cm yr^{-1} (color) below (a) 0°C, (b) 4000 m, and (c) 2000 m equivalent to observed water-mass salinity changes. Basin boundaries (gray lines) and land (gray shading) are shown.

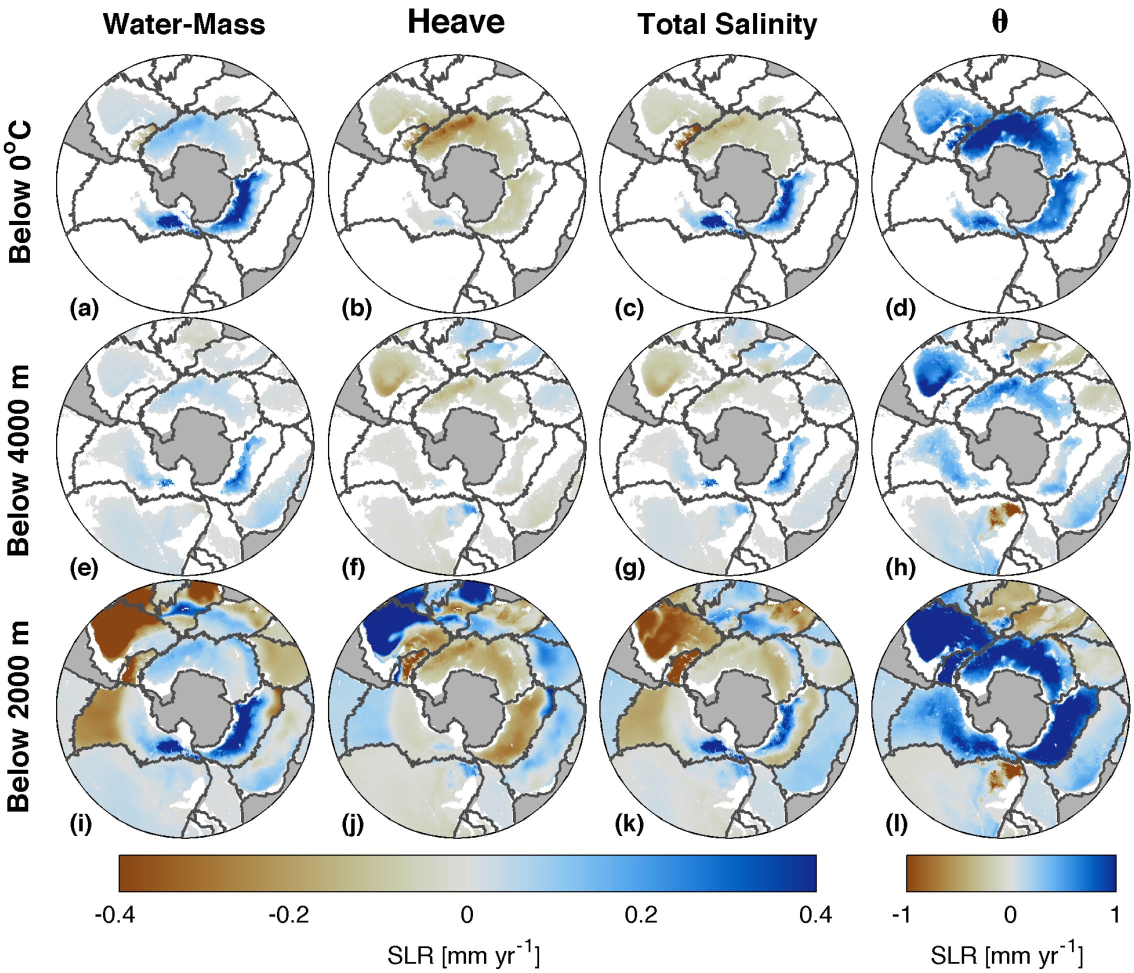

Figure 4.6: Vertical column total sea level rise [mm yr^{-1}] below θ = 0°C (a–d), 4000 m (e–h), and 2000 m (i–l) owing to water-mass S changes (a,e,i), heave salinity changes (b,f,j), net salinity changes (c,g,k), and θ changes (d,h,l). Blue indicates areas of positive SLR and brown of negative SLR (see color legends). SLR is calculated based on basin (gray lines) mean rates of change in S and θ (e.g. Figure 4) along climatological isotherms (see Section 4).

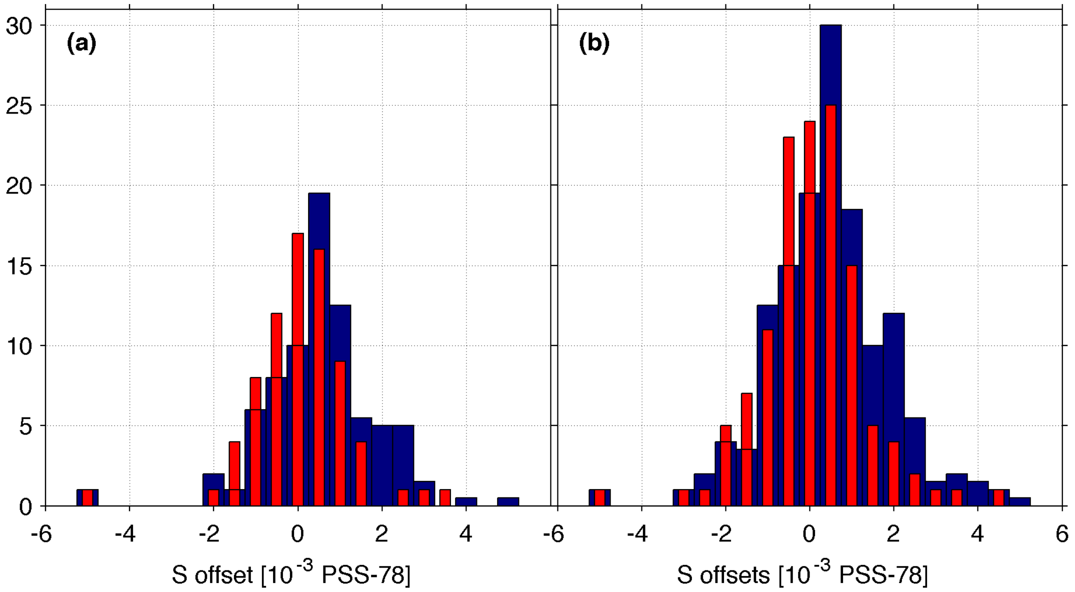

Figure 5.A1: Histogram of estimated ad-hoc salinity offsets (red) and the sum of recommended SSW batch and ad-hoc salinity offsets (blue) applied to the CTD data along hydrographic legs in the (a) Southern Ocean and (b) Global Ocean (Table 4.A1). If a leg had more than one SSW batch offset, each offset is given an equal weight in computing a mean.

Chapter 5

Relative Contributions of Ocean Mass and Deep Steric Changes to Sea Level Rise Between 1993 and 2013

(CITE: Purkey, S. G., G. C. Johnson and D. Chambers, 2014: Relative contributions of ocean mass and deep steric changes to sea level rise between 1993 and 2013. J. of Geophysical Research, submitted.)

Abstract

Regional and global rates of Sea Level Rise (SLR) owing to mass addition are assessed using full-depth ocean and satellite measurements taken between October 1992 and 2013. First, differences in total sea level from satellite altimetry and the steric expansion contribution to SLR between repeated occupations of full-depth in-situ oceanographic sections of temperature and salinity yield estimates of rates of mass addition as residuals. Second, regional trends in mass addition are estimated directly using data from the Gravity Recovery and Climate Experiment (GRACE) from 2003–2013 for comparison. These two independent methods both find higher rates of mass addition in the North Pacific, South Atlantic, and the Indo-Atlantic Sector of the Southern Ocean, with smaller mass addition rates in the Indian, North Atlantic, South Pacific, and the Pacific Sector of the Southern Ocean. Furthermore, rates of global mean mass addition from the two methods agree well, with 1.5 (±0.4) mm yr^{-1} from 1996–2006 found using the residual method and 1.5 (±0.4) mm yr^{-1} from 2003–2013 using the GRACE method. Finally, the relative contributions of steric contributions in the subsurface ocean below 300 m are examined by repeating the

residual method using only upper portions of the steric contribution to SLR. The subsurface ocean steric expansion is found to contribute rates of 0.78, 0.40, 0.36, 0.07, 0.06, and 0.05 mm yr^{-1} from 1996–2006 between 300–700 m, 700–1000 m, 1000–2000 m, 2000–3000 m, 3000–4000 m, and 4000–6000 m, respectively.

5.1 Introduction

Global mean sea level has risen at a rate of 3.2 (±0.4) mm yr^{-1} from 1993–2010, reflecting the sum of steric expansion from anthropogenic warming and increased ocean mass from changes in land-ocean water balance [e.g., *Leuliette et al.*, 2004; *Ablain et al.*, 2009; *Church and White*, 2011; *Church et al.*, 2013]. However, Sea Level Rise (SLR) is not uniform, with some coastal communities experiencing rates three times the global average [e.g., *Nerem et al.*, 2010; *Church et al.*, 2013], while other locations have seen little rise over this time period. A better understanding of the past trends in total SLR and the contributions from mass addition and steric expansion is needed in order to predict accurately future local and global SLR. Here we present regional and global trends in the rate of ocean mass addition using two independent methods. First we calculate differences between the changes in total sea level from satellite altimetry and in-situ steric expansion from full-depth repeat oceanographic sections, hereafter *the residual method*. Second, we estimate trends in equivalent water thickness from ocean bottom pressure (OBP) changes measured by the Gravity Recovery and Climate Experiment (GRACE) twin satellites from 2003–2013 for comparison, hereafter *the GRACE method*. In addition, we use the residual method to examine the relative contributions of warming and freshening to the SLR budget by depth between the surface and 6000 m.

Steric expansion is estimated globally to be adding 0.88 (±0.33) mm yr^{-1} from 1993–2008, with slightly slower rates into the 2010s [e.g., *Cazenave et al.*, 2009; *Church et al.*, 2011; 2013; *Levitus et al.*, 2012; *Rhein et al.*, 2013]. In the global mean, most of the steric contribution is from anthropogenic warming, with freshening having little net effect [*Lowe and Gregory*, 2006]. The upper ocean has expanded the fastest, with warming between the surface and 700 m contributing an estimated 0.7 mm yr^{-1} from 1993–2008 to global sea level rise, and the portion between 700 and 3000 m contributing an additional ~0.1 mm yr^{-1} [e.g., *Church et al.*, 2011; 2013]. Below 2000 m, the oceans are primarily filled by deep convection in the North Atlantic and by dense plumes cascading down select portions of the Antarctic continental slope. Regions ventilated by the southern sources have been warming between the 1990s and 2000s, contributing an additional 0.11 (±0.10) mm yr^{-1} to global SLR rates [*Purkey and Johnson*, 2010]. The North Atlantic below 2000 m, on the other hand, has shown decadal oscillation and with a slightly cooling trend since the mid-1970s [e.g., *Mauritzen et al.*, 2012].

Global mean sea level changes owing to increases in ocean mass can be monitored directly from changes in OBP or from the sum in changes of land storage, through monitoring of glacial retreat, melting polar ice sheets, and changes in terrestrial water storage. Global OBP changes, estimated from small fluctuations in Earth's gravitational field by the GRACE twin satellites, suggest an increase in global ocean mass at a rate of 1.8 (±0.5) mm yr^{-1} from 2003–2012, accounting for both internal variability and uncertainty in the Glacial Isostatic Adjustment (GIA) [*Chambers*, 2009; *Chambers et al.*, 2010; *Johnson and Chambers*, 2013]. This result is in good agreement with estimates in changes in land freshwater storage owning to glacier retreat, polar ice sheets loss and anthropogenic freshwater storage of 1.66 (±0.73) mm yr^{-1} between 1993–2008, despite the difference in time periods [*Church et al.*, 2011]. Glaciers have been retreating around the world, adding freshwater to the ocean at an estimated rate of 259 (±28) Gigatons yr^{-1} from 2003–2009 [*Gardner et al.*, 2013]. *Shepherd et al.* [2012] compile previous ice sheet mass studies to find the polar ice sheets have been melting at a rate of 213 Gigatons yr^{-1} from 1992–2011, with about 1/3 from Antarctic and 2/3 from Greenland. In addition, changes in groundwater extraction and reservoir retention have contributed -0.08 (±0.19) mm yr^{-1} [*Church et al.*, 2011].

Since the start of GRACE in 2003, agreement between global mean total sea level and the sum of steric and mass contributions has progressively improved while error bars have shrunk [e.g., *Lombard et al.*, 2005; *Domingues et al.*, 2008; *Willis et al.*, 2008; *Ablain et al.*, 2009; *Cazenave et al.*, 2009; *Leuliette and Miller*, 2009; *Chambers and Willis*, 2010; *Leuliette and Willis*, 2011; *Rhein et al.*, 2013]. These advances have come from improvements in understanding of the GIA, instrumentation biases, and instrumentation errors [e.g. *Willis et al.* 2008; *Leuliette and Miller*; 2009; *Chamber and Bonin*, 2012;]. Changes in ocean circulation, mostly coupled with large-scale changes in winds, do lead to large variations in regional trends in sea level [e.g., *Merrifield et al.*, 2012]. These variations are mostly associated with steric variations reflecting redistribution of heat and salt within the ocean [*Fukumori and Wang*, 2013]. However, the ocean mass distribution also varies temporally and spatially, albeit with smaller magnitudes [*Johnson and Chambers*, 2013], contributing to regional variations in sea level.

Here we present new full-depth regional and global sea level budgets between October 1992 and 2013. First, we estimate average mass addition trends within seven geographical ocean regions (Fig. 5.1) using the residual between steric sea level, from repeated full-depth in situ temperature and salinity data, and total sea surface height (SSH), from satellite altimetry (Section 3). Next we compute ocean mass trends using GRACE data from 2003–2013 for each ocean region (Section 4). We then compare the findings from both methods (Section 5). We further provide direct estimates of the relative contributions of the subsurface ocean regionally and globally from the surface to 300, 700, 1000, 2000, 3000, 4000, and 6000 m, estimating biases introduced into SLR budgets by excluding steric changes below these different depths (Section 6). We conclude with a discussion and summary (Section 7).

5.2 Data

We use four global data products to compute the ocean mass component of sea level in seven regions and globally. The residual method uses in situ full-depth ship-based oceanographic data (Section 2.1), mapped AVISO satellite altimetry (Section 2.2), and mapped monthly ocean bottom pressure from GRACE (Section 2.3) to calculate decadal ocean mass trends from the residual between total sea level and steric sea level trends, accounting for average seasonal mass redistributions. The GRACE method calculates ocean mass trends from regional monthly time-series of ocean bottom pressure produced using averaging kernels (Section 2.4).

5.2.1 In situ full-depth oceanographic data

Steric sea level is computed using full-depth, high-quality, conductivity-temperature-depth (CTD) profiles collected nominally every 55 km along ocean sections occupied two or more times between October 1992 and 2013 (Fig 5.1). Since the end of the

World Ocean Circulation Experiment (WOCE) around the turn of the century, these occupations are part of the international Global Ocean Ship-based Hydrographic Investigation Program (GO-SHIP). The data used here were publically available as of September 2013 at http://cchdo.ucsd.udu.

A full description of the data quality and intercruise salinity adjustments are given in *Purkey and Johnson* [2013], and only two differences apply here. First, in this study we use only data collected after the start of AVISO altimetry mapped products on October of 1992. The elimination of the earlier occupations reduces data coverage, most notably affecting: A13.5 along 0°E in the Atlantic, P03 along 24°N across the Pacific, S4P along 67°S across the South Pacific, much of A16, nominally along 25°W, between the equator and 53°S, and most of P16 along 150°W north of 35°S (Fig 5.1). Regardless, the 27 remaining repeated sections still provide broad spatial coverage of the global ocean (Fig 5.1). Second, we do not combine sections if occupied multiple times in a single year for this analysis because of large seasonal signals in the upper water column.

5.2.2 Sea-surface height from AVISO

The total changes in sea-surface height between section occupations are estimated using the SsaltoDuacs multi-mission delayed time high resolution global merged mapped sea level anomaly (MSLA) produced by AVISO (http://www.aviso.oceanobs.com/duacs/) with support from *CNES* (e.g., Fig 5.2a). The mapped products combine altimetry measurements from the Jason, Envisat, GFO, ERS-2, and TOPEX/Poseidon satellites [*Ducet et al.*, 2000]. The MSLA provides SSH anomalies on a 1/3° × 1/3 ° Mercator grid with weekly resolution between October 1992 and May 2013 available at http://www.aviso.oceanobs.com/en/data.html, downloaded in July 2013. Here we consider uncertainties from formal SSH mapping errors, regional variability, and the GIA correction for changes in the sea-floor height [*von Schuckmann et al.*, 2014] in the error analysis.

5.2.3 *Mapped ocean bottom pressure from GRACE*

We estimate seasonal mass fluctuations between repeat occupations of sections during varying times of the year using 10 years of gridded monthly maps of OBP GRACE release 05 available at http://GRACE.jpl.nasa.gov [*Chambers and Bonin*, 2012]. The spherical harmonic coefficients from the GRACE gravity field are used to produce monthly 1° × 1° resolution global ocean maps in equivalent water thickness anomalies. As of May 2013, monthly maps were available from January 2003 through January 2013 with only 6 months missing. The maps are smoothed with a 500-km horizontal Gaussian smoother. Post-glacial rebound and anti-stripping corrections have been applied. In addition, we apply a 300-km land mask to avoid land leakage biases and remove the average atmospheric pressure loading signal from European Center for Medium Range Weather Forecasts (ECMRWF) [von Schuckmann et. al, 2014]. Here we compare data products from all three of the GRACE processing centers; Center for Space Research (CSR), the Helmholtz Centre Potsdam, German Research Center for Geosciences (GFZ), and the Jet Propulsion Laboratory (JPL). All results presented hereafter are from CSR, with any differences among the products noted. The uncertainty on the mapped OBP is estimated to be 1 cm of equivalent water thickness anomaly throughout most of the ocean with slightly higher uncertainties of 1–2 cm in the polar regions [*Chambers and Bonin*, 2012].

5.2.4 *Regional averaging kernel ocean bottom pressure*

While mapped GRACE data are useful for investigating spatial patterns of variability, the applied 500-km smoother and anti-stripping greatly damp the magnitude of variation in OPB and bias long-term trends [*Johnson and Chambers*, 2013]. Hence we estimate regional decadal trends in ocean mass directly from the spherical harmonic coefficients of the GRACE gravity field using an averaging kernel for each of the seven regions (Fig 5.1). These averaging kernels are used to produce a monthly mean water thickness anomaly for each of the seven regions following the procedure described in Chambers [2009]. GIA corrections are applied to all the GRACE time series. The GIA correction uncertainty is ±0.3–0.6 mm yr^{-1}, depending on the region, for all trends calculated using the GRACE data here [*Chambers et al.*, 2010]. In addition, the monthly global atmospheric pressure fluctuations are removed.

The monthly standard errors for each regional time series range from 0.6 and 2.7 cm of equivalent water thickness. The standard errors scale inversely with the size of the region. The South Pacific (largest surface area) has the smallest error and the Pacific sector of the Southern Ocean (smallest surface area) the largest.

5.3 Ocean mass trends from residuals

Local fluctuations in total sea surface height (SSH) reflect both global-scale changes in ocean volume resulting from additions of heat or mass, but also local changes arising from redistribution of mass or density by changes in ocean circulation. To find the changes in mass, we calculate the residual between changes in SSH and full-depth steric sea level (SSL) along repeats of hydrographic lines. Generally, local changes in SSH are dominated by steric variability, primarily reflecting changes in heat and freshwater within the upper ocean [e.g., *Fukumori and Wang*, 2013]. Once the steric component is removed, the residuals along sections include changes in local mass owing to both long-term trends and mass redistribution associated with large-scale seasonal shifts in ocean circulation [e.g., *Johnson and Chambers*, 2013]. Therefore, we also apply a correction for the expected seasonal mass redistribution estimated from the 10-year GRACE global mapped OBP time series. After the seasonal mass redistribution is accounted for, the residual will be the trend in local mass plus some remaining noise. We take large regional means using all residuals within a region boundary to reduce the noise and find robust estimates of the mean regional mass trends.

We divide the ocean into seven regions to capture some of the expected large-scale variation in mass addition rates [*Johnson and Chambers*, 2013] while still ensuring we have enough data within a region to get a reliable mean (Fig 5.1). Based on this previous work, we divide the Atlantic, Pacific, and Indian oceans into North (60°N to the equator), South (equator to 50°S), and Southern Ocean (south of 50°S). We consider the Indian and Atlantic sectors of the Southern Ocean as one region because mass trends over our study period in these two regions have been similar, perhaps owing to changes in the Weddell Gyre affecting both regions [*Johnson and Chambers*, 2013]. We also combine the south and north Indian Ocean into one region. We have no full-depth repeat sections in the Arctic Ocean, and the sea ice there would make it difficult to use altimeter data, therefore it is not included in this study.

5.3.1 Changes in steric height

We calculate local changes in steric sea level ($\partial SSL/\partial t$) between occupations along each section. Salinity (S) and potential temperature (θ) data along each section are gridded and interpolated onto an evenly spaced grid following *Purkey and Johnson* [2010]. The local ∂SSL/∂t owing to both thermostatic and halosteric contributions from the surface to the bottom between initial (i) and all subsequent occupations are calculated at each grid point along a section using

$$\partial SSL/_{\partial t} = \frac{\int_{bottom}^{surface} \bar{\alpha}(z)\cdot(\theta(z)-\theta_i(z))\cdot dz}{\partial t} + \frac{\int_{bottom}^{surface} -\bar{\beta}(z)\cdot(S(z)-S_i(z))\cdot dz}{\partial t}. \tag{1}$$

The thermal expansion (α) and haline contraction (β) coefficients are calculated using the mean θ and S profile of the two occupations. The θ, S, α, and β profiles are interpolated from the 20-dbar pressure grid onto a 20-m depth grid and integrated using (1) from the surface to the bottom. The difference is converted into a rate per year by dividing by the difference in dates between the two section occupations (∂t; Fig 5.3).

5.3.2 Changes in SSH

We interpolate gridded Aviso SSH maps onto the hydrographic section locations in space and time. We apply a bilinear interpolant to each weekly mapped SSH to find the SSH anomaly along each section (e.g., Fig 5.2a). The SSH anomaly at each grid point along a section is linearly interpolated in time to the occupation dates (Fig 5.2a, black lines). We calculate rates of change per year in SSH (∂SSH/∂t) along each section as the differences between the first occupation and each subsequent occupation divided by the elapsed times (e.g., Fig 5.3).

5.3.3 Seasonal mass corrections

We estimate offsets to correct for any local seasonal mass fluctuations between occupations ($\partial OM_{seasonal}/\partial t$) along sections using mapped GRACE OBP data. At each geographical grid point on the CSR 500-km smoothed maps, we fit a mean value, linear trend, annual harmonic, and semi-annual harmonic to the 10-year time series of monthly mass anomalies and find the standard error of each fit coefficient. At most locations, the annual cycle dominates, with mean and maximum amplitudes of 1.1 and 3.2 cm, respectively.

The mean, annual, and semi-annual expected mass differences along each section between the initial and all subsequent occupations are calculated using the model fit. We interpolate the model coefficients following the same methods used with the AVISO data (e.g., Fig 5.2b). The dates of occupations are used to calculate the expected seasonal changes in ocean mass ($\partial OM_{seasonal}/\partial t$) along each section (e.g., Fig 5.3). Most sections were occupied during similar seasons; therefore the applied differences are usually only a fraction of the maximum annual and semi-annual amplitudes (e.g., Fig 5.2b).

5.3.4 The residual method

We calculate mean trends in ocean mass and associated errors within seven regions (Fig 5.1). The residuals between $\partial SSH/\partial t$, and $\partial SSL/\partial t$ plus $\partial OM_{Seasonal}/\partial t$ along each section are calculated using:

$$res = {\partial SSH}/{\partial t} - {\partial SSL}/{\partial t} - {\partial OM_{Seasonal}}/{\partial t} \tag{2}$$

(Fig 5.3). We calculate the mean and variance of all residuals within each region (Table 5.1; Fig 5.1) to estimate trends in ocean mass.

Each residual is a difference between an initial occupation (t_i) and second occupation (t_2). Within each region the residual reflects the average time period of all section differences used. Therefore, we estimate the average trend period within each region as the mean t_i and mean t_2 of time of occupations (Table 5.1).

We apply Student's t-test to find the two-tailed 90% confidence intervals from the standard deviation of the residuals within each region and combine them with the small uncertainty from the AVISO GIA correction (Table 5.1; Fig 5.1). Degrees of freedom (DOF) are estimated from the sum of the length of all section divided by the typical global horizontal decorrelation length scale of the residual. A length scale of 156 km is used, which corresponds to the mean maximum of the integrals of spatially lagged auto covariances of all sections longer than 1000 km. The GIA correction to the AVISO data set to account for changes in the sea floor introduces an additional ± 0.1 mm yr^{-1} uncertainty to the trend at the 90% confidence level. We combine this ± 0.1 mm yr^{-1} uncertainty with each of the regional variance-based uncertainties assuming the two terms are independent. Hence we square the terms, sum them, and then take the square root. All error bars hereafter reflect these 90% confidence intervals.

Finally, we also calculate a global ocean mass trend using the area-weighted averages from each of the seven regional means. The ocean surface areas within each region, excluding the masked out areas within 300 km of land, are used to calculate a global weighted summed mean and variance. Student's t-distribution is again used to estimate the 90% confidence interval around the mean using the weighted sum of regional variances and the sum of regional DOF, again taking the ± 0.1 mm yr^{-1} GIA correction uncertainty into account.

Throughout this paper we combine variances with GIA uncertainties within each region to estimate 90% two-tailed confidence intervals, as discussed above. However, it is important to note here that there are also expected measurement uncertainties associated with each term in (2). Below we present a brief discussion of the expected measurement error from (2).

We estimate the measurement uncertainties associated with each of the instrumental or mapping terms ($\partial SSH/\partial t$, $\partial SSL/\partial t$, and $\partial OM_{Seasonal}/\partial t$) from (2). The steric instrumental errors are estimated for each $\partial SSL/\partial t$ along every occupation by propagating the expected temperature and salinity CTD accuracies, 0.002 °C and 0.002 respectively [*Joyce*, 1991], through (1). Therefore, this instrumental error is a function of sampling depth. The formal mapping errors from SSH maps, provided by AVISO, are interpolated onto each occupation following the same procedure discussed in section 2.2. The errors for $\partial SSH/\partial t$ between occupations are the sums of the squares of the mapped errors at each location along a section (e.g., Fig 5.3). We calculate the instrumental errors of $\partial OM_{seasonal}/\partial t$ in two ways. The mapped products used to model the seasonal cycle are estimated to have an error of 1–2 cm [*Chambers and Bonin*, 2012]. If we assume this mapping error is correct, we can calculate the weighted model coefficients and the model coefficient errors based on the known mapping error [*Wunsch*, 1996]. Alternatively, we can leave the measurement errors unknown and estimate the errors based on the variance of the residual from the model. Since the mapping errors are uniform for all months, the model coefficients are the same for either method.

Within each region, we calculate the average errors for $\partial SSH/\partial t$, $\partial SSL/\partial t$, $\partial OM_{Seasonal}/\partial t$ by dividing the means by the square roots of each variable's DOF. The DOF of the errors for $\partial SSL/\partial t$ are simply the numbers of total occupations within a region because biases in salinity or temperature tend to be instrument specific and will therefore persist throughout each cruise, making each cruise only a single degree of freedom. The DOF of

$\partial OM_{Seasonal}/\partial t$ are determined by the map's smoothing length of 500 km divided by the length of sections in the region. The DOF of $\partial SSH/\partial t$ however depends on the typical eddy decorrelation length-scale, which varies between 10 and 500 km in the ocean, since the smoothing scale of AVISO is relatively small and generally captures these features. We find the mean long section length scale in the residual to be 156 km, which mostly reflects the variability from $\partial SSH/\partial t$ (e.g., Fig 5.3). Therefore, we chose a conservative length scale of 200 km as a "typical" eddy length scale to estimate the DOF of $\partial SSH/\partial t$.

The regional average uncertainties for $\partial SSH/\partial t$, $\partial SSL/\partial t$, and $\partial OM_{Seasonal}/\partial t$ range between 0.04 to 0.46, 0.00 to 0.01, and 0.04 to 1.05 mm yr^{-1}, with global average uncertainties of 0.13, 0.01, and 0.20 mm yr^{-1}, respectively. While the sums of these errors are on the same order of magnitude of the regional mean variances, the error from the variances should capture most of these instrumental errors, assuming they are randomly distributed and not systematically biased in any way. In addition, errors may also arise from any internal ocean variability on time scales less than a week captured by $\partial SSL/\partial t$ but not $\partial SSH/\partial t$. However, here we consider large regional and global means to reduce the influence of high frequency variability.

5.4 Ocean mass trends from GRACE

Global and regional trends in ocean mass gain are also calculated directly from the monthly regional mean OBP time series for the seven regions. A mean value, trend, annual harmonics, and semiannual harmonics are fit to the regional time series of water thickness equivalent using an unweighted model (Table 5.1). We retain the trends and trend errors and assume Student's t-distribution to estimate 90% confidence intervals (Figs. 5.4–5.5;

Table 5.1). We combine these uncertainties as discussed above with GIA correction uncertainties of 0.6 mm yr^{-1} in the North Atlantic and 0.3 mm yr^{-1} in all other regions. Again, a weighted global mean is calculated using the regional surface areas.

We also calculate a weighted model fit [*Wunsch*, 1996] to evaluate if using the monthly standard errors of each time series, ranging from 0.6 and 2.7 cm of equivalent water thickness, produces significantly different error bars. This weighted model fit produces 90% confidence intervals for the regional trends that are very similar to those found above. The weighted model errors are slightly larger than the unweighted errors except in the South and North Pacific where the errors of the monthly OBP are small and thus the weighted model errors are small. Furthermore, the global mean error for both methods agree within 0.03 mm yr^{-1}, well within error bars. We choose to discuss only the unweighted model errors combined with GIA correction uncertainties below.

5.5 Results

We find a global average ocean mass gain rate of 1.5 (±0.4) mm yr^{-1} SLR equivalent centered on 1996–2006 using the residual method and 1.5 (±0.4) mm yr^{-1} from 2003–2013 using the GRACE method, both with large regional variability (Figs. 5.1; 5.4; Table 5.1). The two method's regional results are consistent in pattern and mostly agree within error bars (Fig. 5.5), despite their different time periods. The regional mass trends reveal 1–3 times greater rates in the North Pacific, South Atlantic, and the Atlantic-Indian sector of the Southern Ocean than in the Pacific sector of the Southern Ocean, North Atlantic, Indian, or South Pacific regions, consistent with previous ocean mass regional studies [e.g., *Johnson and Chambers*, 2013].

The residual method ocean mass trends vary regionally from -0.8 (±1.2) mm yr^{-1} in the Pacific sector of the Southern Ocean to +4.7 (±2.6) mm yr^{-1} in the Indian-Atlantic sector of the Southern Ocean (Fig 5.1; Table 5.1). Five of the seven regions have statistically significant positive trends. The North Atlantic and Pacific sectors of the Southern Ocean both have negative mass trends, but neither is statistically significant (Fig. 5.1). Each regional rate reflects a slightly different time period based on when the sections were occupied within the region. The mean initial occupation (t_i) is between 1993–1997 for all regions. The mean second occupation (t_2) ranges from 2001–2008, with trends over mean time spans of 10.3 years on average (Table 5.1).

The model fits to the regional monthly mass anomalies from the GRACE method also do a good job of capturing low-frequency variability in the South Atlantic, North Pacific, and Atlantic-Indian sector of the Southern Ocean, all showing large, statistically significant positive mass trends of 3.2 (±0.7), 3.6 (±0.7), 3.5 (±0.6) mm yr^{-1} (Fig. 5.4a; d; f). The North Atlantic has a small, but statistically significant, trend of 1.1 (±0.9) mm yr^{-1}, albeit with larger errors on the monthly means. In addition, proximity to regions with high land ice lost rates, may bias the GRACE data in the North Atlantic (Fig. 5.4b) [e.g., *Chambers*, 2009]. Both the fits to the Indian and South Pacific regions capture the large mass seasonal cycle but have no significant decadal trend (Fig. 5.4c; g).

The Pacific sector of the Southern Ocean and the North Pacific are the only regions where the model applied to the GRACE data has residuals with structure. The North Pacific region has residual structure that increases by ~1 cm from 2003–2007 and then returns to zero afterwards (Fig. 5.4a). This result is consistent with large low-frequency fluctuations in bottom pressure throughout the sub-polar gyre observed over this period [*Chambers*, 2011; his Figure 6]. In the Pacific sector of the Southern Ocean, the amplitude of the model residual is as large as the model, so the model does not fit the data well. The model does find a slight negative trend of -1.5 (±1.2) mm yr^{-1}, however, this trend is not consistent over the entire time period and subsampling yields radically different trends (Fig. 5.4e). The proximity of this region to West Antarctic ice sheets, with their large mass losses, may introduce short time-scale noise and systematic biases in the trend. Even with the 300-km land mask and applied corrections, land leakage from areas with large changes can still introduce large bias errors [*Chambers*, 2009].

5.5.1 Regional trends

Regional trends are consistent between the two methods even though they are estimated over somewhat different time periods. Both suggest the Indian-Atlantic sector of the Southern Ocean and North Pacific are gaining mass while the North Atlantic and Pacific sector of the Southern Ocean are losing mass (Fig. 5.5). The regional mean mass trends and 90% confidence intervals are discussed in light of previous work.

The mass trends in the two Southern Ocean regions suggest a large dipole between the Atlantic-Indian sector and Pacific sector of the Southern Ocean, with the residual method showing the Indo-Atlantic sector increasing mass at a rate of 4.7 (±2.6) mm yr^{-1} and the Pacific Sector decreasing mass at a rate of -0.8 (±1.2) mm yr^{-1} (Figs. 1; 4e–f; Table 5.1). The negative trend in the Pacific sector of the Southern Ocean has been previously noted using GRACE products, perhaps connected to land leakage from the melting West Antarctic Ice Sheet [*Chambers*, 2009]. However, here we find consistent negative trends using the residual method, independent from the GRACE method, although both methods have large errors. The observed small or negative SLR rates in the North Atlantic and

Pacific Sector of the Southern Ocean could also be owing partly to changes in the gravitational field caused by mass loss of the Greenland and the West Antarctic Ice Sheets, which tends to reduce sea level rise around these locations, and increase them elsewhere [e.g., *Bamber and Riva*, 2010]. The strong positive trend in the Indian-Atlantic sector of the Southern Ocean is consistent with *Johnson and Chambers* [2013], which found OBP trends as high as 2–5 mm yr^{-1} above the global mean rate in these regions. They suggest these changes could be linked to small variations in the strength of the Antarctic Circumpolar Current [e.g., *Hogg et al.*, 2014] or the Weddell Gyre.

Both methods yield a relatively large ocean mass gain in the North Pacific with a small to zero mass gain in the North Atlantic. The GRACE method's largest mass trend is in the North Pacific, at a rate of 3.5 (±0.7) mm yr^{-1} (Table 5.1; Fig. 5.4a). The residual method also finds a relatively large positive ocean mass trend of 1.5 (±0.6) mm yr^{-1} gain from 1999–2006, albeit half the magnitude from the GRACE method (Fig 5.1; Table 5.1). This large trend in local mass addition has been linked to changes in the strength of wind stress curl [*Chambers and Willis*, 2008; *Chambers*, 2011; *Cheng et al.*, 2013]. The full column residual method in the North Atlantic, on the other hand, has a non-significant contribution to SLR from the ocean mass trend of -0.1 (±2.7), albeit with very large error bars, whereas the GRACE method finds a positive ocean mass trend of 1.1 (±0.9) mm yr^{-1} (Fig. 5.4b).

The residual method finds a positive trend in all the south basins, with the GRACE method showing only a positive trend in the South Atlantic (Table 5.1; Figs. 1; 4c; d). The South Pacific has ~1 mm yr^{-1} gain from the residual and less than 0.1 mm yr^{-1} from GRACE (Table 5.1). The South Atlantic residual estimates a mass increase of 3.3 (±1.4) mm yr^{-1}, consistent with the estimate from the GRACE methods, albeit based on limited data (Fig

5.1). The residual method finds a positive trend in ocean mass in the Indian Ocean of 1.1 (±0.8) mm yr^{-1}, statistically different from the GRACE method rate of 0.0 (±0.6). However, the December 2004 Indonesia earthquake could affect GRACE products in this region [e.g., *Chen et al.*, 2007], or there may be interdecadal variability, with rate of mass gain changing over the somewhat different time periods considered by the two methods.

5.5.2 Global trends

The residual and GRACE methods both find the area-weighted global mean mass contribution to SLR to be 1.5 (±0.4) mm yr^{-1}, reflecting 1996–2006 for the residual method and 2003–2013 for the GRACE method (Fig. 5.4h; Table 5.1). Neither global mean includes the Arctic and both are area-weighted means of the seven regions. The 90% confidence intervals from the two methods are similar, despite reflecting different uncertainties. The residual method's confidence interval primarily reflects the large variance in the residual, with only a small contribution from the GIA correction uncertainty. In contrast, the GRACE method sees a relatively small variance in the trend (Fig 5.1h) but the error is increased substantially by the 0.3 mm yr^{-1} GIA correction uncertainty, inflating the total uncertainty to 0.4 mm yr^{-1}.

The two methods are in very good agreement with each other and previous estimates. The residual method 1996–2006 trend is within error of *Church et al.* [2011] 1993–2008 total mass contribution of 1.66 (±0.46) mm yr^{-1}. Our GRACE method global mean is slightly less than *Johnson and Chambers* [2013] estimate of 1.8 mm yr^{-1} over a very similar period, but theirs is a global averaging kernel and our weighted sum of smaller areas both attenuates the trend and excludes the Arctic.

5.5.3 The $\partial OM_{seasonal}/\partial t$ term:

Seasonal mass redistribution adjustments, the $\partial OM_{seasonal}/\partial t$ term in (2), are a small contribution to the SLR budget in all regions, owing to both the comparatively small seasonal cycle and because most repeat sections are occupied during similar months (e.g., Figs. 2b; 3). To demonstrate this, we re-calculate regional residuals from the residual method using two variations on $\partial OM_{seasonal}/\partial t$. First, the regional means are re-calculated using the coefficients from JPL and GFZ instead of CSR. The GFZ coefficients are slightly different from JPL or CSR; however, these variations do not affect the regional or global trends. Second, if the $\partial OM_{seasonal}/\partial t$ term is excluded from (2) altogether, the regional trends stay within the 90% confidence intervals in all except the South Pacific region, where the regional trend decreases substantially from 1.0 (±0.4) mm yr^{-1} with the $\partial OM_{seasonal}/\partial t$ term to 0.3 (±0.4) mm yr^{-1} without the $\partial OM_{seasonal}/\partial t$ term. The global mean estimate is insensitive to which GRACE mapped product are used and, when no GRACE seasonal adjustments are used, only changes slightly, to 1.4 ± 0.5 mm yr^{-1}.

Applying the $\partial OM_{seasonal}/\partial t$ offset in (2) limits our study area to regions of the ocean further than 300 km from the coast owing to the land leakage mask associated with the GRACE mapped products. We test the effect of this mask on our results by calculating the regional residual from (2) without GRACE, both with the land mask and without. The land mask eliminates a substantial fraction of our section data, changing the total length of all sections used from 1.4×10^5 km to 1.1×10^5 km. Nonetheless, the only regions whose rates change > 0.1 mm yr^{-1} is the Indian-Atlantic sector of the Southern Ocean and the Indian Ocean which increased by 0.7 mm yr^{-1} and 0.6 mm yr^{-1}, respectively. Again, the global trends are essentially unaffected by the masking, with the rates increasing by ~ 0.1 mm yr^{-1}, well within the error bars.

5.6 Deep steric contributions

We evaluate the relative importance of the deep steric contribution to the SLR budget by using a variation of the residual method. Here we are asking, ‘How much error is introduced into the SLR budget when the full water-column steric contribution is not included?’ We do not directly calculate the steric component here because the temporal and spatial coverage of the data used is not sufficient to capture the high variability in the upper water column. However, by taking the residual between SSH and the upper water column steric contribution, we remove most of this variability, and are left with the mass plus the deep steric contribution. Therefore, we calculate the regional and global ocean mass addition trends by integrating (1) from the surface to 300, 700, 1000, 2000, 3000, and 4000 m and compare the results to the ocean mass addition trends found using the full water column steric contribution.

The deep ocean steric contribution is found to add 0.78, 0.40, 0.36, 0.07, 0.06, and 0.05 mm yr^{-1} from 300–700, 700–1000, 1000–2000, 2000–3000, 3000–4000, and 4000–6000 m, respectively. Therefore, neglecting the deep steric sea level component below 300, 700, 1000, or 2000 m increases the expected mass component of the SLR budget by 117%, 65%, 38%, or 13%, respectively (Fig. 5.6). The sparse sampling of full-depth repeat sections may lead to aliasing of steric variability, captured in SSH but not SSL when the full column steric term is not used in (2). The large deep steric contribution estimated here between 300–2000 m of 1.53 mm yr^{-1}, over twice as large as previously estimated rates [e.g., *Levitus et al.*, 2012], most likely reflects a sampling bias. However, this calculation suggests that previous sea level budgets calculating mass addition from the difference between total sea level and upper steric contributions, neglecting say the ocean below 2000 m, where aliasing is likely smaller, may over-estimate that mass contribution by 13%. This result is consistent with previous studies estimating that the deep steric expansion below 2000 m is contributing roughly 6% to the total SLR budget [e.g., *Purkey and Johnson*, 2010]. Finally, if the steric contribution is limited to only the upper 1000 m or less of the water column, the residual no longer falls within the 90% confidence limits of the GRACE method, and the budget will not close (Fig. 5.6).

The relative contribution of the deep ocean to the SLR budget varies considerably by region (Fig. 5.6). In regions where deep convection communicates surface heating to the deep ocean, one would expect a higher contribution from deep steric changes. Accordingly, the Indian-Atlantic sector of the Southern Ocean has substantial contributions through the water column, extending below 4000 m. The North Atlantic also has a large contribution from steric changes from 700–2000 m. In the Pacific sector of the Southern Ocean, however, there was no contribution between 300 m and 6000 m outside the error bars, inconsistent with previous deep steric estimates in the region, possible owing to less data used in this region because of the 300-km land mask and the post-1992 repeat criteria used here (e.g., Fig 5.1 vs. Fig 5.1 of *Purkey and Johnson* [2010]). Elsewhere, the deep ocean below 2000 m contributes 1–17% to the residual OM calculation, roughly consistent with previous deep steric contributions from deep ocean warming [e.g., *Purkey and Johnson*, 2010].

5.7 Discussion

The success of the residual method relies on two assumptions. First, we assume that the ocean mass addition trend has been approximately linear between October 1992–2013. We find a linear trend in ocean mass from 2003–2013 from the GRACE method in most of the seven regions considered here (Fig. 5.4). The AVISO SSH record is also well described by a linear trend in SSH over the whole time period used here, although there is certainly some interannual variability in both records [*Boening et al.*, 2011; *Fasullo et al.*, 2013]. Given the limited temporal coverage we have for the residual method, a linear trend is all that can be resolved. We find agreement within the 90% confidence intervals of the two methods globally and regionally in most cases, suggesting the trend rate from 1996–2006 versus 2003–2013 has not changed significantly, or at least not outside our error estimates (Fig. 5.5).

Second, we balance making our regions small enough to capture regional variability in ocean mass but large enough so the regional means rise above the noise. The variability at any given location along the sections is 10 times the amplitude of the regional ocean mass trends presented here and therefore, at any given point the residual is meaningless (e.g., Fig 5.3). However, the residuals averaged over large enough regions should reflect the large-scale mass signal, estimated within the stated errors. On the other hand, while the gravity wave adjustment happens rapidly when the ocean gains external mass, spreading that mass signal over the global oceans, regional differences in ocean mass rates can arise [e.g., *Lorbacher et al.*, 2012; *Johnson and Chambers*, 2013], probably owing to changes in wind forcing [e.g., *Chambers and Willis*, 2008; *Cheng et al.*, 2013] and the gravitational field from melting ice [e.g., *Bamber and Rivas*, 2010]. Here we have chosen enclosed regions to resolve ocean mass patterns found by *Johnson and Chambers* [2013] but still large enough to get meaningful averages.

In summary, here we present a new estimate of ocean mass addition extending back to October 1992 calculated independently of GRACE and using a full column steric SLR budget. This GRACE-independent residual method finds a global mass addition trend of 1.5 (±0.4) mm yr^{-1} from 1996–2006 by calculating the difference between total SSH and in situ full depth steric sea level. This finding is in good agreement with the global ocean mass trend of 1.5 (±0.4) mm yr^{-1} from 2003–2013 found by GRACE. Both methods agree on large-scale patterns of higher rates of ocean mass gain in the Indian-Atlantic sector of the Southern Ocean, the North Pacific and the South Atlantic. Finally, we have also estimated the relative importance of the deep ocean to the SLR budget, with the deep ocean steric expansion below 700 m (2000 m) equivalent to 65% (13%) of the ocean mass contribution to sea level.

Acknowledgments

The altimeter products were produced by Ssalto/*Duacs* and distributed by *AVISO*, with support from *CNES* (http://www.aviso.oceanobs.com/duacs/). GRACE ocean data were processed by Don P. Chambers, supported by the NASA MEASURES Program, and are available at http://GRACE.jpl.nasa.gov. Cecilia Bitz provided an insightful comment on early results. The findings and conclusions in this article are those of the authors and do not necessarily reflect the views of the National Oceanic and Atmospheric Administration (NOAA). This work was supported by the NOAA Climate Program Office, NOAA Research, and NASA Headquarters under the NASA Earth and Space Fellowship Program - Grant

NNX11AL89H. DPC was funded through NASA Grant NNX12AL28G. PMEL Contribution Number 4170.

References:

Ablain, M., A. Cazenave, G. Valladeau, and S. Cuinehut (2009), A new assessment of the error budget of global mean sea level rate estimated by satellite altimetry over 1993–2008, *Ocean Sci.*, *5*, 193–201, doi:10.5194/os-5-193-2009.

Bamber, J., and R. Riva (2010), The sea level fingerprint of recent ice mass fluxes, *The Cryosphere*, *4*, 621–627, doi:10.5194/tc-4-621-2010.

Boening, C., J. K. Willis, F. W. Landerer, R. S. Nerem, and J. Fasullo (2012), The 2011 La Niña: So strong, the oceans fell, *Geophys. Res. Lett., 39*, L19602, doi:10.1029/2012GL053055.

Cazenave, A., K. Dominh, S. Guinehut, E. Berthier, W. Llovel, G. Ramillien, M. Ablain, and G. Larnicol (2009), Sea level budget over 2003–2008: A reevaluation from GRACE space gravimetry, satellite altimetry and Argo, *Global Planet. Change*, *65*, 83–88, doi:10.1016/j.gloplacha.2008.10.004.

Chambers, D. P. (2009), Calculating trends from GRACE in the presence of large changes in continental ice storage and ocean mass, *Geophys. J. Int.*, *176*, 415–419, doi:10.1111/j.1365-246X.2008.04012.x.

Chambers, D. P. (2011), ENSO-correlated fluctuations in ocean bottom pressure and wind-stress curl in the North Pacific, *Ocean Sci.*, *7*, 685–692, doi:10.5194/os-7–685-2011.

Chambers, D. P., and J. A. Bonin (2012), Evaluation of Release-05 GRACE time-variable gravity coefficients over the ocean, *Ocean Sci.*, *8*, 859–868, doi:10.5194/os-8-859-2012.

Chambers, D. P., and J. K. Willis (2008), Analysis of large-scale ocean bottom pressure variability in the North Pacific, *J. Geophys. Res.*, *113*, C11003, doi:10.1029/2008JC004930.

Chambers, D. P., and J. K. Willis (2010), A Global Evaluation of Ocean Bottom Pressure from

GRACE, OMCT, and Steric-Corrected Altimetry, J*. Atmos. Oceanic Tech.*, *27*, 1–8, doi:10.1175/2010JTECHO738.1.

Chambers, D. P., and J. Schröter (2011), Measuring ocean mass variability from satellite gravimetry, *J. Geodynam.*, *52*, 333–343, doi:10.1016/j.jog.2011.04.004.

Chambers, D. P., J. Wahr, M. E. Tamisiea, and R. S. Nerem (2010), Ocean mass from GRACE and glacial isostatic adjustment, *J. Geophys. Res.*, *115*, B11415, doi:10.1029/2010JB007530.

Chen, J. L., C. R. Wilson, B. D. Tapley, and S. Gran (2007), GRACE detects coseismic and postseismic deformation from the Sumatra-Andaman earthquake, *Geophys. Res. Lett.*, *34*, L13302, doi: 10.1029/2007GL030356.

Cheng, X., L. Li, Y. Du, J. Wang, and R.-X. Huang (2013), Mass-induced sea level change in the northwestern North Pacific and its contribution to total sea level change, *Geophys. Res. Lett.*, *40*, 3975–3980, doi:10.1002/grl.50748.

Church, J. A. and Coauthors (2013), Sea Level Change. In: Climate Change 2013: The Physical Science Basis. Contribution of Working Group I to the Fifth Assessment Report of the Intergovernmental Panel on Climate Change [Stocker, T.F., D. Qin, G.-K. Plattner, M. Tignor, S.K. Allen, J. Boschung, A. Nauels, Y. Xia, V. Bex and P.M. Midgley (eds.)]. Cambridge University Press, Cambridge, United Kingdom and New York, NY, USA.

Church, J. A. and Coauthors (2011), Revisiting the Earth's sea-level and energy budgets from 1961 to 2008, *Geophys. Res. Lett.*, *38*, L18601, doi:10.1029/2011GL048794.

Church, J. A., and N. J. White (2011), Sea-Level Rise from the Late 19th to the Early 21st Century, *Surv. Geophys.*, *32*, 585–602, doi:10.1007/s10712-011-9119-1.

Domingues, C. M., J. A. Church, N. J. White, P. J. Gleckler, S. E. Wijffels, P. M. Barker, and J. R. Dunn (2008), Improved estimates of upper-ocean warming and multi-decadal sea-level rise, *Nature*, *453*, 1090–1093, doi:10.1038/nature07080.

Ducet, N., P.-Y. Le Traon, and G. Reverdin (2000), Global high-resolution mapping of ocean circulation from TOPEX/Poseidon and ERS-1 and -2, *J. Geophys. Res.*, *105*, 19,477–19,498

Fasullo, J. T., C. Boening, F. W. Landerer, and R. S. Nerem (2013), Australia's unique influence on global sea level in 2010–2011, *Geophys. Res. Lett., 40,* 4368–4373, *doi:*10.1002/grl.50834.

Fukumori, I., and O. Wang (2013), Origins of heat and freshwater anomalies underlying regional decadal sea level trends, *Geophys. Res. Lett.*, *40*, 563–567, doi:10.1002/grl.50164.

Gardner, A. S. and Coauthors (2013), A Reconciled Estimate of Glacier Contributions to Sea Level Rise: 2003 to 2009, *Science*, *340*, 852–857, doi:10.1126/science.1234532.

Hogg, A. McC., M. P. Meredith, D. P. Chambers, E. P. Abrahamsen, C. W. Hughes, and A. K. Morrison (2014), Recent trends in the Southern Ocean eddy field and Antarctic Circumpolar Current, *Geophys. Res. Lett.*, accepted.

Johnson, G. C., and D. P. Chambers (2013), Ocean bottom pressure seasonal cycles and decadal trends from GRACE Release-05: Ocean circulation implications, *J. Geophys. Res.*, *118*, 4228–4240, doi:10.1002/jgrc.20307.

Joyce, T. M. (1991), Introduction to the Collection of Expert Reports Compiled for the WHP Program. WOCE Hydrographic operations and methods. WOCE Operations Manual. WHP Office Report WHPO-91-1, WOCE Report no. 68/91.

LeBel, D. A., W. M. Smethie Jr., M. Rhein, D. Kieke, R. A. Fine, J. L. Bullister, D.-H. Min, W. Roether, R. F. Weiss, C. Andrié, D. Smythe-Wright, E. P. Jones (2008), The formation rate of North Atlantic Deep Water and Eighteen Degree Water calculated from CFC-11 inventories observed during WOCE, *Deep-Sea Res. I*, *55*, 891–910.

Leuliette, E. W., and L. Miller (2009), Closing the sea level rise budget with altimetry, Argo, and GRACE. *Geophys. Res. Lett.*, *36*, L04608, doi:10.1029/2008GL036010.

Leuliette, E. W., R. S. Nerem, and G. T. Mitchum (2004), Calibration of TOPEX/Poseidon and Jason Altimeter Data to Construct a Continuous Record of Mean Sea Level Change, *Mar. Geod.*, *27*, 79–94, doi:10.1080/01490410490465193.

Leuliette, E., and J. Willis (2011), Balancing the Sea Level Budget, *Oceanogr. Mag.*, *24*, 122–129, doi:10.5670/oceanog.2011.32.

Levitus, S. and Coauthors (2012), World ocean heat content and thermosteric sea level change (0-2000 m), 1955-2010, *Geophys. Res. Lett.*, *39*, doi:10.1029/2012GL051106.

Lombard, A., A. Cazenave, K. DoMinh, C. Cabanes, and R. S. Nerem (2005), Thermosteric sea level rise for the past 50 years; comparison with tide gauges and inference on water mass contribution, *Global Planet. Change*, *48*, 303–312.

Lorbacher, K., S. J. Marsland, J. A. Church, S. M. Griffies, and D. Stammer (2012), Rapid barotropic sea level rise from ice sheet melting, *J. Geophys. Res.*, *117*, C06003–C06010, doi:10.1029/2011JC007733.

Lowe, J. A., and J. M. Gregory (2006), Understanding projections of sea level rise in a Hadley Centre coupled climate model, *J. Geophys. Res.*, *111*, C11014, doi:10.1029/2005JC003421.

Mauritzen, C., A. Melsom, and R. T. Sutton (2012), Importance of density-compensated temperature change for deep North Atlantic Ocean heat uptake, *Nature Geosci.*, *5*, 905–910, doi:10.1038/ngeo1639.

Merrifield, M. A., P. R. Thompson, M. Lander, and K. Aagaard (2012), Multidecadal sea level anomalies and trends in the western tropical Pacific, *Geophys. Res. Lett.*, *39*, doi:10.1029/2012GL052032.

Nerem, R. S., D. P. Chambers, C. Choe, and G. T. Mitchum (2010), Estimating Mean Sea Level Change from the TOPEX and Jason Altimeter Missions, *Mar. Geod.*, *33*, 435–446, doi:10.1080/01490419.2010.491031.

Orsi, A. H., G. C. Johnson, and J. L. Bullister (1999), Circulation, mixing, and production of Antarctic Bottom Water, *Prog. Oceanogr.*, *43*, 55–109.

Purkey, S. G., and G. C. Johnson (2010), Warming of Global Abyssal and Deep Southern Ocean Waters between the 1990s and 2000s: Contributions to Global Heat and Sea Level Rise Budgets, *J. Climate*, *23*, 6336–6351, doi:10.1175/2010JCLI3682.1.

Rhein, M., and Coauthors (2013), Observations: Ocean. In: Climate Change 2013: The Physical Science Basis. Contribution of Working Group I to the Fifth Assessment Report of the Intergovernmental Panel on Climate Change [Stocker, T.F., D. Qin, G.-K. Plattner, M. Tignor, S.K. Allen, J. Boschung, A. Nauels, Y. Xia, V. Bex and P.M. Midgley (eds.)]. Cambridge University Press, Cambridge, United Kingdom and New York, NY, USA.

Shepherd, A. and Coauthors (2012), A Reconciled Estimate of Ice-Sheet Mass Balance, *Science*, *338*, 1183–1189, doi:10.1126/science.1228102.

von Schuckmann, K., J.-B. Sallée, D. Chambers, P.-Y. Le Traon, C. Cabanes, F. Gaillard, S. Speich, and M. Hamon (2014), Monitoring ocean heat content from the current generation of global ocean observing systems, *Ocean Sci*., in press.

Willis, J. K., D. P. Chambers, and R. S. Nerem (2008), Assessing the globally averaged sea level budget on seasonal to interannual timescales, *J. Geophys. Res.*, *113*, C06015, doi:10.1029/2007JC004517.

Wunsch (1996), The Ocean Circulation Inverse Problem, Cambridge University Press, Cambridge M.A., pp 103-133.

Ocean Region	Residual Method		GRACE Method	
	Mean time period of trend (year)	Mass trend (mm yr^{-1})	Time period of trend (year)	Mass trend (mm yr^{-1})
North Pacific	1999.4–2006.8	1.53 ± 0.58	2003–2013	3.59 ± 0.71
North Atlantic	1995.0–2003.3	-0.09 ± 2.67	2003–2013	1.12 ± 0.89
South Pacific	1996.1–2008.1	1.03 ± 0.40	2003–2013	0.08 ± 0.62
South Atlantic	1993.1–2007.4	3.26 ± 1.41	2003–2013	3.23 ± 0.68
Pacific sector of the Southern Ocean	1994.2–2006.7	-0.80 ± 1.23	2003–2013	-1.49 ± 1.18
Indian-Atlantic sector of the Southern Ocean	1994.4–2001.8	4.66 ± 2.57	2003–2013	3.52 ± 0.61
Indian	1995.0–2005.5	1.12 ± 0.77	2003–2013	0.03 ± 0.55
Global Mean	1996.1–2006.3	1.47 ± 0.45	2003–2013	1.53 ± 0.36

Table 5.1: Regional and global (excepting the Arctic) trends in sea level rise (SLR) owing to ocean mass addition using the residual method (see Section 4) and the GRACE method (see Section 5) over the time periods given with the two-tailed 90% confidence limits.

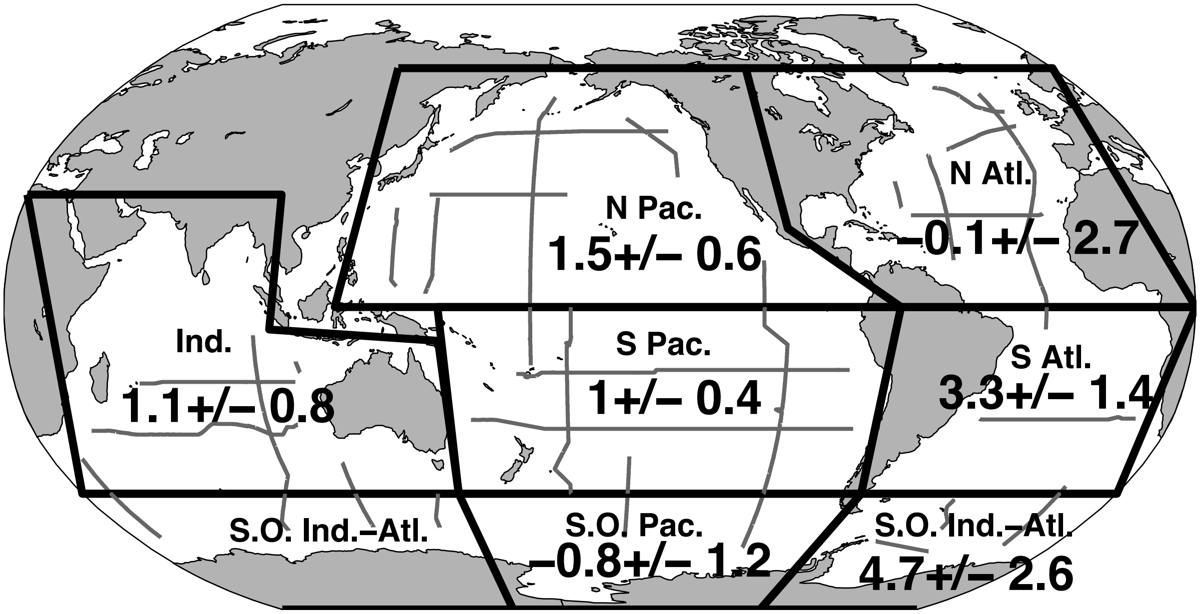

Figure 5.1: Regional (black lines) mean ocean mass sea level rise (mm yr^{-1}) calculated from the residual between total and steric sea level changes along sections (gray lines). Uncertainties given are two-tailed 90% confidence limits.

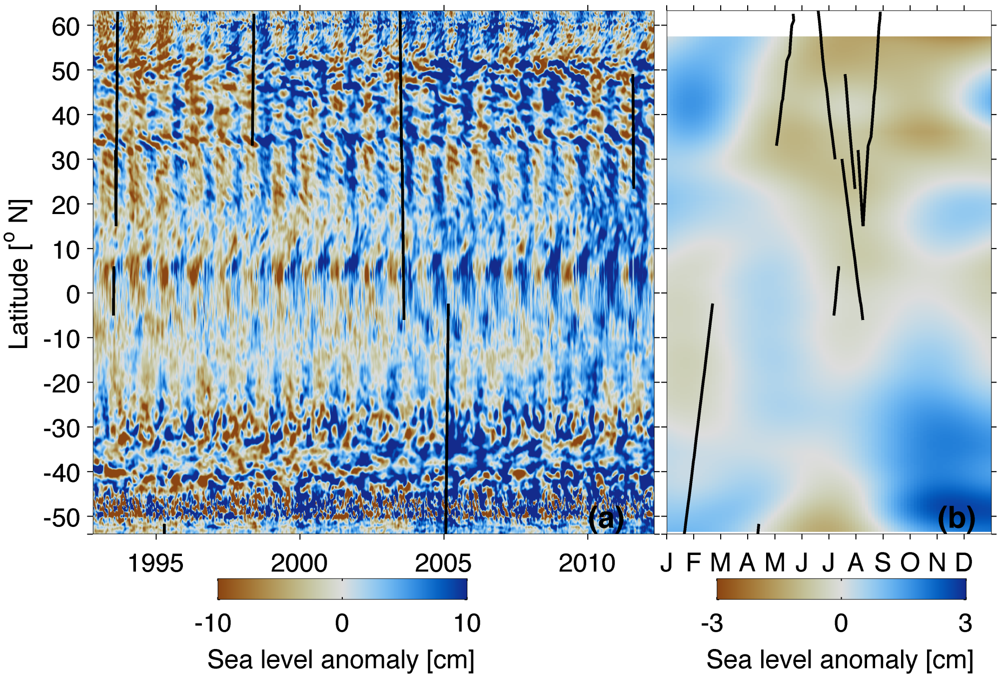

Figure 5.2: Total sea level variability from AVISO satellite altimetry (a) and seasonal mass cycle (January- December) from GRACE ocean bottom pressure (b) along approximately 25 °W through the Atlantic Ocean. Full depth in-situ data are located along black lines.

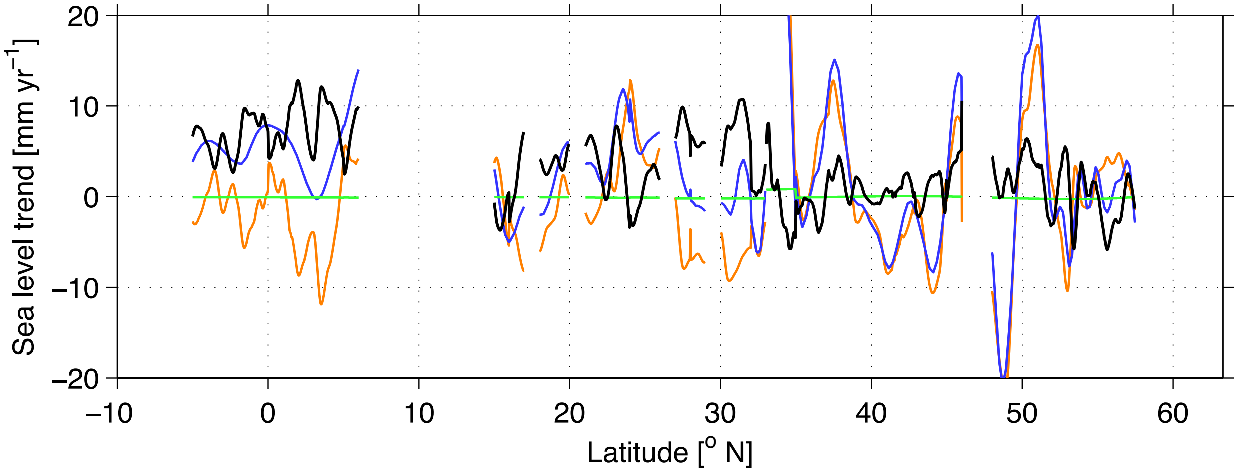

Figure 5.3: The rate of change in full-depth steric (orange) and mass seasonal cycle (green) contributions to total (blue) sea level trends (in mm yr^{-1}) nominally along 25 °W (Fig. 5.1) between the 1993 and 2003 occupations of WOCE section A16. The residual (black) between the total and the sum of the full-depth steric and mass seasonal cycle is also shown.

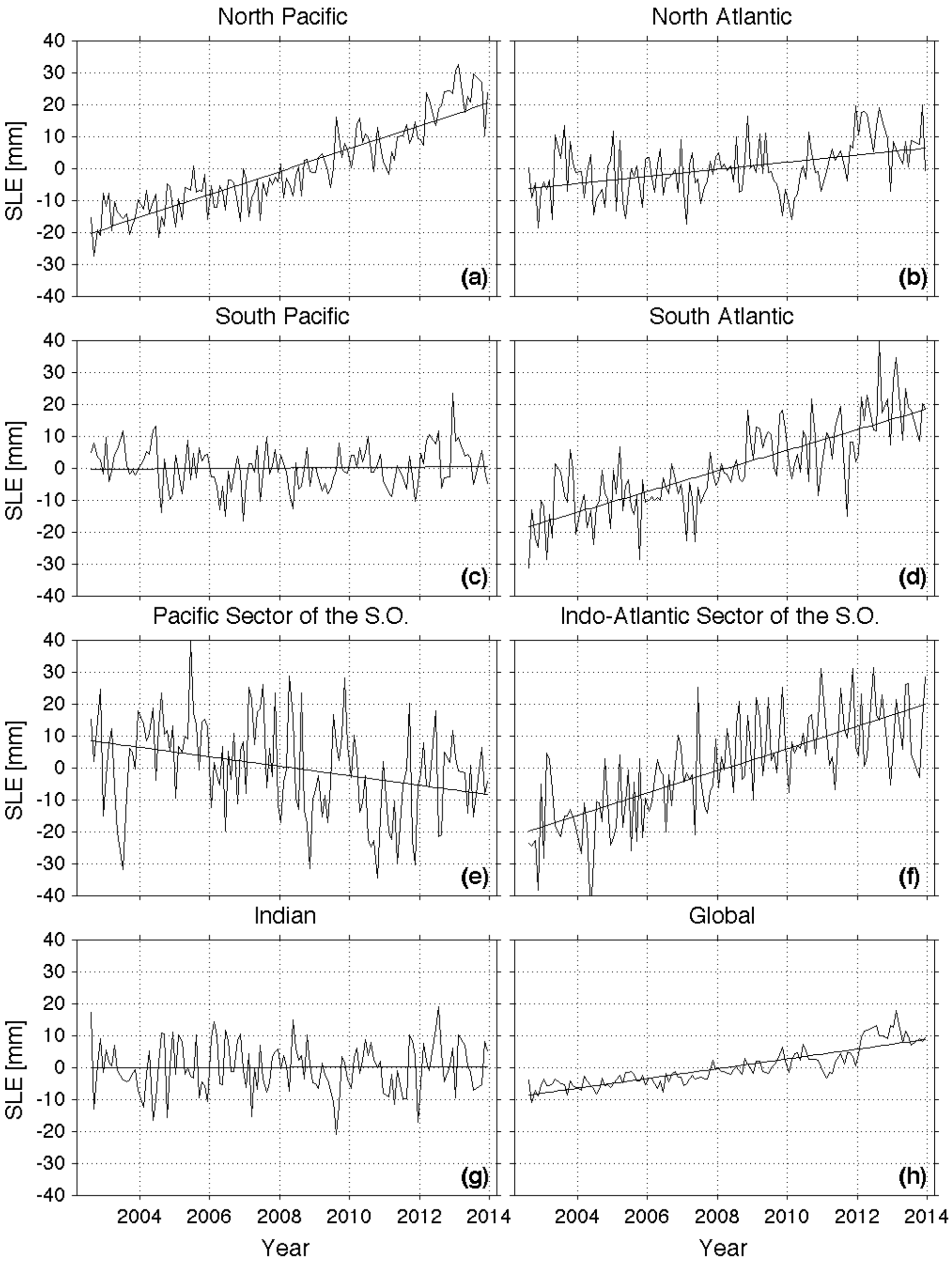

Figure 5.4: Linear trends (straight lines) of 2003–2013 time series of GRACE ocean bottom pressure anomaly with the annual and semi-annual seasonal cycle removed (squiggly lines) in Sea Level Equivalent (SLE) for the seven (a-g) regions (see Fig 5.1) and the area-weighted global mean (h).

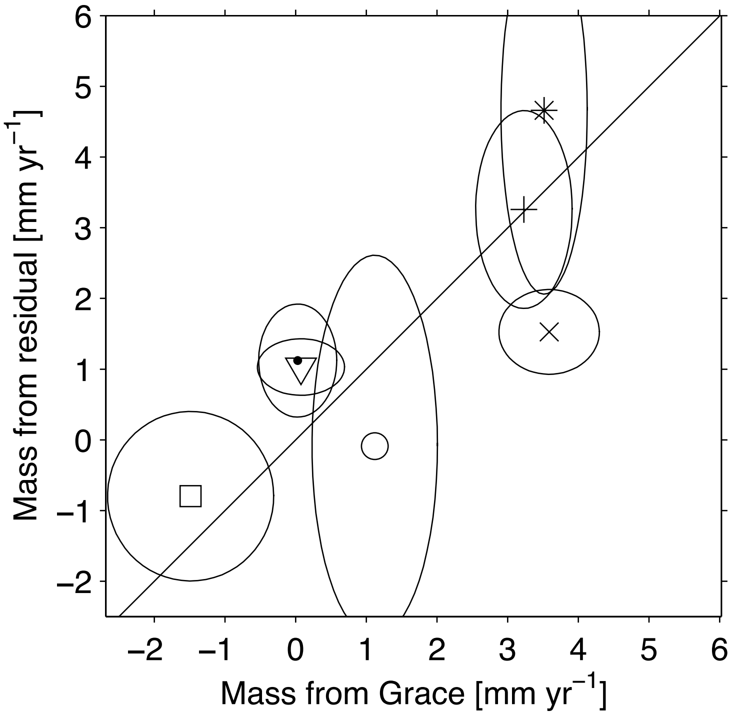

Figure 5.5: Regional mean ocean mass trends in the Indian (•), North Atlantic (O), North Pacific (x), South Atlantic (+), Southern Ocean Atlantic-Indian sector (*), Southern Ocean Pacific sector(□), and South Pacific (Δ) calculated from full-depth section residuals and from GRACE from 2003–2013 with 90% confidence intervals (Table 5.1). Diagonal line indicates a one-to-one ratio.

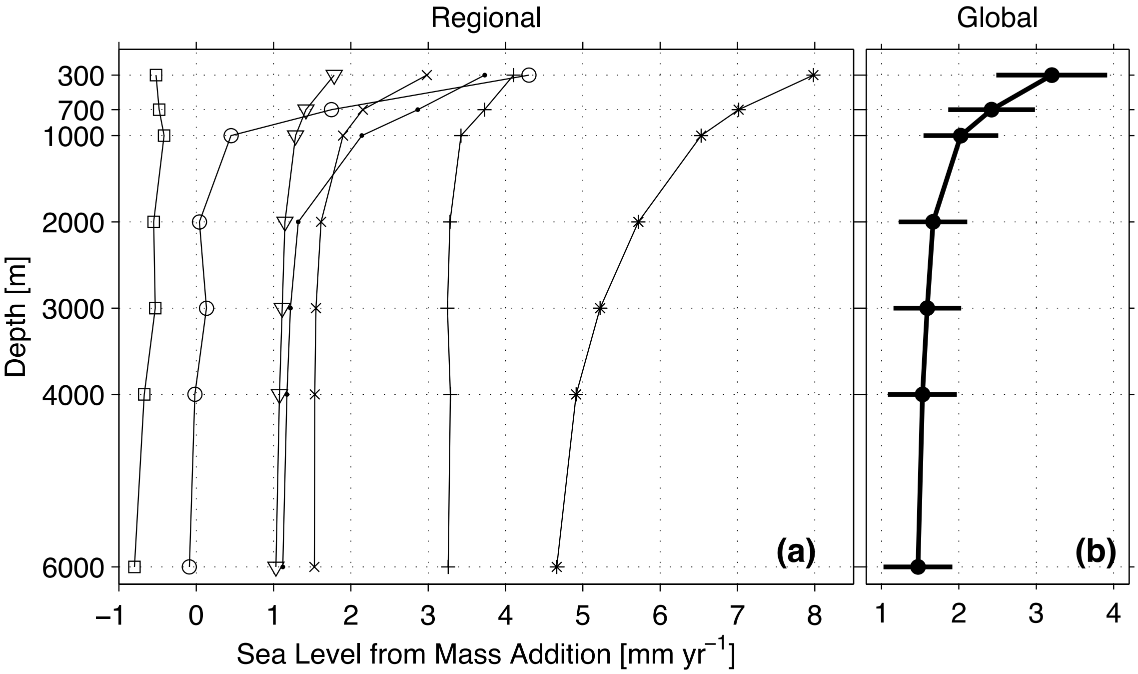

Figure 5.6: Area average trends of residuals between total sea level and steric contributions in the Indian (•), North Atlantic (O), North Pacific (x), South Atlantic (+), Southern Ocean Atlantic-Indian sector (*), Southern Ocean Pacific sector (□), and South Pacific (Δ) and global (b) with 90% confidence intervals vs. depth of integration from the surface.

Chapter 6

Conclusion

This dissertation assesses the role the deep ocean has played in the global heat and Sea Level Rise (SLR) budgets during the 1990s and 2000s. The Earth is currently in radiative imbalance owing to increased atmospheric greenhouse gasses, with over 90% of this excess heat being absorbed by the oceans (Rhein et al., 2013). Therefore, in order to accurately quantify this radiative imbalance, precise knowledge of ocean warming is needed. While the upper 2000 m of ocean are now relatively well monitored by Argo, the deep ocean is sparsely measured in space and time, so many previous global heat budgets either ignore or crudely estimate the deep ocean's contribution. Here, despite limited data, we have shown the deep ocean has contributed substantially to both the global heat and SLR budgets between the 1990s and 2000s and demonstrated the importance of further monitoring the deep ocean.

Chapter 2 uses in-situ observations to quantify abyssal warming between the 1990s and 2000s, focusing on regions fed by a southern bottom water mass, Antarctic Bottom Water (AABW). Here, the first global analysis of abyssal warming (below 4000 m) on isobars is presented, finding a statistically significant warming equivalent to over 10% of the global heat imbalance over the time period. Abyssal warming is quantified within 32 individual deep ocean basins, presenting a clear global pattern of southern originating abyssal warming. The strongest warming is observed in the three southernmost basins around Antarctica directly fed by AABW. The abyssal warming continues to the north, at progressively decreasing magnitudes, along three of the four deep western boundary currents. The abyssal warming below 4000 m, plus the deep Southern Ocean warming between 1000 m and 4000 m, is equivalent to 0.10 (± 0.6) W m^{-2} heat flux absorbed over the entire surface of the earth, or 1/6 the upper ocean energy absorption rate. Furthermore, this warming contributes 0.14 (± 0.08) mm yr^{-1} to global steric sea level rise.

It has been hypothesized that distant abyssal warming could be driven by changes in AABW formation rates causing a global scale contraction of AABW, communicated throughout the global ocean on short time scales via internal gravity waves (Masuda et al., 2010). This falling of isotherms is observed as warming on isobars. In Chapter 3, we re-examine the abyssal warming discussed in Chapter 2 through a volume analysis, revealing the warming is equivalent to a reduction of AABW (here defined as water with potential temperature, $\theta < 0$ °C) at a rate of 8.2 (± 2.6) Sv between the 1990s and 2000s. In the Southern Ocean, the volume loss appears to be bottom-intensified, with a loss of coldest AABW waters at the bottom causing a near-uniform descent of potential isotherms throughout much of the water column until a near surface recovery from an increase in CDW from the north. The volume decrease continues to the north along three of the four main northward outflow routes of AABW indicating a global scale slowdown of the bottom, southern limb of the Meridional Overturning Circulation (MOC).

Chapter 4 focuses on salinity (S) changes in the more recently formed AABW, within the Southern Ocean. Here, we assess where θ and S water-property changes are driven by vertical isotherm heave (as discussed in Chapter 3) vs. water-mass change. This analysis reveals a large water-mass freshening in addition to a volume reduction in the newly formed AABW in the Pacific and Indian sectors of the Southern Ocean, with magnitudes strongest near the source regions. The water-mass freshening was equivalent to freshwater flux of 73 (±26) Gt yr^{-1} into the abyssal ocean. This freshening rate is on the same order of magnitude as the recent increase in mass loss of the west Antarctic Ice Shelf (Shepherd et al., 2012). Outside of these two regions, however, AABW changes were primarily driven by heave, with the largest isotherm heave seen in the Weddell Sea. This heave causes AABW in the South Atlantic to become more saline. The net effect of AABW salinity changes on sea level rise were negligible, with the freshening having a slight positive effect in the South Indian and Pacific and the heave having a slight negative effect in the South Atlantic. The warming and freshening contributed an average of 0.52 (± 0.18) mm yr^{-1} to local sea level rise south of 30 °S, with almost all owing to the warming.

Finally, Chapter 5 broadens the scope of this thesis by using the full-depth steric changes examined in Chapters 2 and 4 to conduct a full water-column SLR budget from 1993–2013. Here, we calculate regional and global rates of SLR owing to mass addition using the residual between total sea level changes from satellite altimetry and the steric sea level contribution between repeated occupations of full-depth hydrographic sections. The regional trends found agree well with mass addition estimates made directly from ocean bottom pressure calculated from the Gravity Recovery and Climate Experiment (GRACE) from 2003–2013. The two methods both find a global mass gain of 1.5 (± 0.4) mm yr^{-1}, between 1996–2006 for the residual method and 2003–2013 using GRACE data. Furthermore, both methods show a non-uniform mass addition pattern, with higher mass addition rates in the North Pacific, South Atlantic and the Indo-Atlantic sector of the Southern Ocean. Finally, the residual method is used to examine the deep ocean's relative contribution to the SLR budget. We find almost 0.2 mm yr^{-1} of bias is introduced into the budget when the steric contribution below 2000 m is neglected.

This thesis has highlighted the importance of monitoring the deep ocean. Over the sampling period considered here, we have seen a global-scale warming of the abyssal ocean, possibly indicating a slow down of the bottom limb of the MOC, and strong water-mass freshening of AABW within the Pacific and Indian sectors of the Southern Ocean. Quantifying these changes is important to accurately evaluating past changes in the global heat and SLR budgets. Ignoring the contribution of these changes to the budgets underestimates past decadal trends by ~10%.

Furthermore, understanding these changes and what is driving them is important for improving our ability to project how climate will change under future CO_2 emission scenarios. Currently, global climate models (GCMs) do not accurately portray the changes revealed by the observations discussed here. However, in order to incorporate these changes into GCMs, a better understanding of the driving forces are needed. Future work using new data from observational programs such as Deep Argo, incorporation of tracer data in analyses, and advancements in modeling all offer promising avenues for improvement in our understanding of the abyssal ocean.

References:

Masuda, S., Awaji, T., Sugiura, N., Matthews, J. P., Toyoda, T., Kawai, Y., et al. (2010). Simulated Rapid Warming of Abyssal North Pacific Waters. *Science*, *329*(5989), 319–322. doi:10.1126/science.1188703.

Rhein, M., S.R. Rintoul, S. Aoki, E. Campos, D. Chambers, R.A. Feely, S. Gulev, G.C. Johnson, S.A. Josey, A. Kostianoy, C. Mauritzen, D. Roemmich, L.D. Talley and F. Wang, (2013). Observations: Ocean. In: *Climate Change 2013: The Physical Science Basis. Contribution of Working Group I to the Fifth Assessment Report of the Intergovernmental Panel on Climate Change* [Stocker, T.F., D. Qin, G.-K. Plattner, M. Tignor, S.K. Allen, J. Boschung, A. Nauels, Y. Xia, V. Bex and P.M. Midgley (eds.)]. Cambridge University Press, Cambridge, United Kingdom and New York, NY, USA.

Shepherd, A., Ivins, E. R., A, G., Barletta, V. R., Bentley, M. J., Bettadpur, S., et al. (2012). A Reconciled Estimate of Ice-Sheet Mass Balance. *Science*, *338*(6111), 1183–1189. doi:10.1126/science.1228102.